Alma Mater Studiorum · Università di Bologna

Scuola di Scienze
Corso di Laurea Magistrale in Fisica del Sistema Terra

Observations and modeling of the Marginal Ice Zone

Supervisor:

Prof. Nadia Pinardi

Advisors:

Dott. Timothy Williams
Dott. Laurent Bertino

Presented by:

Giacomo Di Noto

Sessione III
Anno Accademico 2014/2015

The significance of our lives and our fragile planet is determined only by our own wisdom and courage.

We are the custodians of life's meaning.

Carl Sagan

Contents

Abstract

Global climate change in recent decades has strongly influenced the Arctic generating pronounced warming accompanied by significant reduction of sea ice in seasonally ice-covered seas and a dramatic increase of open water regions exposed to wind [Stephenson et al., 2011]. By strongly scattering the wave energy, thick multiyear ice prevents swell from penetrating deeply into the Arctic pack ice. However, with the recent changes affecting Arctic sea ice, waves gain more energy from the extended fetch and can therefore penetrate further into the pack ice. Arctic sea ice also appears weaker during melt season, extending the transition zone between thick multi-year ice and the open ocean. This region is called the Marginal Ice Zone (MIZ).

In the Arctic, the MIZ is mainly encountered in the marginal seas, such as the Nordic Seas, the Barents Sea, the Beaufort Sea and the Labrador Sea. Formed by numerous blocks of sea ice of various diameters (*floes*) the MIZ, under certain conditions, allows maritime transportation stimulating dreams of industrial and touristic exploitation of these regions and possibly allowing, in the next future, a maritime connection between the Atlantic and the Pacific. With the increasing human presence in the Arctic, waves pose security and safety issues. As marginal seas are targeted for oil and gas exploitation, understanding and predicting ocean waves and their effects on sea ice become crucial for structure design and for real-time safety of operations. The juxtaposition of waves and sea ice represents a risk for personnel and equipment deployed on ice, and may complicate critical operations such as platform evacuations. The risk is difficult to evaluate because there are no long-term observations of waves in ice, swell events are difficult to predict from local conditions, ice breakup can occur on very short time-scales and wave-ice interactions are beyond the scope of current forecasting models [Liu and Mollo-Christensen, 1988, Marko, 2003].

In this thesis, a newly developed **Waves in Ice Model** (**WIM**) [Williams et al., 2013a, Williams et al., 2013b] and its related **Ocean and Sea Ice model** (**OSIM**) will be used to study the MIZ and the improvements of wave modeling in ice infested waters. The following work has been conducted in collaboration with the *Nansen Environmental and Remote Sensing Center* and within the *SWARP* project which aims to extend operational services supporting human activity in the Arctic by including forecast of waves in ice-covered seas, forecast of sea-ice in the presence of waves and remote sensing of both waves and sea ice conditions. The WIM will be included in the downstream forecasting services provided by Copernicus marine environment monitoring service (fig. 1.3).

Chapter 1

Introduction

In the following chapter it will be briefly described how sea ice forms and how it is classified. Relevant parameters for sea ice study are introduced together with the observations used and the models related to the Waves in Ice Model.

1.1 Origin and study of Sea Ice

Sea ice is defined as any form of ice originated in the surface of the sea from the freezing of sea water. Much of it is located within the Earth's polar regions: the Arctic sea ice of the Arctic ocean and the Antarctic sea ice of the Southern Ocean. Sea ice undergoes a significant yearly cycling in surface extent. The Arctic sea ice extent generally reaches maximums in March and minimums in September. During its life it is subject to the action of winds, currents, waves, swell and temperature fluctuations, making it very dynamic and leading to a wide variety of types and features.

1.1.1 Formation

Ice first freezes in fine crystals, mainly in the form of small discs with the size of $2 - 3mm$, in suspension in a turbulent layer at the top of the water column. These crystals (*frazil*) further aggregate to minimize their thermodynamic energy evolving into more and more compact ice that imprison small quantities of very salty sea water (*brine*). These brine pockets weaken the sea ice (more or less like a porous material) making it more fragile and brittle compared to its freshwater analogy. When freezing continues, the *frazil* ice concentration increases until it finally reaches a transition point where ice crystals start to form small blocks known

as *pancakes*.

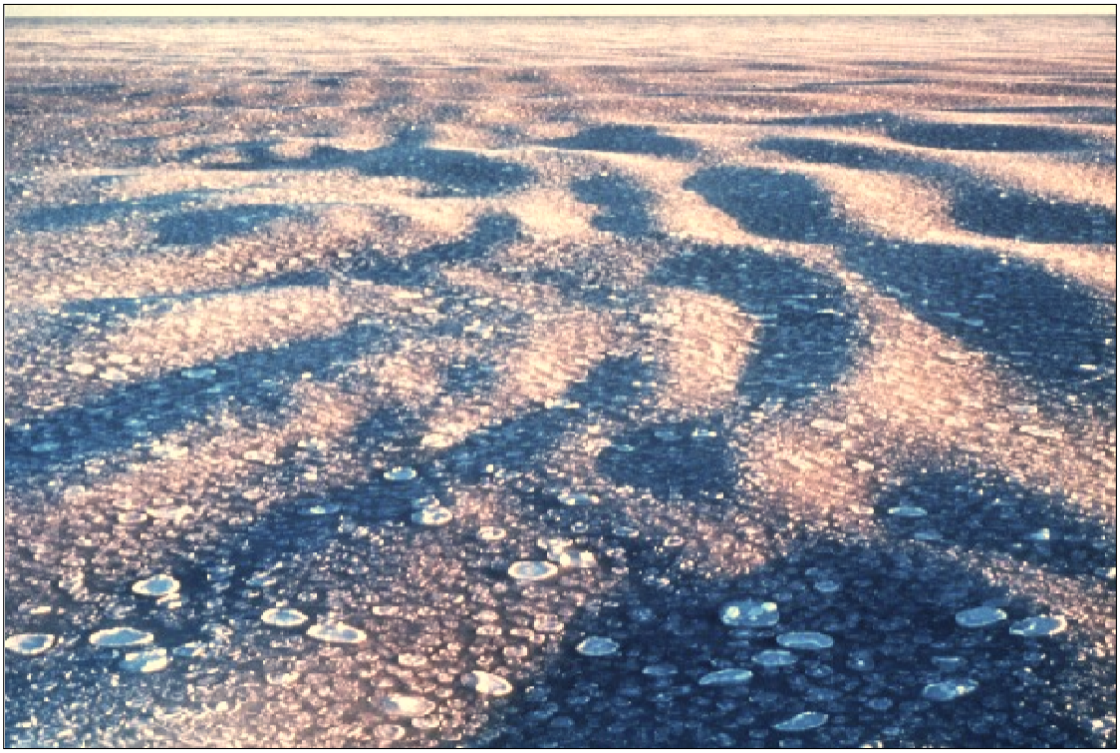

Figure 1.1: Waves into *pancake* ice infested waters.

The size of these newborn pancakes depends on the turbulent, wave-induced motion taking place in the surface but with proper conditions will grow with bottom and lateral freezing or by addition and compaction of snow on its top [Squire et al., 1995]. Wind and wave induced motion force the cakes to crash into each other breaking them into a more round shape while stronger wave action force them to group and meld on top of each other creating a thicker layer of ice. If freezing continues these pancakes will eventually reach diameters of $3-5m$ with $50-70cm$ thickness. Depending on ocean and meteorological conditions they may either break up and disperse or grow and meld with their neighbours. As growth continues, these blocks of sea ice now ranging from few meters to kilometres are referred to as *floes*.

1.1.2 Classification

Sea ice can be classified according to its age. *First-year* sea ice is young ice that has no more than one year's growth. In other words, it is ice that grows in fall

and winter (*freezing season*) reaching the maximum extent in late February, but does not survive the spring and summer months (*melting season*). During these months, sea ice retreats diminishing its extent till a minimum is reached (usually around September). Old sea ice is sea ice that has survived at least one melting season. It is generally thicker than first-year sea ice and is commonly divided into two types: *Second-year* ice, which has survived one melting season, and *multi-year* ice, which has survived more than one.

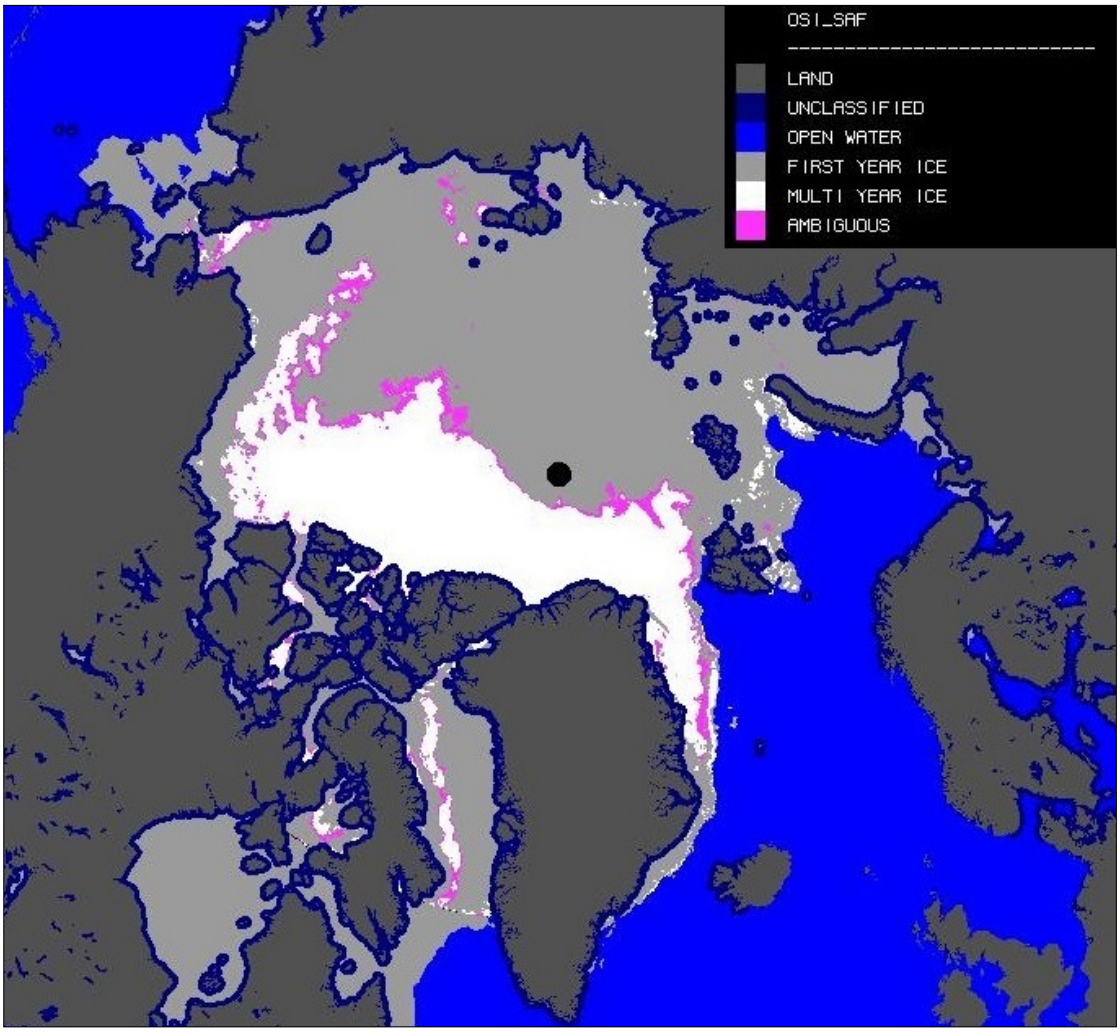

Figure 1.2: End of 2014/2015 freezing season, sea ice classified according to its age (**note:** second-year ice is classified as multi-year ice). Maximum sea ice extent was of 14.54×10^6 km^2 on 25-02-2015 [Fig. from OSI-SAF (1.2)].

Another classification used is whether or not it is able to drift. If sea ice is attached to the shoreline (or between shoals or to grounded icebergs) is called *landfast ice* or *fast ice*. Alternatively *drift ice* occurs offshore in wide areas, en-

compassing ice that is free to move with currents, winds and waves. The drift ice zone may be further divided into a *shear zone* (or *sparse ice area*), a *marginal ice zone* and a central *pack ice area*. Drift ice consists of floes of different diameters and, depending on the region, they can be few meters to several kilometres wide.

1.1.3 Definition of Marginal Ice Zone

The following work takes into great consideration the intermediate region between sparse and compact sea ice. This is the Marginal Ice Zone defined by the World Meteorological Organization as:

"The region of an ice cover which is affected by waves and swell penetrating into the ice from the open ocean"

This highly dynamic region is in fact, strongly influenced by the properties of sea ice, the state of the atmosphere and the ocean, including, specifically, short waves generated locally and ocean swell propagating from large ocean basins. As they encroach on the ice cover, waves are scattered causing it to bend and potentially break into smaller fragments causing fractures even in multi-year pack ice [Asplin et al., 2012, Prinsenberg and Peterson, 2011].

It has also been observed that floes damp waves so that, if the broken sea ice area is large enough, these will not penetrate, thus allowing the formation of thicker and wider ice. Sea ice damping effects on wave energy are strongly related to the the density and dimension of the ice floes. For this reason, model results for the MIZ will be classified in this work using *floe size distribution* (**FSD MIZ**). However, due to the scarcity of FSD observations, they will also be classified using *ice concentration* (**IC MIZ**) to enable comparison with passive microwave data.

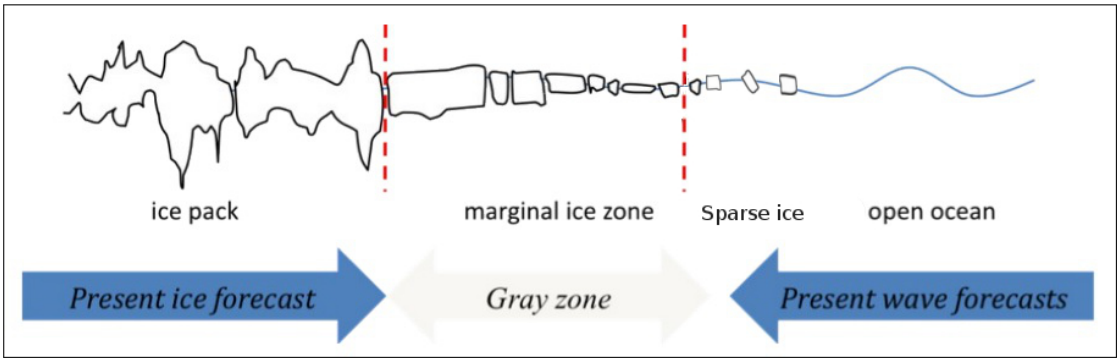

Figure 1.3: Transition from Open Ocean to the consolidated pack ice. The red lines, containing the *gray zone* represent the MIZ, a region still unmodeled by many of the present sea ice forecast models.

1.1.4 Floe Size Distribution

Commonly, present numerical models and observations focus on two variables to describe the state of sea ice: ice concentration and ice thickness. Several studies, however, showed that the response to wind and melting depends on ice floe size introducing, as a new important ice state variable, the **Floe Size Distribution** (**FSD**) [Steele et al., 1989].

This variable becomes extremely significant in the MIZ where relatively small ice floes are dominant, giving the FSD a key role for both dynamic and thermodynamic processes. To support this, it was discovered that ice velocity significantly decreases as floes become smaller than 100 m in diameter due to increased form drag. Moreover, the melting rate of ice floes increases for smaller floes (< 40 m) due to more prominent lateral melting. In addition, even size and shape distributions of floes can provide information about sea ice formation and break-up processes [Steele, 1992, Steele et al., 1989].

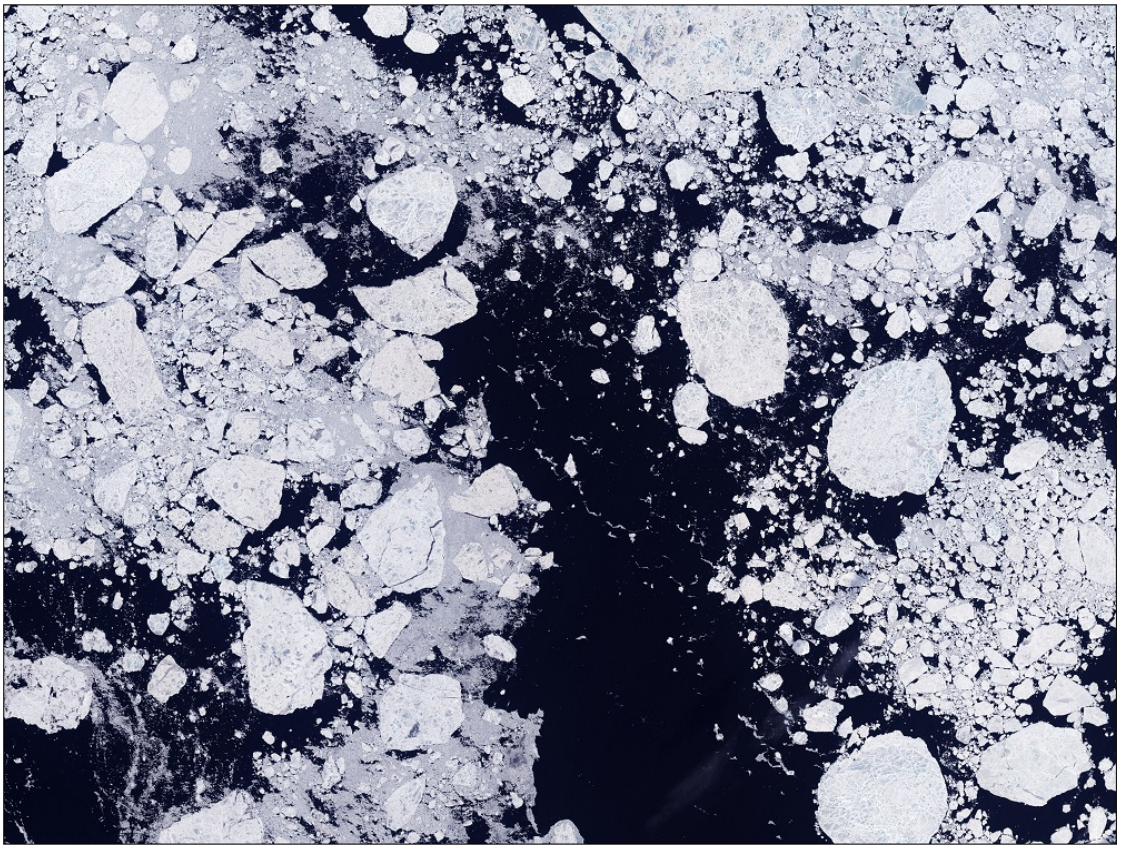

Figure 1.4: Arctic sea ice, captured on June 16, 2001, by NASA's Landsat-7 satellite.

Various observation methods were used to investigate floe size distribution both for Arctic and Antarctic sea ice showing similar results and common features. Several studies collected floe size distribution data at different scales using ship-borne, heli-borne and airborne radar and photographic mosaics as well as space-borne passive microwave and SAR observations. These showed that the FSD generally obeyed a power-law (Pareto) distribution and is commonly represented as a cumulative number distribution $N(d)$, where d is the diameter of the floe [Rothrock and Thorndike, 1984].

$$N(d) \propto d^{-\alpha} \tag{1.1}$$

Since sea ice floes have irregular shape, the diameter generally considered in literature is the average of the Feret diameters of the floe (also known as caliper diameters).

The exponent α is usually greater than 2 which implies that the expected

diameter and area are defined if the minimum floe size D_{min} is nonzero. However, in a fragmentation only process α should be less then 2 since the fractal dimension of the objects produced must not be greater than the Euclidean space dimension [Mandelbrot, 1983]. Investigating smaller floes (1 m to 1.5 km) showed that α was best fitted by a smaller value ($\simeq 1.15$) [Toyota et al., 2006]. This regime shift is consistent with:

$$D_c = \left(\frac{\pi^4 Y h^3}{48 \rho g (1 - \nu^2)} \right)^{1/4} \tag{1.2}$$

which corresponds to the diameter below which flexural failure cannot occur [Mellor, 1986].

An explanation to the exponent governing smaller floes was proposed by [Toyota et al., 2006] in terms of a breaking probability f, related to α by:

$$f = \xi^{\alpha - 2} \text{ or } \alpha = 2 + \log_{\xi}(f) \tag{1.3}$$

where f is the probability that a floe will break into ξ^2 pieces.

Such a distribution (power law with regime shift) has better behaviour as $D_{min} \to 0$. Other mechanisms are required to explain the exponent for the larger floes being greater than 2 thus several theories were developed. Among the most successful, one suggested to represent FSD with a truncated Pareto distribution, an emergent property of a certain group of multiplicative stochastic systems, described by the generalized Lotka-Volterra (GLV) equation [Herman, 2010]. Later though, a second theory was developed after it was observed that floes tend to herd at different scales growing into larger ones trough rafting and new ice formation. Herding and consolidation appears to work effectively (see the herds on the **right** of fig.1.4) and will therefore affect the distribution in this regime [Toyota et al., 2011].

This mechanism is not completely understood yet but it is often associated with the interaction between floes and ocean swell. The variable conditions of ocean swell, depending on region and time, would account for different values of α. Recent simulations lent credibility to this, as floes in such models tend to group in clusters with diameters obeying power-law distributions and exponents

often greater than 2 [Herman, 2011].

In this work the FSD is parameterised with the maximum floe diameter - D_{max} $[m]$ and so sea ice is classified using the criteria:

D_{max} $[m]$	**Classification - Description**
$D_{max} < 20\ m$	**Sparse Ice** (**SI**) - The floes are too little to significantly attenuate local wave motion and produce negligible scattering [Kohout and Meylan, 2008].
$20\ m < D_{max} < 300\ m$	**Marginal Ice Zone** (**FSD MIZ**) - The floes abruptly attenuate wave motion and are often broken by wave induced stress.
$D_{max} > 300\ m$	**Pack Ice** - The ice cover is treated no longer as a collection of floes, break-up is mainly caused by thermal imbalances and internal stresses. However, it has been recorded flexural failure induced by swell propagating within multiyear pack ice even at very large distances from the ice edge [Prinsenberg and Peterson, 2011].

1.1.5 Ice Concentration

Ice Concentration [**IC**] is a ratio describing the amount of the sea surface covered by ice as a fraction of the whole area being considered. Total concentration includes all stages of development that are present while partial concentration may refer to the amount of a particular stage or of a particular form of ice and represents only a part of the total. In this work ice concentration is considered only as a total concentration.

IC is reported as a percentage $[0 - 100\%]$ (or fraction from 0 to 1) where 0 is open water and 100% full ice cover. **Sea ice Extent** is the area above the 15% IC threshold a limit commonly referred to as **Ice Edge**. Given the percentage of ice concentration, sea ice can be further classified as follows:

Percentage	Classification - Description
$IC < 15\%$	**Sparse Ice** (**SI**) - frazil ice, small pancackes, slush. Swell and waves have little to no effect on sea ice.
$15\% < IC < 80\%$	**Marginal Ice Zone** (**IC MIZ**)- collections of floes with maximum widths of hundreds of meters. Waves and swell are damped by the ice which breaks.
$IC > 80\%$	**Pack Ice** (**PI**) - solid compact ice, floes with several kilometres of diameters. Common swell and waves are completely absorbed before reaching this region.

Ice concentration has a key role in the navigability of ice infested water. Navigability is the characterization given to a waterway passable by ship, even with the presence of sea ice. Vessel capability determines navigability of sea ice, however, general navigability is linked with concentrations under the 30% threshold.

1.2 Sea ice Observations

Sea ice can be observed and measured using a wide variety of methods and at different spatial scales. The smallest, as well as more precise observations available, are *in-situ* measurements (point-to-point local data), followed by *ship-borne* imaging (metres to hundreds of meters), to *air-borne* and *heli-borne* mosaics (kilometres to hundreds of kilometres). The largest as well as most frequently available observations, however, come from *space-borne* satellite data (global coverage).

In this thesis only the latter will be used, specifically only ice concentration data elaborated by the OSI SAF consortium. Hosted by Météo-France, sea ice products are processed and distributed under the supervision of the *OSI SAF High Latitude Processing Facility* operated jointly by the Norwegian (MET-No) and Danish meteorological institutes (DMI). Resulting sea ice fields are available daily within 6 hours after the last satellite data acquisition. This means within 06 UTC each day.

1.2.1 Origin and processing of observations

IC measurements come from a reprocessing of passive microwave brightness temperature of the polar oceans from orbital swath data generated by the Special Sen-

sor Microwave/Imager (SSM/I) aboard the Defense Meteorological Satellite Program (DMSP) F8, F11, and F13 and the Special Sensor Microwave Imager/Sounder (SSMIS) aboard DMSP-F17. The SSM/I and SSMIS frequency channels used to calculate brightness temperatures include 19.3 GHz vertical and horizontal, 22.2 GHz vertical, 37.0 GHz vertical and horizontal, 85.5 GHz vertical and horizontal (on SSM/I), and 91.7 GHz vertical and horizontal (on SSMIS). Thus, a total of nine channels result from vertical and horizontal polarization for each of five frequencies, with the exception of 22.2 GHz, which is vertical only.

Raw data from satellite is transmitted and processed in real time to tactical terminals such as the Air Force Global Weather Central (AFGWC) at Offutt Air Force Base, Nebraska and the Fleet Numerical Meteorology and Oceanography Center (FNMOC) in Monterey, California. These convert output voltages into sensor counts (brightness temperatures) and send them to the National Snow & Ice Data Center (NSIDC). Orbital data for each 24-hour period are mapped to respective grid cells using a simple sum and average method (drop-in-the-bucket method). 85.5 GHz and 91.7 GHz data are gridded at a resolution of 12.5 km, with all other frequencies at a resolution of 25 km (Goddard Space Flight Center polar stereographic projection).

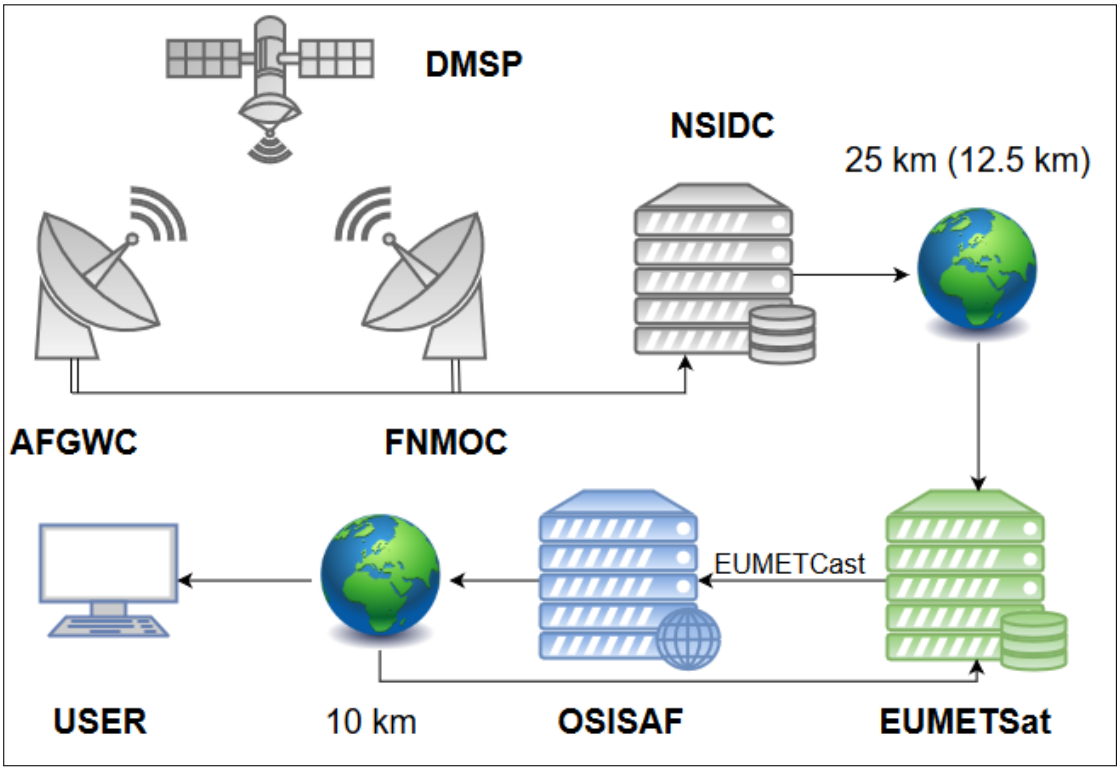

Figure 1.5: Data flow from satellite to the user. The earth thumbnail represents georeferencing of the data to a specific grid (25km grid from Goddard Space Flight Center grid; 10km OSISAF grid).

The data is collected by the (European Organisation for the Exploitation of Meteorological Satellites) EUMETSAT and sent through EUMETCast (a scheme for dissemination of various meteorological data) to the OSI SAF HL processing centre. Here, brightness temperature data is processed considering the atmospheric water vapour content as well as surface wind, which roughen the open water surface. These are common problems in the remote sensing of sea ice from passive microwave observations and are accounted using a radiative transfer model [Wentz, 1997] with inputs from European Centre for Medium range Weather Forecast (ECMWF) and High Resolution Limited Area Model (HIRLAM) NWP fields of surface wind, temperature and atmospheric water content.

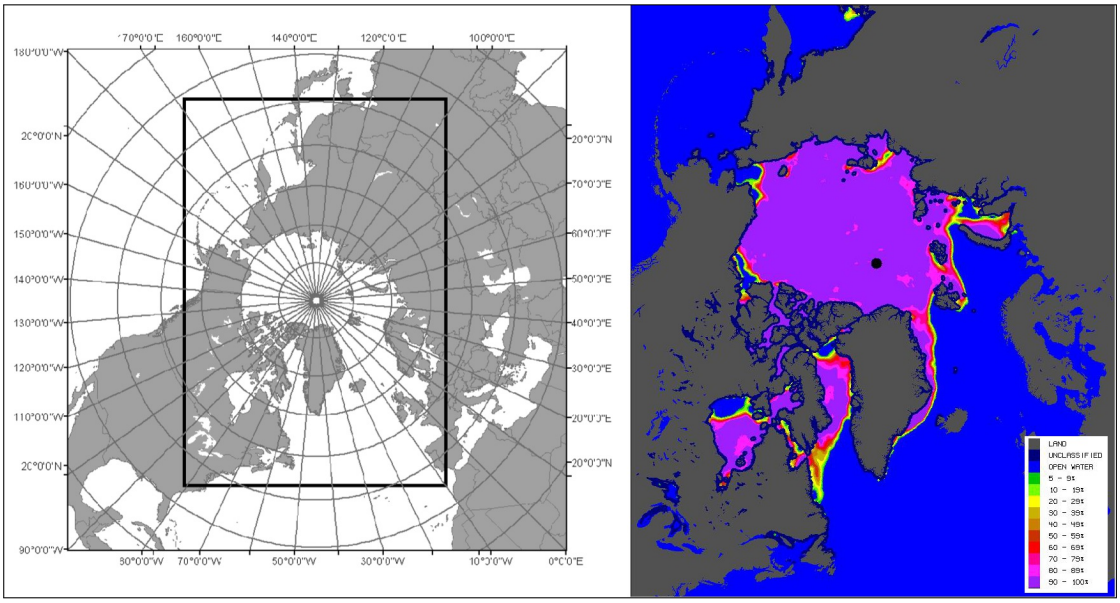

Figure 1.6: **left**, OSI SAF's Northern Hemisphere (NH) grid; **right** product for sea ice Concentration (NH grid) - 2015/06/01, the middle of the melting season.

The product grids are then adapted from the 25 km resolution Goddard Space Flight Center projections to the 10 km resolution grid used by OSISAF (fig.1.6). This result is achieved with a 2-step procedure. In the first step, ice concentration is calculated in the swath projection for each satellite passage. In the second step, (the multi pass analysis) these results are analysed on the 10 km OSI SAF grid. Several SSMIS observation nodes, with estimated concentrations, influence on each analysis grid point. The radius of influence for each SSMIS observation is 18 km. The weight assigned to each SSMIS observation in the analysis is dependent on:

σ_n^2 : square of the standard deviation of SSMIS concentration estimate

d : distance between the centre of the SSMIS node and the grid point

The variance of the concentration estimates were found using a large dataset of collocated SSMI concentration estimates for passages close in time and further assuming a Gaussian distribution around the concentration estimate (C_n), the most probable ice concentration (C_A) and its standard deviation (σ_A) in the SAF grid are:

$$C_A = \frac{\sum_{n=1}^{N} \sigma_n^{-2} C_n}{\sum_{n=1}^{N} \sigma_n^{-2}} \tag{1.4a}$$

$$\sigma_A = \frac{1}{\sum_{n=1}^{N} \sigma_n^{-2}} \tag{1.4b}$$

$$\text{with} \quad \sigma_n = 0.04 + 0.07(C_n(1 - C_n)/0.25) \tag{1.4c}$$

Validation and assessment of product performance is published on a monthly basis and is based on both objective and subjective comparison with high quality sea ice charts produced at the operational sea ice Services at DMI and MET-No. It is important to consider that ice charts are, to a large extent, based on subjective interpretation of high resolution SAR and AVHRR data. This is a well known issue given the uncertainty of human based analysis and lack of data in areas where SAR or AVHRR are of difficult interpretation or completely unavailable. (http://osisaf.met.no)

1.3 Sea Ice modeling

In an attempt to take into account the dynamical nature of sea ice, many theories have been developed. The most commonly used one deals with continuum ice sheets scattered with leads and ridges, where the deformation field follows a plastic constitutive rule and sea ice is considered as a uniform **Viscous-Plastic** (**VP**) material. From this theory has originated the so-called Viscous-Plastic class of numerical models [Hibler III, 1979, Hunke and Dukowicz, 1997]. However, alternatives such as the **Elasto-Brittle** (**EB**) rheology [Girard et al., 2010] have been proposed to account for the discrepancies in spatial and temporal scaling of ice deformations between VP model predictions and observations [Rampal et al., 2008, Girard et al., 2009]. These rheologies are also the dynamical core of the neXtSIM model [Rampal et al., 2015].

Figure 1.7: Aerial image of the pack ice in the Canada Basin. sea ice is compact with only few cracks wide enough to show the Arctic ocean underneath.

These models were designed to simulate pack ice, but it is unknown how well they handle the dynamics of MIZ-like situations, where the ice is broken up into smaller pieces by waves and may also be less compact, depending mainly on the wind. The ice floes are probably freer to move and thermodynamical processes such as melting or freezing may be enhanced compared to the central pack ice [Steele et al., 1989, Steele, 1992]. Direct numerical simulations (DNS) of the MIZ using granular models with either a single floe diameter [Shen et al., 2004,Herman, 2012], or with floe diameters sampled from a power-law type distribution [Herman, 2013] provide the most realistic physical models, but are usually applied in fairly idealised situations. However, they may help to parameterise large-scale models in the future, or perhaps they could be nested inside such models. In attempts to model the MIZ as a continuum, variations of the VP rheology have been proposed [Shen et al., 1987, Feltham, 2005] but these are not widely used.

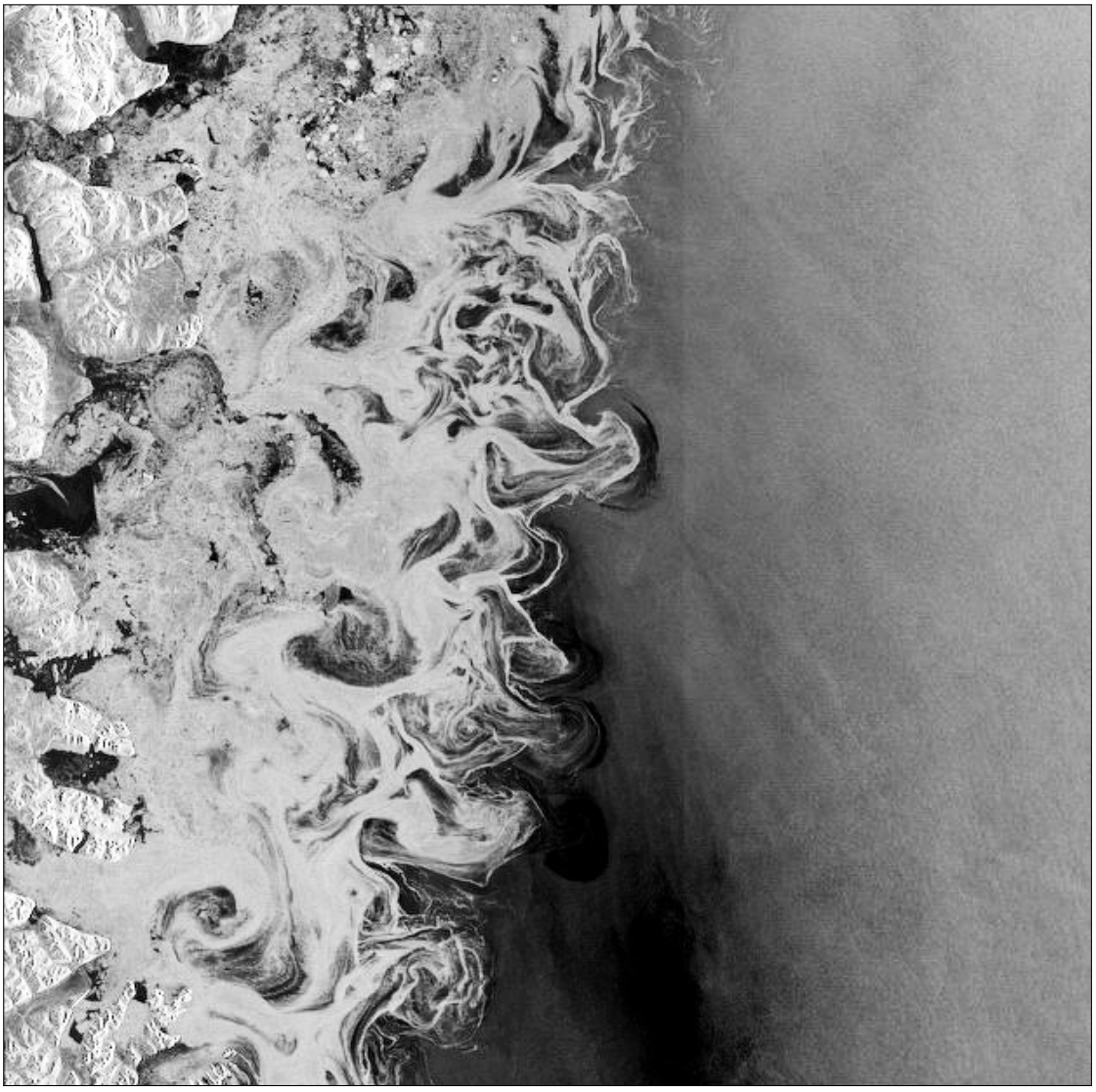

Figure 1.8: Synthetic Aperture Radar (SAR) image of the MIZ on the east coast of Greenland (Fram Strait). Reduced resistance to wind and currents make the MIZ mobile and fluid; thus, the presence of ice vortices at the ocean's surface as a clear indication of low cohesion.

The notion and importance of integrating waves into an ice/ocean model was first introduced more than 30 years ago [Squire and Moore, 1980]. Since then, several models for wave energy transport into ice-covered seas have been presented; evolution of the wave spectrum into ice was studied leading to a comparison of the attenuation occurring in ice fields with experimental data [Masson and Leblond, 1989,Perrie and Hu, 1996] . A similar transport equation focusing on the evolution of the directional spectrum followed [Meylan et al., 1997]. While they neglected non-linearity and the effects of wind and dissipation due to wave breaking, they improved the floe model by representing the ice as a thin elastic plate rather than

a rigid body.

Figure 1.9: A picture of the Marginal Ice Zone, characterized by floes of big size (hundreds of metres to few kilometres)

The above papers give the framework and demonstrate some implementations of wave energy transport into the sea ice, but all neglect ice breakage. In fact, it is only recently that this effect has been included in a wave transport problem [Dumont et al., 2011] . The method used involved modeling the attenuation of an incident wave spectrum and defining probabilistic breaking criteria so as to decide when the strains in the ice would exceed a breaking strain.

The WIM model provides a fuller description of the resulting ice cover: it evaluates the spatial variation of floe sizes throughout the entire region where breaking occurs and also allows the temporal evolution to be investigated. In addition, it considers the coupling between the breaking and the transport of wave energy [Williams et al., 2013a].

1.4 Ocean and sea ice Model

The Waves in Ice Model will be thoroughly discussed in chapter 2 while now its nesting and inputs are discussed. The WIM is implemented into an Ocean and Sea Ice Model (**OSIM**), their relation with inputs and sub-components are shown in fig. 1.10:

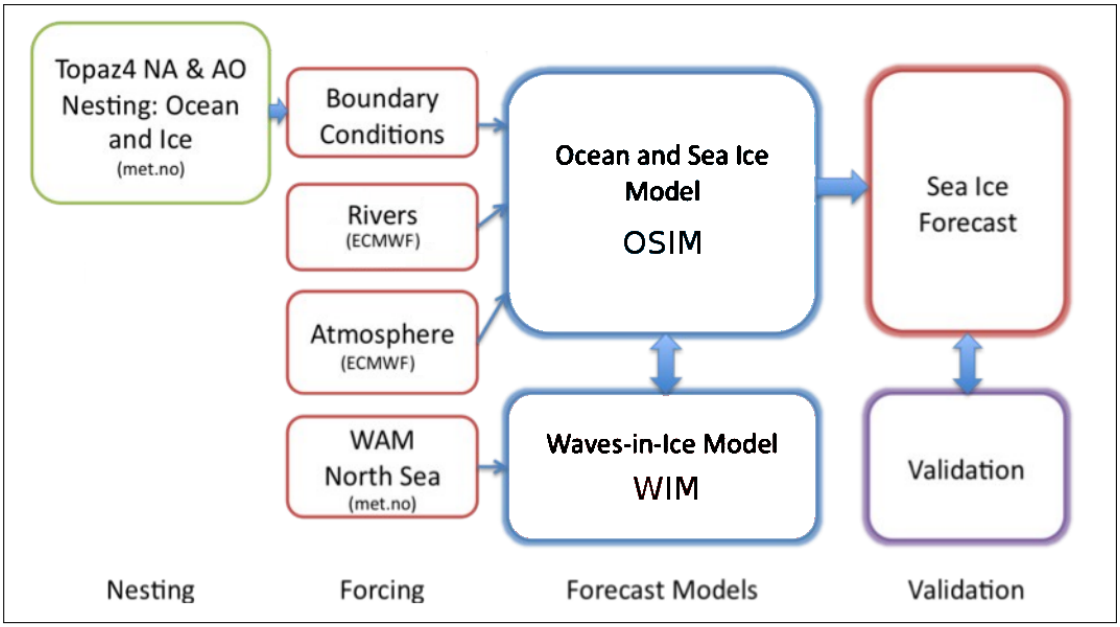

Figure 1.10: Schematics of forcing, models, the nested forecast system for the WIM

1.4.1 OSIM

The OSIM uses NERSC's version 2.2.12 of HYCOM (HYbrid Coordinate Ocean Model), coupled to a VP class sea ice model. In this implementation of HYCOM, the vertical coordinate is *isopycnal* in the stratified open ocean focusing on the conservation of traces and potential vorticity, and z-coordinates in the unstratified surface layer where mixing is important (minimum z-level thickness is $3m$, while the maximum is $450m$, to resolve the deep mixed layer in the Sub-Polar Gyre and Nordic Seas). Vertical mixing is solved using the GISS vertical turbulence closure scheme [Canuto et al., 2002]; this is a Reynold stress-based model which calculates vertical diffusivities for momentum, heat and salt in terms of the density ratio, the Brunt-Väisälä frequency, the Richardsson number and the dissipation rate of kinetic energy. This allows great accuracy given the presence of dense overflow and surface mixed layer that isolate sea ice from the warm Atlantic inflow [Sakov et al., 2012]. As for sea ice, the model is coupled to a one thickness category sea

ice model using the elastic-viscous-plastic (EVP) rheology [Hunke and Dukowicz, 1997]. Its thermodynamics, with a correction of heat fluxes for sub-grid scale ice thickness heterogeneities, are based on an old version of *CICE, The Los Alamos sea ice Model* [Drange and Simonsen, 1996]. Atmosphere and river flow data comes from the ECMWF in the form of Integrated Forecasting System (IFS) products for forecasts or ERA-Interim reanalysis for hindcasts.

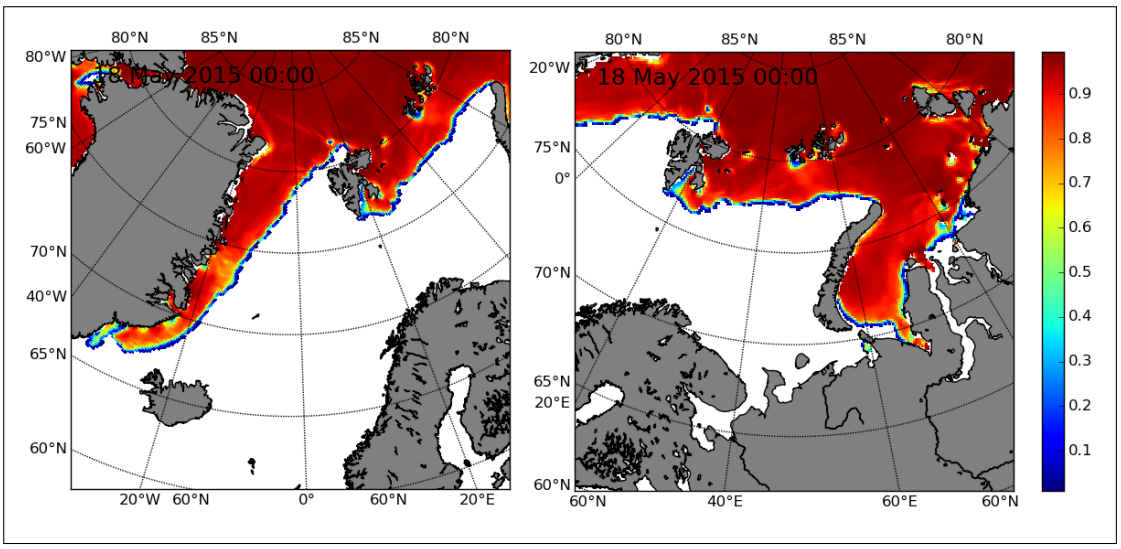

Figure 1.11: Ice concentration product for OSIM - 18-05-2015

Atmosphere and river flow data come from the ECMWF in the form of Integrated Forecasting System (IFS) products for forecast or ERA-Interim reanalysis for hindcast.

The geographical domain of OSIM is given by the boundary conditions of TOPAZ, a coupled Ocean-sea ice model and data assimilation system developed at NERSC (TP4) acting as the main monitoring forecast system for the North Atlantic Ocean and Arctic basin. The system is based on an ensemble Kalman filter (EnKF) [Evensen, 1994] with a 100-member ensemble. Compared to numerical weather prediction (NWP), the EnKF is prohibitively expensive for a large-scale, eddy-resolving ocean model but given TOPAZ's relatively small regional domain it was deemed affordable.

The model's horizontal grid spacing is approximately $12 - 16km$ in the whole domain. This is eddy-permitting resolution for low and middle latitudes, but it is too coarse to properly resolve all of the mesoscale variability in the Arctic, where the Rossby radius is as small as $1 - 2km$.

1.4.2 WAM - Waves

As for wave data, the operational wave prediction model WAM of the Norwegian Meteorological Institute (met.no) has been used. WAM is run four times a day at a $50km$ resolution (WAM50). Additionally a WAM with $10km$ and $4km$ resolution (WAM10 and WAM4) is run twice a day. WAM10 is nested into the $50km$ model while WAM4 is nested into WAM10. The higher resolution model primarily covers the Norwegian coastal waters as shown in Fig. 1.12.

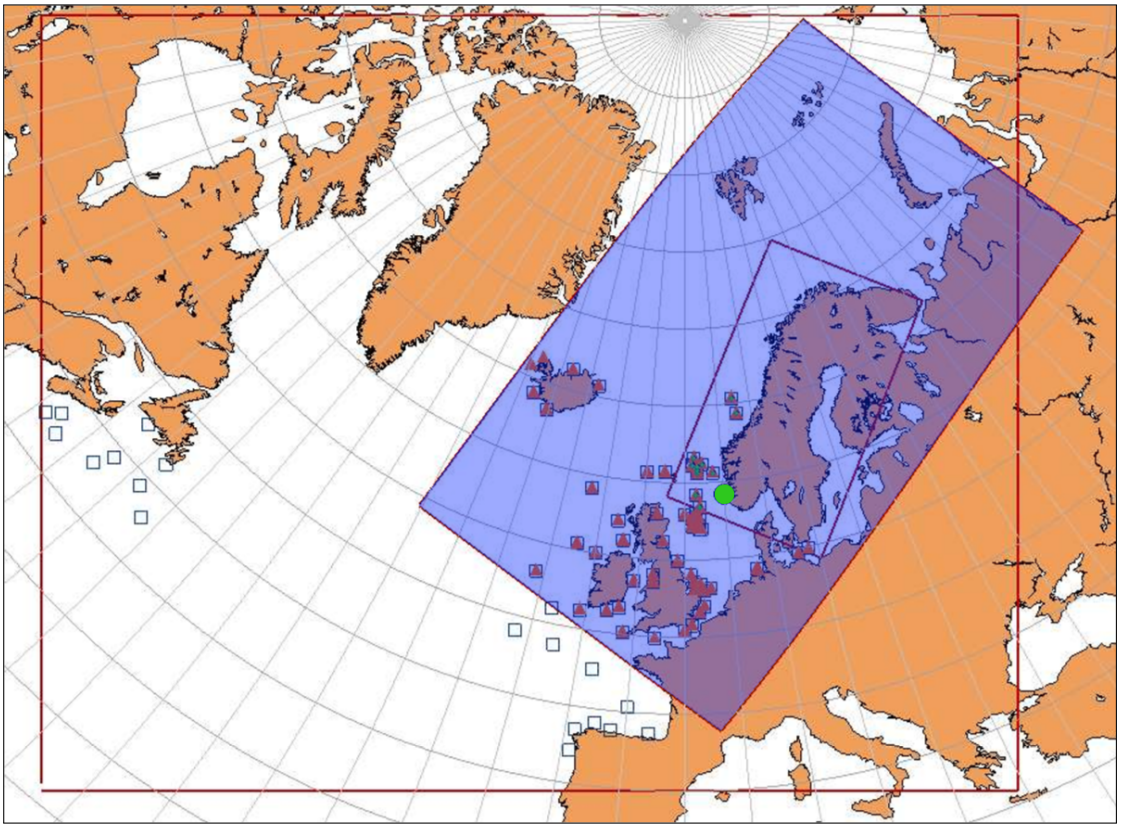

Figure 1.12: Buoys and domains of WAM50,WAM10 and WAM4. WAM10 domain is highlighted in **blue**. The **green** dot corresponds to the Hywind station where results of WAM4 and WAM10, are compared with observations.

The forecast period of each model is 66 hours. Wave measurements from ERS-24 and ENVISAT4 satellites are used to correct the initial state of the WAM. It computes two-dimensional wave spectra from which several parameters are computed: significant wave height, peak wave period, mean wave period, peak wave direction and mean wave direction. The wave parameters are computed for total sea, and for wind sea and swell.

The WIM currently uses WAM10 for wave data. This means that the only Arctic seas in its domain will be the northern Greenland sea, the Barents sea and the Kara sea. This is a great limitation of the model that is going to be fixed using a wider wave model possibly with grid resolution under 5 km. An example of such model is the newly developed global Wave Watch III which was not available for the results that will be shown thus confining the analysis of the Waves in Ice Model to the Barents-Kara seas and the Fram Strait (Appendix A).

1.5 Thesis Objectives

This thesis concentrates on the study of the MIZ through observational analysis and modeling experiments.

For what concerns modeling the Ocean and Sea Ice Model (OSIM) used in this thesis is presented in section 1.4.1 as well as the newly developed Waves in Ice Model (WIM) described in chapter 2. The main purpose of WIM is to extend the wave spectrum under the ice cover and consider the break-up of sea ice due to wave and wind induced stress. This will possibly lead to better forecasts given the high mobility of smaller ice floes in the presence of waves and their increased lateral melt [Steele et al., 1989, Toyota et al., 2011]. Model simulations have been carried out for the melting season period (April to September 2015) and are presented in section 2.3.

As for observational and model analysis, in chapter 3 a data analysis method based on the Principal Component Analysis (**PCA**) is presented and discussed together with some examples. This will allow objective and repetitive estimations of the MIZ's location and width. The PCA method is thus applied to WIM simulation results and to satellite observations (1.2). Only the *Barents-Kara* region and the *Fram Strait* region will be studied (see 1.4.2). Geographical characteristics as well as the importance of these regions for wave-sea ice interaction are explained in appendixes A.1 and A.2.

The above mentioned study will allow us to study the MIZ, specifically looking for errors in MIZ width estimations in model as compared to observations. It will then be used to partially assess the PCA analysis as an ice edge validation methodology.

Finally in appendix B are given two theoretical studies about possible diagnostics for wave induced effects on sea-ice. To study the potential improvements of the introduction of waves, two sections will be presented. The first one focuses on wave stress applied to the ice sheet and consequent energy transfer. The purpose is to assess if the wave stress has comparable effects to the wind stress and whether it may be important in MIZ modeling. The second one discusses modified ice growths derived from floe size distribution.

Chapter 2

WIM - Waves in Ice Model

The WIM is a wave-ice interaction model for the MIZ that calculates the attenuation of ocean surface waves by sea ice and potential breaking of it. The model is coupled with an ocean sea-ice model (OSIM, see 1.4.1) and includes two inter-related sub-components. First, a wave attenuation model that calculates the proportion of wave energy that is reflected by floe edges, and lost to dissipative processes, as a function of the number of ice floes encountered along the propagation path. And second, an ice breakage model that decides when the strain imposed by the passing waves on the ice cover is sufficient to cause fracture and how the resulting FSD evolves.

The wave spectrum is extended into ice-covered ocean according to the wave energy balance equation. Dissipation due to all conventional sources (i.e. winds,white-capping, non-linear interactions) are neglected; however, wave dissipation due to the presence of ice is parametrized. Furthermore, a viscous damping is included to simulate the unmodeled attenuation of large period waves. The attenuation rate considers a thin elastic plate scattering model and a probabilistic approach in order to derive a breaking criterion based on significant strain. This determines if the local wave field is sufficient to break the sea ice, thus connecting the FSD model and the local wave spectrum. This is done setting the maximum floe size to be half the dominant wavelength when the wave spectrum is sufficient to cause the ice to break. Such breakage will drastically alter the FSD, and consequently the attenuation coefficient of the WIM.

The criterion to determine the occurrence of ice breakage is based on the integrated strains imposed on the ice by passing waves. A critical strain, incorporating

a critical probability and a breaking strain is derived but in the absence of experimental or theoretical data, the value of the critical probability is set according to the limit for monochromatic waves.

Figure 2.1 shows the flow of information into and out of the WIM, whose three components, namely advection, attenuation and ice breakage will be described in relationship to the inputs and outputs. The inputs are the ice properties, the incident wave field and the initial FSD. Technically the FSD is also an ice property, but it will be treated separately due to the special role it plays in the WIM. The ice properties are all considered to vary only spatially, not with the time.

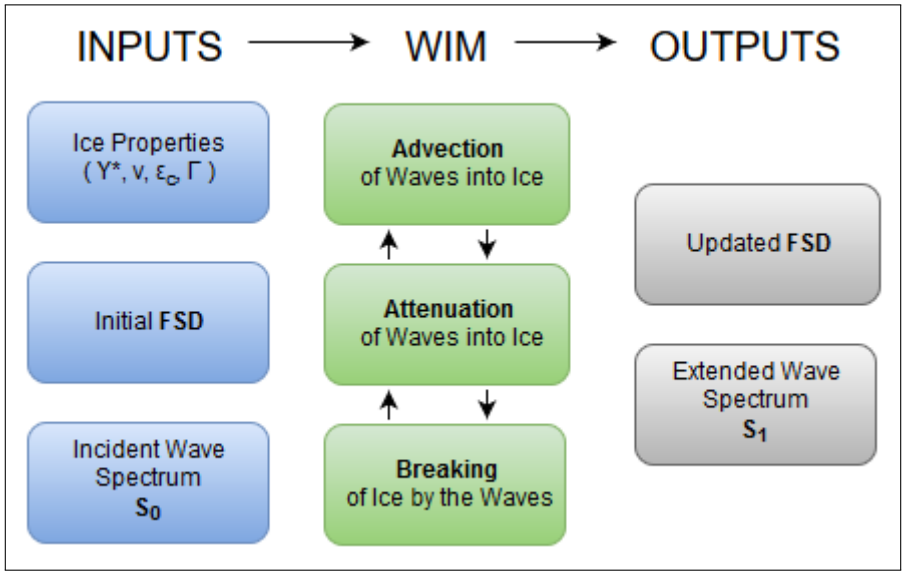

Figure 2.1: WIM's flow of information. Inputs, modeling and outputs.

The ice concentration (c) and thickness (h) are standard variables of ocean-sea ice models and their estimates can be easily obtained. However, the effective Young's modulus (Y^*), Poisson's ratio (ν) and breaking strain (ε_c) are non-standard and must be estimated (see 2.1.1). The breaking strain is formulated by means of a relationship for flexural strength using and Euler-Bernoulli beam model for sea ice [Timco and O.'Brien, 1994]. Further, an effective Young's modulus is proposed in this relationship, so that both instantaneous and delayed elasticity are incorporated. The damping coefficient Γ comes from experimental attenuation measurements and is included to increase the attenuation of long waves as this is excluded by the conservative scattering theory [Squire and Moore, 1980].

2.1 Inputs

Several studies and theories are now considered to satisfy the inputs needed by WIM. *Ice properties* (as well as FSD) come both from boundary conditions of the sea ice-Ocean model and theoretical estimations, *Waves* come from External Wave Models (see 1.4.2).

2.1.1 Sea ice properties

Investigators under a variety of conditions and test types showed that the flexural strength σ_c of sea ice has the following dependence on brine volume fraction (v_b):

$$\sigma_c = \sigma_0 \exp(-5.88\sqrt{v_b}) \;\; ; \;\; \sigma_0 = 1.76MPa \tag{2.1}$$

Equation 2.1 shows a monotonic decrease from σ_0 as v_b increases. Brine volume is calculated from ice temperature and salinity [Ulaby et al., 1981]:

$$v_b = 10^{-3} S \left(-\frac{49.185}{T} + 0.532 \right) \tag{2.2}$$

Flexural strength is analysed by means of Euler-Bernoulli beam theory in which the stress normal to the beam cross section is related to the analogous strain, therefore to convert flexural strength into a breaking strain all is required is the Young's modulus Y for sea ice. It is expected that during its lifespan in the MIZ, the sea ice will experience stress levels and rates such that the total recoverable strain $\varepsilon_t \approx \varepsilon_i + \varepsilon_d$, where ε_i is the instantaneous elastic strain and ε_d is the delayed elastic (anelastic) strain, known as primary, recoverable creep. The instantaneous Young's modulus will then vary allowing delayed elasticity to act. This is often called *effective modulus* or the *strain modulus* and is denoted by Y^*.

Recent studies report a linear relationship for $Y(v_b)$ of the form:

$$Y = Y_0(1 - 3.51v_b) \tag{2.3}$$

where $Y_0 \approx 10GPa$ is roughly the value for freshwater ice at high loading rates.

But, whilst increased brine volume leads to a reduction in the effective modulus Y^*, the data are too scattered for an empirical relationship for $Y^*(v_b)$ to be expressed. However, is reasonable to apply the same kind of reduction and since

brine volumes v_b range from 0.05 to 0.1, Y will reduce to between $6-8GPa$ [Timco and Weeks, 2010]. More challenging is determining the effect of anelasticity (delayed elasticity) on reducing Y to Y^*. The WIM applies a reduction of $1GPa$ based on the rate of the cyclical stress loading coming from surface gravity wave periods $(0.01 - 1Hz)$ [Williams et al., 2013a].

In summary the WIM uses:

$$Y^* = Y_0(1 - 3.51v_b) - 1[GPa] \tag{2.4a}$$

$$\varepsilon_c = \frac{\sigma_c}{Y^*} \tag{2.4b}$$

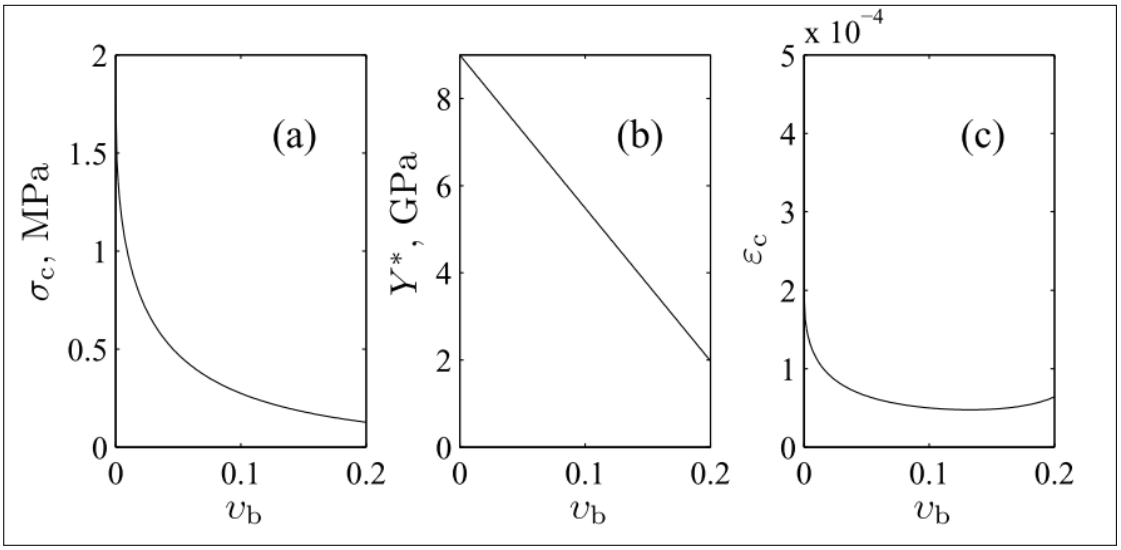

Figure 2.2: Behaviour of *flexural strength* (a), WIM's *effective Young modulus* (b) and the *breaking strain* (c) with the *brine volume* fraction v_b

An appropriate choice of the effective Young's modulus is very important from the wave modeling perspective, as the higher Y^* becomes the more energy is reflected at each floe present enhancing attenuation experienced by the wave train. However, since the same value of Y^* is used to convert flexural stress into failure strain, the analysis is self-consistent. The breaking strain has a minimum of 4.8×10^{-5} when $v_b = 0.15$ ($Y^* = 3.8GPa$). The value is approximately constant for $v_b \in [0.1, 0.2]$ and shows an increase for both higher and lower brine volumes. The

less porous ice is predictably stronger while the more porous is more compliant so it will be able to sustain more bending before breaking. The final property to consider is the Poisson's ratio. From seismic measurements $\nu = 0.295 \pm 0.009$, so as in most wave calculations involving ice it is simply taken to be 0.3 [Fox and Squire, 1991].

2.1.2 Floe Size Distribution

The model expresses the FSD in the form of maximum floe diameter D_{max}. In section 1.1.4 it has been showed that the floes obey a power-law (Pareto) distribution having two different regimes:

- *Large floes* with exponent $\alpha > 2$
- *Small floes* with exponent $\alpha < 2$.

The WIM's FSD is restricted to the *small floes* regime and is derived over a finite interval $[D_{min}, D_{max}]$. D_{max} is calculated from the break-up of the initial FSD while D_{min} is empirically set to 20 m as floes with less than this diameter produce negligible scattering [Kohout and Meylan, 2008]. The FSD is then calculated using a renormalization group (RG).

One attribute of power-laws is their scale invariance. Given equation 1.1, scaling the argument d by a constant factor c causes only a proportionate scaling of the function itself. That is:

$$N(c \cdot d) = (c \cdot d)^{-\alpha} = c^{-\alpha} \cdot N(d) \propto N(d) \tag{2.5}$$

This means that scaling by a constant c simply multiplies the original power-law relation by the constant $c^{-\alpha}$. Thus, it follows that all power-laws with a particular scaling exponent are equivalent up to constant factors, since each is simply a scaled version of the others. A similar self similarity is expected from the sea ice floes; in fact, scale invariance in fracture patterns of sea ice has been demonstrated over a wide range of sizes; fig. 2.3 shows a magnified image of part of an ice covered area that looks almost identical to the original confirming self-similar properties of the floes [Rothrock and Thorndike, 1984, Weiss, 2001].

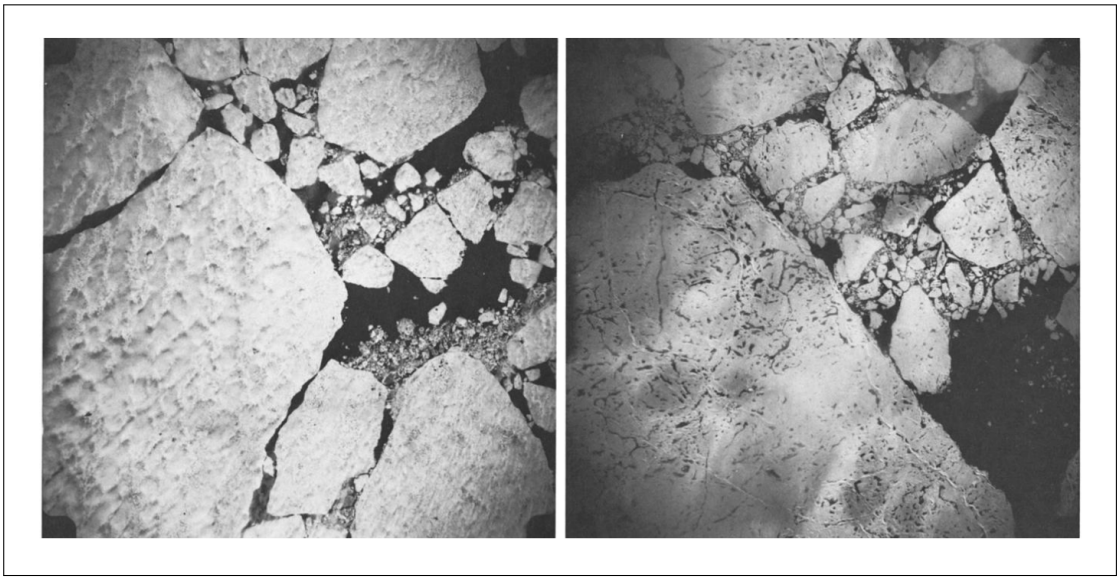

Figure 2.3: Views of sea ice on two different scales. Left frame is about 28 km wide, right one 2.4 km, from [Rothrock and Thorndike, 1984]

Therefore, in order to examine the formation process of size distribution in the WIM, a simple renormalization group (RG) is applied. This method has been successfully used to explain the scale invariance in various phenomena through a physical fracture/fragmentation process [Weiss, 2001]. One merit of the RG method is that it allows to treat the fragmentation process in a two-dimensional space. For this analysis it is introduced the concept of fragility, used as a physical parameter to explain the scale invariance in the mass distribution of rocks.

The fragility (f) represents the probability of fragmentation of floes and is considered to be a function of the strength of sea ice and the intensity of ocean waves [Turcotte, 1986]. Studies show that f takes nearly 0.6 at $80/100km$ from the ice edge, irrespective of the region, while it is reduced to 0.5 going into the inner region. These results indicates a close relation between f and wave activity [Squire and Moore, 1980] [Wadhams et al., 1988].

The possible scenario is as follows: first, ocean waves enter an ice covered region with full intensity and ice floes are fragmented into smaller floes. Then the ocean wave propagates further into the ice area with attenuated intensity. Thus in the inner region, ice floes are less fragmented with smaller f. It is then plausible that ice strength can be an important factor for f in the melting season when sea ice is significantly weakened due to melting. For this reason f is expected to increase significantly so $f = 0.9$ is chosen for sea ice in the melting season. Such a

high value indicates that sea ice is weak enough to be easily broken for any wave perturbations [Steer et al., 2008].

Knowing the extrema of the distribution (D_{max} and D_{min}) and given that sea ice floe size distribution in the MIZ generally follows a power law in the form 1.1, the floe size distributed between these limits can be calculated. Supposing N_0 rectangular ice floes with a length of d are initially present (0th order cell), these may fragment into smaller floes step by step. The basic hypothesis of this method is the assumption that, at each step, a cell fragments into four identical elements with the probability f $(0 < f < 1)$ (Fig. 2.4).

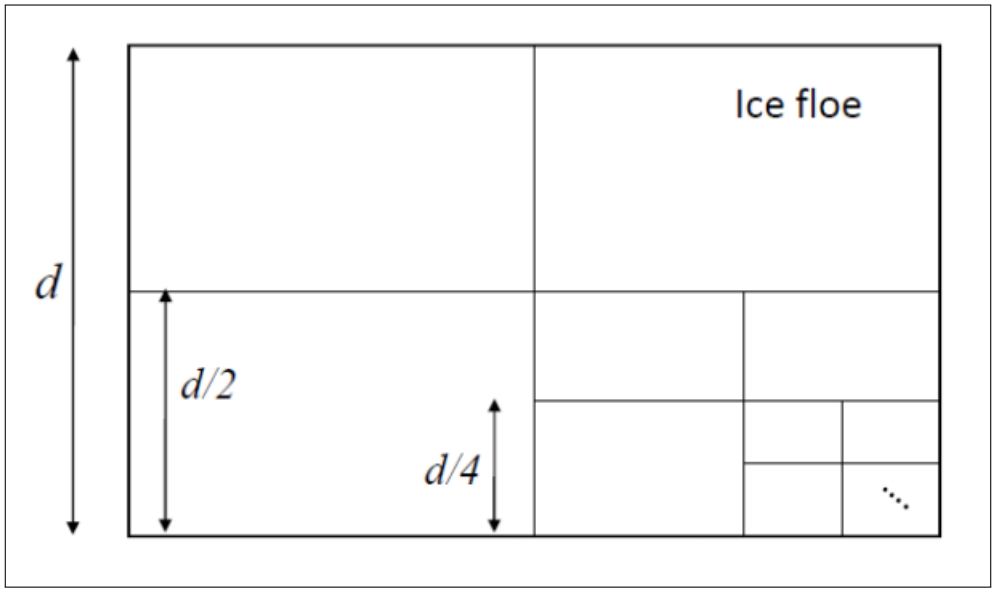

Figure 2.4: Schematic picture illustrating a simple renormalization method for ice floes. At each step, a cell is fragmented into four elements with the probability f.

Given ξ as an integer larger or equal to 2 (which determines the number of pieces each floe will fragment into) floes of size D_{max} are fragmented into ξ^2 floes of equal size D_{max}/ξ with a probability of $(0 < f < 1)$. After the first fragmentation step, the number of floes of size D_{max} is $\hat{N_0} = (1-f)N_0$ while the number of floes of size D_{max}/ξ is $N_1 = \xi^2 f N_0$. By repeating this step m time, the number of floes of size D_{max}/ξ^m is $\hat{N_m} = (1-f)(\xi^2 f)^m N_0$. Imposing the D_{min} sets the limit of number of fragmentation to:

$$M = [\log_\xi(D_{max}/D_{min})] \tag{2.6}$$

The minimum floe size does not mean that there are no smaller floes, but that floes smaller than D_{min} do not contribute significantly to scattering. Considering, as in WIM's case, $20 < D < 300$ and $\xi = 2$ the number of fragmentations per grid-cell are:

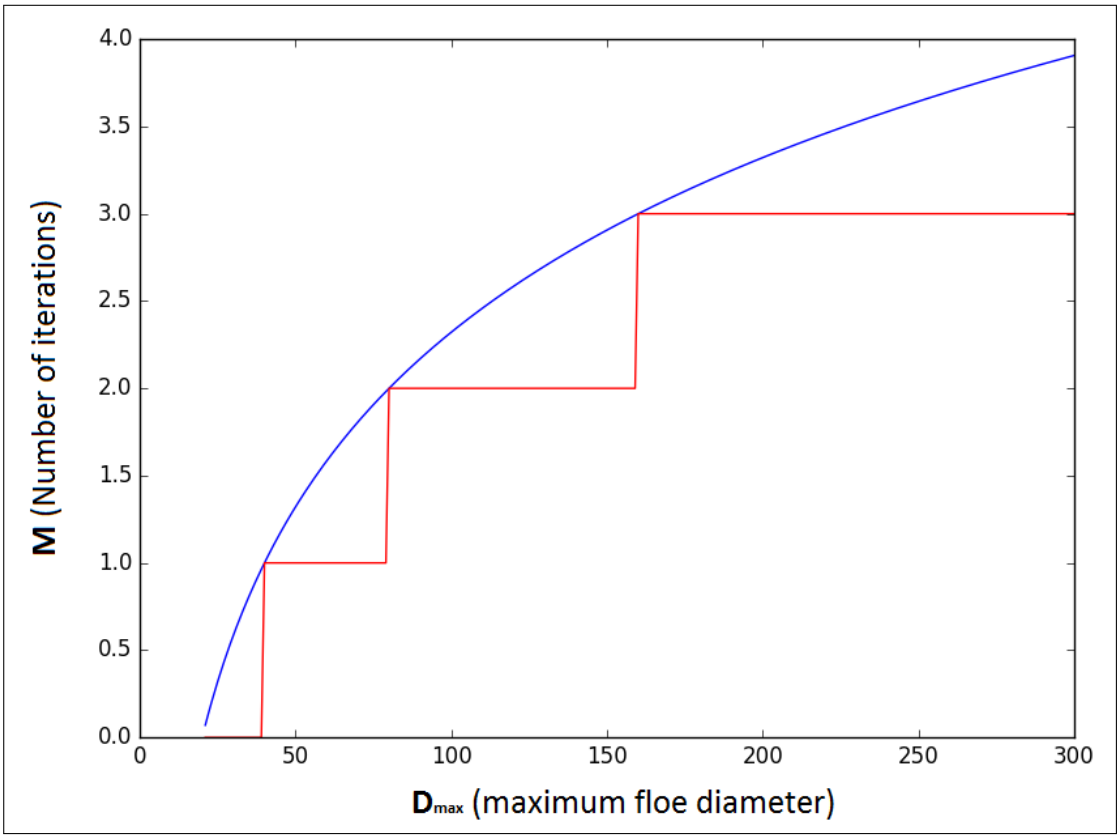

Figure 2.5: The **blue** line represents equation 2.6 while in **red** the results are rounded down to the nearest integer number. This is the actual number of fragmentation steps that will be used.

It is possible now to calculate the overall lateral and bottom surfaces of the ice floes composing the ice cover. A single floe ($N_0 = 1$) is considered and given its initial size, the number of possible fragmentations is derived using 2.6 (see fig. 2.5 as well). First of all a mean and a quadratic mean floe size are calculated from the distribution $\hat{N_m}(D_{max})$ as:

$$\overline{D} = \frac{\sum_{m=0}^{M}(\xi^2 f)^m (D_{max}\xi^{-m})}{\sum_{m=0}^{M}(\xi^2 f)^m} \tag{2.7a}$$

$$\overline{D^2} = \frac{\sum_{m=0}^{M}(\xi^2 f)^m (D_{max}\xi^{-m})^2}{\sum_{m=0}^{M}(\xi^2 f)^m} \tag{2.7b}$$

For simplicity, floes are considered as simple squares in this analysis hence the surfaces of a specific collection of floes will be:

$$S_{lat} = 4N_{tot}\overline{D} \tag{2.8a}$$

$$S_{bot} = N_{tot}\overline{D^2} = f_i A_{sq} \tag{2.8b}$$

where f_i is the ice concentration and A_{sq} the area of the grid cell, and N_{tot} is the total number of floes.

From a thermodynamic point of view, we are more interested in the ratios:

$$\beta_{lat} = \frac{S_{lat}}{S_{bot}} = \frac{4\overline{D}}{\overline{D^2}}, \tag{2.9a}$$

$$\alpha_{lat} = \frac{S_{lat}}{S_{lat} + S_{bot}} = \frac{\beta_{lat}}{1 + \beta_{lat}}. \tag{2.9b}$$

2.1.3 Wave energy

Wave energy is described by the spectral density function (SDF) $S(\omega, x, t)$, where $\omega = 2\pi/T$ is the angular frequency and T is the wave period. (SDF is sometimes written $S = S(\omega)$, taking the spatial (x) and temporal (t) dependencies to be implicit.) The wave spectrum may be defined either in the open ocean or within the sea ice, after having undergone attenuation. However, most External Wave Models (EWM) only predict S inside a region known as a *wave mask*, which currently stops at a conservative distance from the ice edge. While there has been some progress in the EWMs at addressing waves-in-ice (both in WAM and Wave Watch

3), there is still a problem of the ice mask of the WIM not matching the EWM's one. For this reason, the WIM applies a mask to the EWM waves that provides the initial boundary condition for the initial spectrum then advected across the gap between the wave mask and the ice mask, and then into the ice-covered ocean. For this work, the EWM used is described in section 1.4.2.

2.2 Advection, attenuation and break-up.

Ocean waves are the primary source of energy for ice breakup in the MIZ and are therefore the main driver determining its properties and extent. However, this interaction is particularly complex because ice suppresses waves by scattering and dissipating wave energy while simultaneously breaking up the ice shelves altering the local FSD. [Squire, 2007, Marko, 2003]. The outputs will alter ice properties which are then fed back into the ice-ocean model. An important follow-on is the momentum/energy exchange between the waves, the ocean and the atmosphere which is an unresolved issue even without the complicating presence of sea ice [Ardhuin et al., 2008].

2.2.1 Energy transport

Advection extends contemporary external wave models inside ice-covered oceans. The waves are transported according to the energy balance equation, namely:

$$\frac{1}{c_g} D_t S(\omega; x, t) = R_{in} - R_{ice} - R_{other} - R_{nl} \tag{2.10}$$

where $D_t \equiv (\partial t + \ \mathbf{c}_g \cdot \nabla)$ is the material derivative and $\mathbf{c}_g$ is the group velocity (having magnitude c_g) [Masson and Leblond, 1989, Meylan and Masson, 2006].

The source terms R_{in}, R_{ice} and R_{other} represent respectively the wind energy input, rates of energy loss to (or due to) the ice and the total of all other dissipation sources (i.e. friction at the bottom of the sea, losses from wave breaking or white-capping). These are all quasi-linear in S. The R_{nl} term incorporates fully non-linear energy exchanges between frequencies [Hasselmann and Hasselmann, 1985].

For the WIM, $R_{other} = R_{nl} = 0$ and $R_{ice} = \hat{\alpha}S$ changing 2.10 into:

$$\frac{1}{c_g} D_t S(\omega; x, t) = -\hat{\alpha}(\omega, c, h, \overline{D}\rangle) S(\omega; x, t) \tag{2.11}$$

The quantity $\hat{\alpha}$ is the dimensional attenuation coefficient, given by:

$$\hat{\alpha} = \frac{\alpha c}{\overline{D}} \tag{2.12}$$

where α is the non-dimensional attenuation coefficient, as the (average) amount of attenuation per individual floe, which is a function of ice thickness and wave period. The definition $R_{ice} = \hat{\alpha}S$ does not allow transfer of energy between directions (via diffraction by ice floes). R_{ice} is quasi-linear since an S that is sufficiently large to cause breaking lowers the average floe size $\langle D \rangle$ and subsequently increases $\hat{\alpha}$, according to equation 2.12.

The effects of neglecting R_{other} and R_{nl} are not clear. They may be important in moving the energy across the gap between the wave and ice masks, although as the resolution of the EWMs increases, this will become less of an issue. Several studies confirmed that some of the effects (like wind generation) are proportional to its open water analogy, and that R_{nl} was the same in the ice-covered ocean as in open water [Masson and Leblond, 1989, Doble and Bidlot, 2012, Polnikov and Lavrenov, 2007]. By including wind generation in the ice, models were able to reproduce (qualitatively at least) the observed *rollover* in the effective attenuation coefficient [Perrie and Hu, 1996]. That is, instead of attenuation increasing monotonically with frequency, reaching a maximum value before starting to drop again.

The operator D_t is the time derivative in a reference frame moving with the wave (the Lagrangian reference frame) at the group velocity $\mathbf{c}_g$. The above problem can be reconfigured, in between breaking events, in the Lagrangian frame, as:

$$\frac{d\mathbf{x}}{dt} = \mathbf{c}_g(\omega, \mathbf{x}, t), \tag{2.13a}$$

$$\frac{d}{dt} S(\omega; \mathbf{x}, t) = -c_g \hat{\alpha}(\omega; \mathbf{x}, t, S) S(\omega, \mathbf{x}, t). \tag{2.13b}$$

Thus the problem is divided into an advection problem and an attenuation

one which are solved by alternately consider the advection and attenuation processes [Williams et al., 2013b]. The advection is done using the WENO (Weighted Essentially Non-Oscillatory) method, while the attenuation is described below.

2.2.2 Attenuation

Attenuation of waves is included by considering two processes. The first one is the scattering of waves as they travel into an ice field, losing energy. This is modeled using multiple wave scattering theory or by models in which the ice cover is a viscous fluid or a visco-elastic material. The WIM considers a conservative scattering process hence the energy lost this way can be calculated and will be reflected back into open ocean. The rate of wave attenuation depends on the group velocity (c_g) and the attenuation coefficient $\hat{\alpha}$. These variables depend on wave period and the properties of the ice cover [Squire and Moore, 1980, Wadhams et al., 1988].

In scattering models, wave energy is reduced with distance travelled into the ice-covered ocean by an accumulation of the partial reflections that occur when a wave encounters a floe edge [Bennetts and Squire, 2012a]. Scattering models are hence strongly dependent on the FSD. In viscous models wave energy is lost to viscous dissipation, so these models are essentially independent of the FSD [Weber, 1987, Wang and Shen, 2011]. The WIM uses an attenuation model that includes both multiple wave scattering and viscous dissipation of wave energy. This means that there is a feedback between the FSD and wave attenuation, since the amount of breaking depends on how much incoming waves are attenuated, and the amount of scattering depends on how much breaking there is.

The remaining energy loss is parametrized by adding a damping pressure, which resists particle motion at the ice water interface. The phenomenological mechanism responsible for this energy loss is poorly understood and inadequately parametrized at present. Further investigations are required to balance momentum/energy in a fully coupled model. It is however necessary to include damping in the WIM to accurately predict the distance waves travel into the ice cover and hence the regions subjected to wave induced break-up (the width of the MIZ).

The implemented attenuation model has wave scattering as the dominant attenuation mechanism, but also include additional attenuation provided by a particular damping model [Robinson and Palmer, 1990]. Accordingly, the dimensional

and non-dimensional attenuation coefficients are, respectively:

$$\alpha = \alpha^{scat} + \alpha^{visc} \quad \text{and} \quad \hat{\alpha} = \hat{\alpha}^{scat} + \hat{\alpha}^{visc} \tag{2.14}$$

Multiple scattering model

The multiple scattering model is based on linear wave theory. The model predicts the spatial profile of time-harmonic waves in a fluid domain, which has a surface that is partially covered by a large number of floes. The floes are represented by thin-elastic plates and respond to fluid motion in flexure only. The wave number for the ice-covered ocean is k_{ice} and for the open ocean is k. In general $k_{ice} \neq k$, so scattering is produced by an impedance change when a wave moves from the open ocean into a patch of ice-covered ocean, or vice versa, at a floe edge. Attenuation due to multiple wave scattering by floe edges alone is sufficient for the present investigation, but extensions to scattering by other features in the ice cover, e.g. cracks and pressure ridges, are possible [Bennetts and Squire, 2012b].

The WIM is confined to two-dimensional transects, one horizontal dimension and one depth dimension. It cannot yet account for lateral energy leakage or directional evolution of the waves. Attenuation models capable of describing these features are being developed, but are not yet sufficiently robust to be integrated into the WIM [Bennetts et al., 2010]. Even with the restriction to only one horizontal dimension, computational expense can be large as there is an infinite sum of reflections and transmissions of the wave between each pair of adjacent floe edges. In the full multiple scattering problem exponential decay is a product of localization theory, which relies on positional disorder and requires proper consideration of wave phases.

Reliance on disorder implies the use of an averaging approach. The attenuation coefficient due to multiple wave scattering is hence calculated as an ensemble average of the attenuation rates produced in simulations that are randomly selected from prescribed distributions. It is natural to calculate a 3 non-dimensional attenuation coefficient, α^{scat} (per floe), for these types of problem, but this is easily mapped onto the dimensional attenuation coefficient $\hat{\alpha}^{scat}$ (per meter) for use in the WIM. The distribution of floes used in the model has a large impact on the predicted attenuation and hence the width of the MIZ.

Viscosity-based models

Recent model-data comparisons have shown that multiple wave scattering models give good agreement with data for mid-range periods ($6 - 15s$) [Perrie and Hu, 1996, Kohout and Meylan, 2008, Bennetts et al., 2010]. For large periods scattering is negligible and other unmodeled dissipative mechanisms are more important, although it is unclear which mechanism takes on in this regime. Plausible causes include secondary creep occurring when flexural strain rates are slower, and frictional dissipation at the ice-water interface. While this remains unresolved, the attenuation of large period waves is modeled in the WIM with the damped thin elastic plate model [Robinson and Palmer, 1990]. It contains a single damping coefficient Γ, which produces a drag force that damps particle oscillations at the ice-water interface. In practice, the dispersion relation is solved and the imaginary part of the damped-propagating wave number ($K(\omega, \Gamma) \approx k_{ice} + i\delta$) is used, and set the viscous attenuation coefficients to be:

$$\alpha^{visc} = 2\delta\langle D\rangle \quad \text{and} \quad \hat{\alpha}^{visc} = 2\delta c \tag{2.15}$$

The magnitude of the damping coefficient, Γ, is set using data from the most complete single experiment on wave attenuation available at present [Squire and Moore, 1980]. More experimental data, with detailed descriptions of prevailing ice properties and wave conditions, would help to tune Γ or to compare different models of wave dissipation.

2.2.3 Break-up of sea ice

The WIM derives the mean square value of the strain applied by the waves into a thin elastic plate representing the floes. Specifically:

$$\langle \varepsilon^2 \rangle = m_0[\varepsilon] \tag{2.16a}$$

$$m_n[\varepsilon] = \int_0^\infty \omega^n S(\omega) E^2(\omega) d\omega \tag{2.16b}$$

$$E(\omega) = \frac{h}{2} k_{ice}^2 W(\omega) \tag{2.16c}$$

In these, m_n is the n-th order spectral moment, k_{ice} is the positive root of the dispersion relation for a section of ice-covered ocean, $W(\omega) \approx \frac{k_{ice}}{k}|T|$ with T as the transmission coefficient for a wave travelling from water to ice.

$E(\omega)$ represents the approximate strain amplitude, per metre of water displacement amplitude of a monochromatic wave in the form of $\eta_{ice} = W cos(k_{ice}x - \omega t) = W \cdot n)$. It does not account for non-linear interactions between frequencies which could be very important for an ice breakage event. For now, brittle failure is assumed as a criterion for ice failure so that a linear stress-strain law applies right where the ice breaks. Let the significant strain amplitude be $E_s = 2\sqrt{m_0[\varepsilon]}$, which is two standard deviations in strain. Since wave heights generally follow a Rayleigh distribution and so will its applied strain therefore, we can define a probability of the maximum strain from a passing wave E_W as:

$$P_\varepsilon = P(E_W > \varepsilon_c) = \exp(-2\varepsilon_c^2/E_s^2) \tag{2.17}$$

Now a critical probability threshold (P_c), such that if $P_\varepsilon > P_c$ the ice will break, will be found. In such case that the maximum floe size is set to $D_{max} = max(\lambda_W/2, D_{min})$, where $D_{min} = 20\ m$ (see 2.1.2), given equation 2.17, said probability can be written as:

$$E_s > E_c = \varepsilon_c\sqrt{-2/\log(P_c)} \tag{2.18}$$

In the simulations run for this work it was chosen $P_c = e^{-1} \approx 0.37$. This value is derived from a monochromatic wave induced strain but is scheduled to be tuned once better observational information becomes available [Williams et al., 2013a].

2.3 WIM simulations

Two experiments were run with the OSIM+WIM configuration, a forecast (WIM-fc) and an hindcast (WIM-hc). As already introduced, WIM is coupled to an ocean and sea ice model (OSIM) which was run independently daily with a 7-day forecast. Every Monday, initial conditions for the ocean and sea ice fields are taken from the operational TOPAZ forecast model at Met Norway 1.4.1.

WIM-fc was first launched in the second week of May 2015 (07-05-2015) and has been operational using a different wave model (Wave Watch 3) since Decem-

ber 2015. Its initial conditions come from a daily forecast run of OSIM (7-day daily run) where waves are not considered. Its forecast time is 66 hours given the same limit of the wave model used 1.4.2, the model outputs ice concentration, extended wave spectrum and maximum floe size data every 6 hours. These products are then merged into a single netCDF file and uploaded to SWARP's website (https://swarp.nersc.no). WIM-hc was a 7-day free model hindcast from 2 March 2015 to 30 September. For this experiment ECMWF (ERA-interim) atmospheric forcing is applied with the WAM North Sea model (1.4.2) being used for wave forcing.

Data is missing the second week of March (6th to 12th) and the second week of June (8th to 14th) because of missing wave data, the first week of June (1st to 7th) because of corrupted restarts and the third week of August (17th to 23rd) because of missing and corrupted wind data.

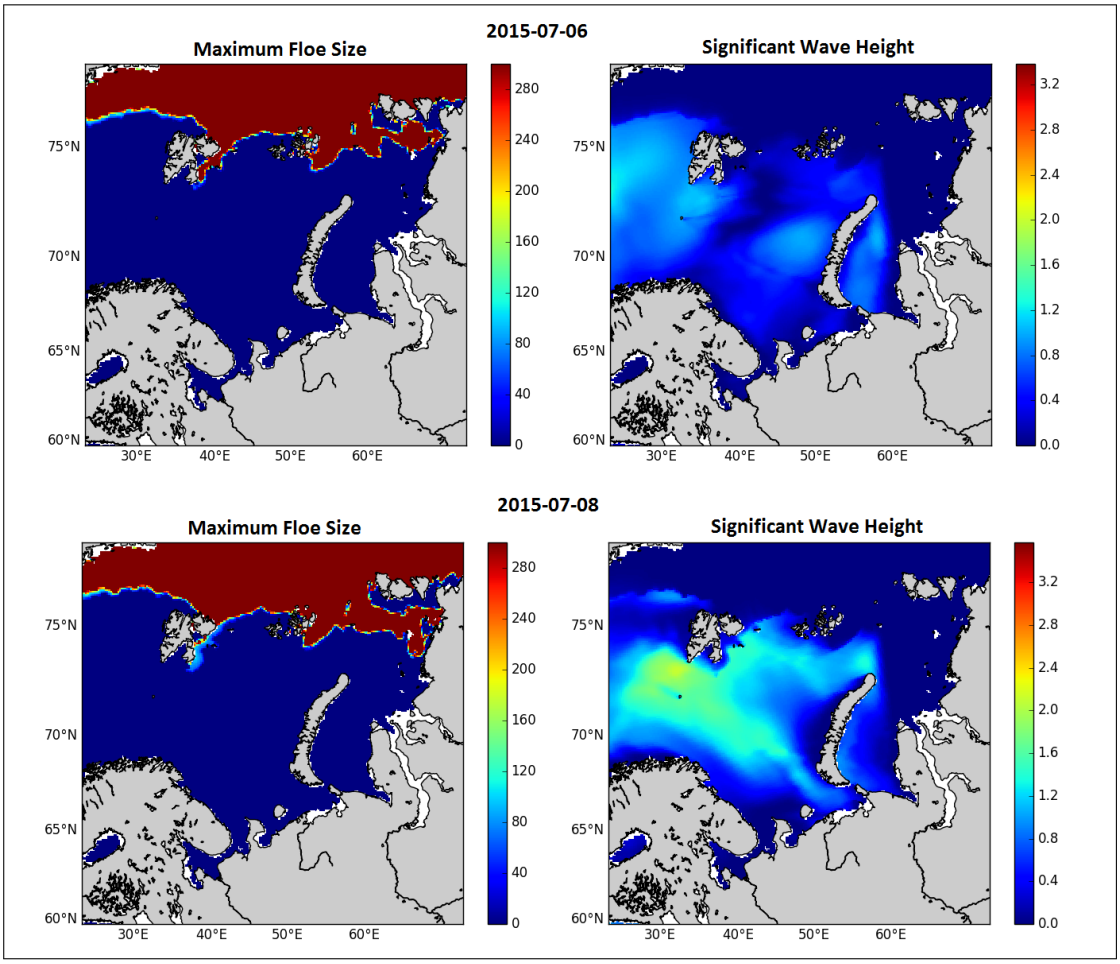

Figure 2.6: 6th July wave event for the Barents and Kara seas region.**Top** figures come from 2015-07-06 run, **bottom** show the 2 day forecast (2015-07-08). Maximum floe size as well as significant wave height are given in meters.

The 2015 melting season was not characterised by big wave events (most of the Arctic 2015 storms happened in late Autumn and Winter), however, the effect of wave-ice interaction can be seen even for relatively small swell coming in from the Atlantic basin. Such event was forecast by the WIM and is showed above (fig. 2.6) and below (fig. 2.7).

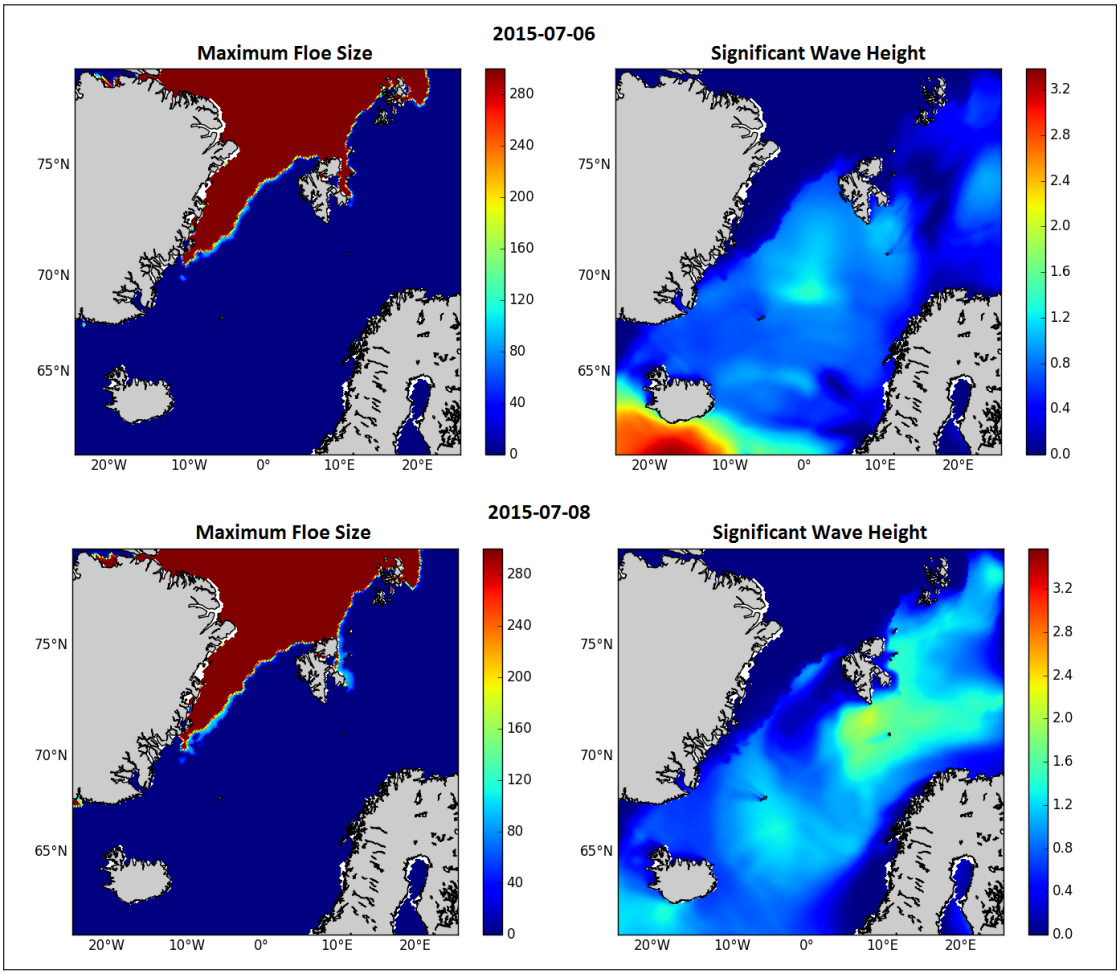

Figure 2.7: 6th July wave event for the Fram Strain (Greenland) region. **Top** figures from 2015-07-06, **bottom** from 2015-07-08. Maximum floe size and significant wave height expressed in meters

It is clear how most of the waves and swell do not reach the Kara basin leading to a relative growth west to Vilkitsky strait (collection of islands in the upper right corner of fig. 2.6). The Svalbard archipelago instead clearly lost most of its fast ice in just two days. As for the Fram Strait, the most exposed edge of the MIZ (southern tip) shows a smoother ice edge indicating wave induced break-up.

As for WIM-hc a detailed analysis of the MIZ for the melting season in given in chapter 3. Here it is presented a significant wave-in-ice break-up event happened on the 18th of December 2015, in this case Wave Watch 3 (WW3) wave model was used. During the period from 17 to 19 of December 2015 a low-pressure system producing significant wave heights of over 6 m reached the ice edge in the Fram Strait area. The main event in Fram Strait is happening over 24 hours, from 12:00

h at 17 December to 06:00 18 December, and model results for this date are presented in fig. 2.8. The significant wave height, Hs (m), from the WW3 Arctic wave model is presented in the right-hand panels of fig. 2.8. Areas where the maximum floe size is less than 250 m are here defined as MIZ areas (see the left-hand panels in fig. 2.8). The average widths of the MIZ is estimated, see Section 3.2, and the numbers are indicated in the figures.

The significant wave height increases from $H_s < 2\ m$ at the beginning of 17th December to a core in the wave field of $H_s > 6.5\ m$ in the beginning of 18 December. This has a major impact on the ice close to the open ocean. When the wave field moves north, these large waves propagate into and break up the ice, creating a much larger MIZ area. The estimated averaged MIZ width increases from below 60 km in early 17 December to above 97km during 19 December. A deeper study of this event and a comparison with high quality SAR images and hand-drawn ice charts was included into 2016 validation report of the SWARP project [NERSC, 2016].

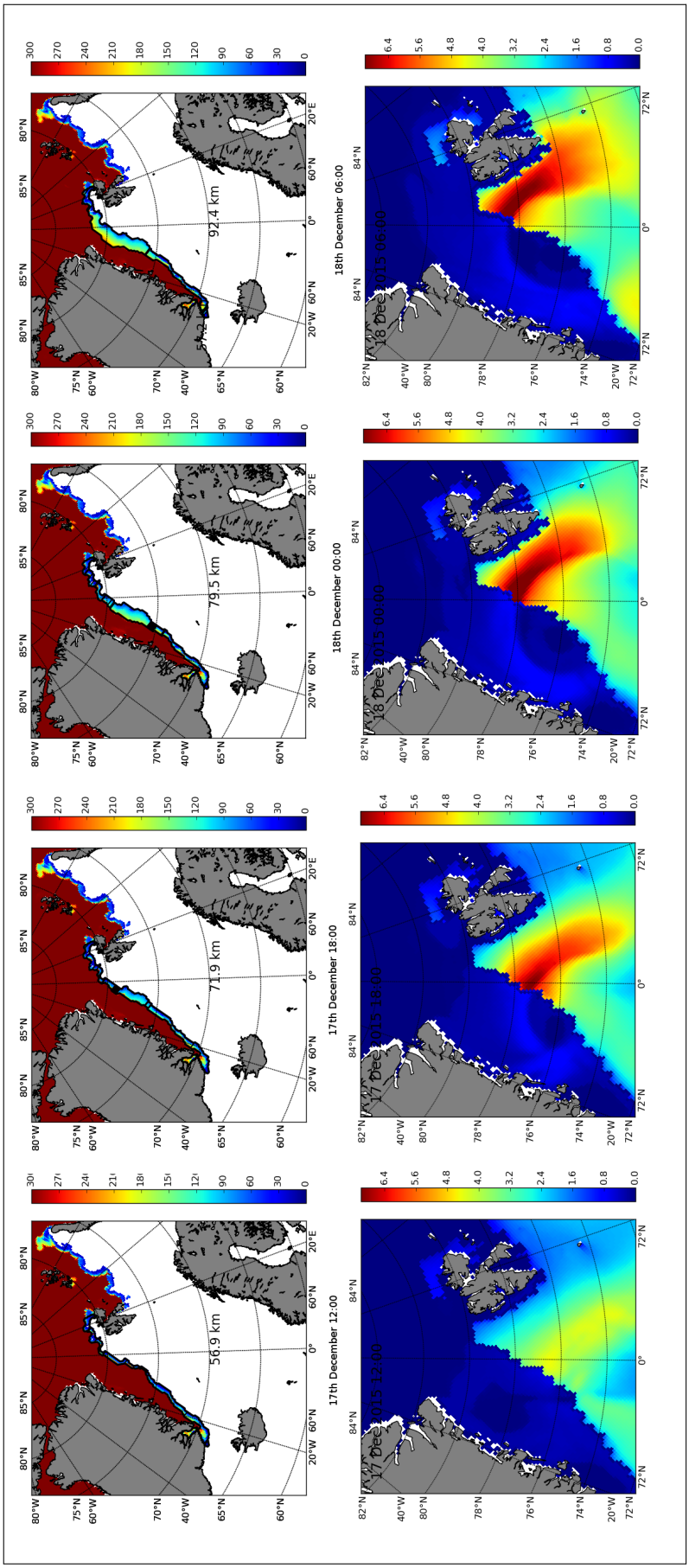

Figure 2.8: 18th December wave event for the Fram Strain (Greenland) region. **Top** images are maximum floe size data [m] with highlighted (in **black**) the MIZ boundaries (i.e. ice edge and pack ice). In the middle of each figure is given the average width of the MIZ. **Bottom** is the significant wave height from WIM [m].

High quality SAR images were also acquired for this event, in fig. 2.9 a Radarsat-2 image was taken at 6:51 UTC, 18 December 2015 while in fig. 2.10 a Sentinel-1 image from 16:34, 18 December 2015. Particularly interesting is the vastly increased wave penetration as seen in fig. 2.10 as well as the change in texture of the ice there.

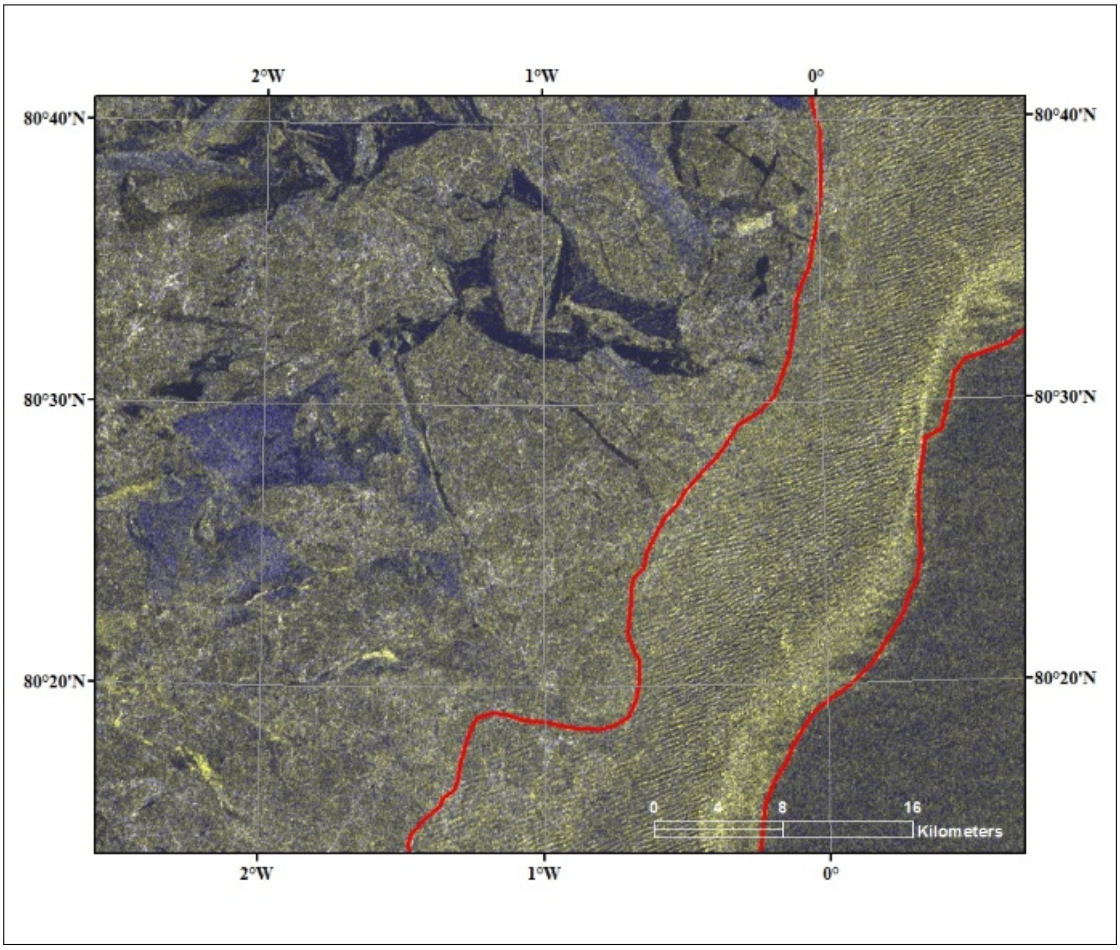

Figure 2.9: Radarsat 2 image from 06:51, 18 December 2015. The **red** lines denote the estimated boundary of the MIZ

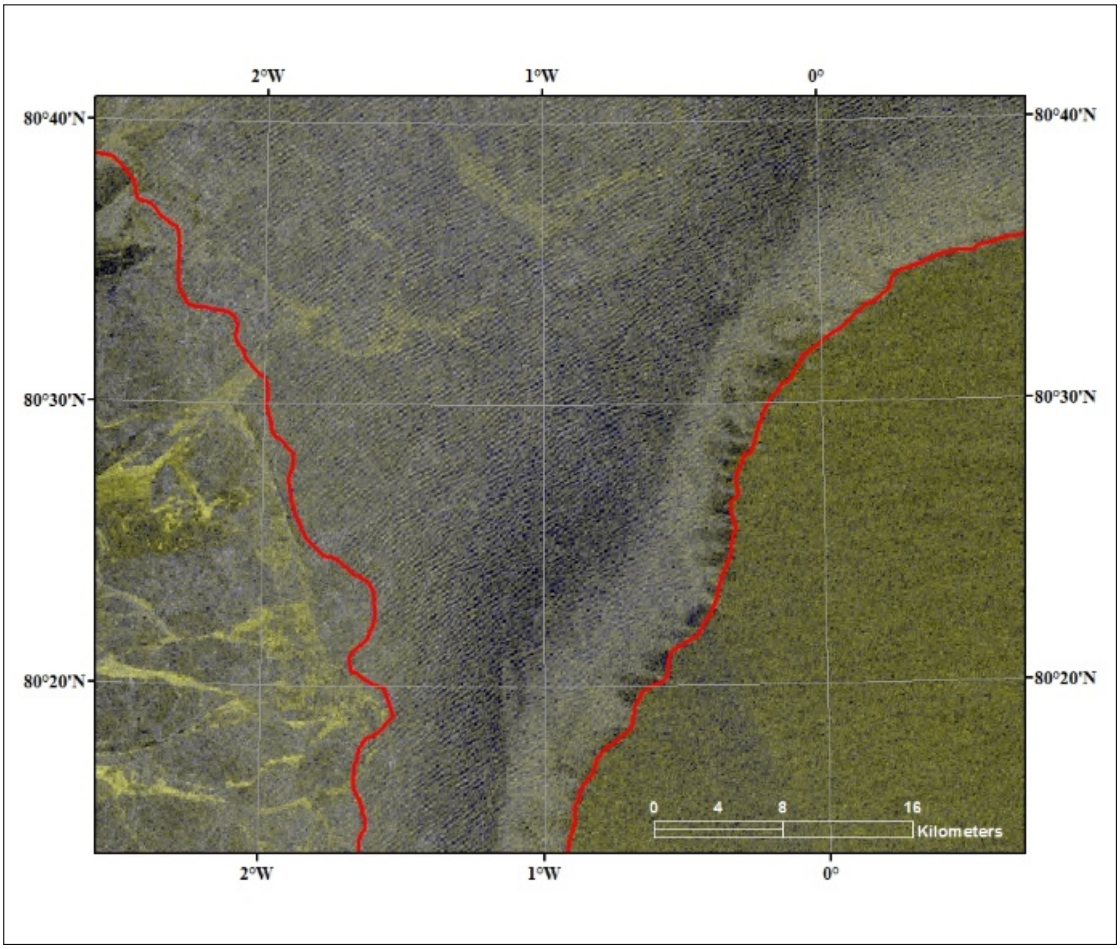

Figure 2.10: Radarsat 2 image from 06:51, 18 December 2015. **Red** lines as estimated boundary of the MIZ.

At NERSC, Natalia Zakhvatkina, Anna Vesman and Alexandra Mushta are developing a support vector machine (SVM) algorithm to automatically classify sea ice in high quality SAR images. This supervised learning model with associated learning algorithms analyse the accuracy of the ice-water separation by comparing training maps to the classification results. This reached reasonably good agreement, but needs some fine-tuning as improving the classification (assessed visually) led to an increase in the error. The algorithm is still being trained to distinguish between MIZ/pack ice and multi year ice (MYI)/first year ice (FYI). Fig. 2.11 and 2.12 show some results for the 18 December event with comparison to a visual identification of the MIZ. The agreement is reasonable, although the ice edge location is slightly off in the Radarsat-2 image (Fig. 2.11), and there are a couple of small areas of MYI identified which should be either MIZ or water.

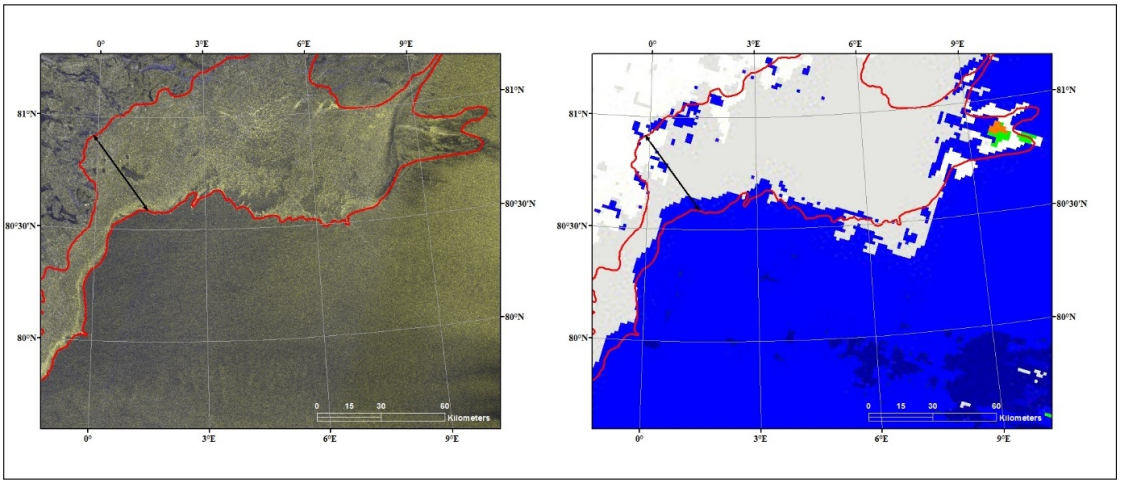

Figure 2.11: **Left**: original SAR image (Mohamed Babiker). **Right**: result of ice classification with SVM (Natalia Zakhvatkina, Anna Vesman, Alexandra Mushta); white=FYI, green=MYI, grey=MIZ, blue=water. The **red** lines denote the estimated boundary of the MIZ in the original image. The **black** line has length 43.5km.

In this overview of the Radarsat-2 image, the MIZ has an approximate width of 43.5 km. To both SAR image and SVM product, an hand-drawn visual estimate of the MIZ extent is overlaid.

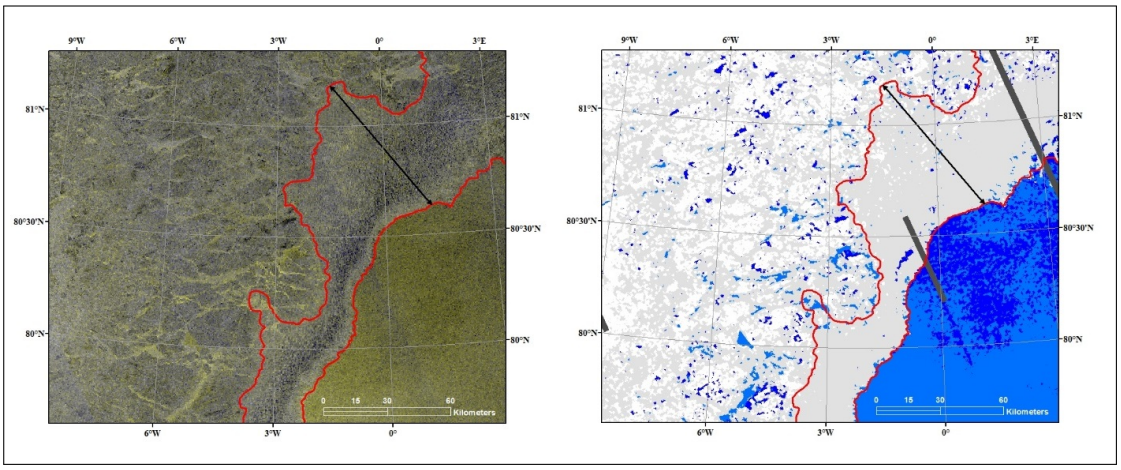

Figure 2.12: **Left**: original SAR image (Mohamed Babiker). **Right**: result of ice classification with SVM (Natalia Zakhvatkina, Anna Vesman, Alexandra Mushta). The **red** lines denote the estimated boundary of the MIZ in the original image. The **black** line has length 73.5km.

Here, an overview of the Sentinel-1 image, with an approximate MIZ width of 73.5 km. Again, the SVM ice classification is shown on the right with an hand-drawn visual estimate of the MIZ extent overlaid on both figures. This MIZ width

is comparable to the model average width of 93 km, but a more detailed comparison should be done, for instance by considering a smaller area in the calculation from the model and calculating the MIZ width from the SAR image using the same method.

Chapter 3

Analysis of Marginal Ice Zone Data

The analysis of the marginal sea ice zone (MIZ) and subsequently the definition of Ice edge for sea ice has always been subject of discussion in the scientific community. As defined in section 1.1.3, the MIZ is the region of an ice cover affected by waves and swell penetrating into the ice from the open ocean. Unfortunately waves travelling in ice infested water are extremely difficult to detect (only with in-situ measurements or high quality SAR images). A significant consequence of this is the decrease of quality for validation of sea ice models especially when wave induced break of the sea ice is considered.

This issue was approached investigating metrics for evaluating and characterising model results focusing on sea ice extent and MIZ width. Standard information such as the extent and location of the MIZ can be calculated from observations and model ice concentration and from modeled floe size distribution. Width analysis proved to be more challenging. The canonical problem is the definition of width of an irregular shape given available extra information about its boundaries (e.g. ice edge, pack ice or land). First a Laplacian method, already used in literature, was implemented but this proved too difficult to get to work (to converge) since OSIM produces a large variety of shapes as opposed to said studies which focused on a bigger scale working with lower resolutions [Strong, 2012]. Another downside of this method was the sensitivity to errors in the boundary classification, for instance the edge of a polynya (water surrounded by pack ice) was seen as the "main" ice edge.

In the end a less sophisticated but more robust model referred to as PCA method was developed. This considered the average ice edge direction (on a stereographic projection) measuring successive widths travelling in the perpendicular direction.

3.1 Polygons definition

The first step into MIZ analysis is its localization for a specific dataset. Using the definitions given in section 1.1.5 for ice concentration (IC), the data is divided into open water, MIZ and pack ice (same process can be done using the FSD 1.1.4). Now the modified data does not represent IC (or FSD) but is a 3 value array with values 0,1,2 representing, respectively, open water, MIZ and pack ice. The MIZ is formed by the collection of irregular polygons with value 1 referred to as *MIZ polygons* (in **light green** on fig. 3.3 and 3.5). These MIZ polygons are defined using a *marching square* algorithm applied to the modified array.

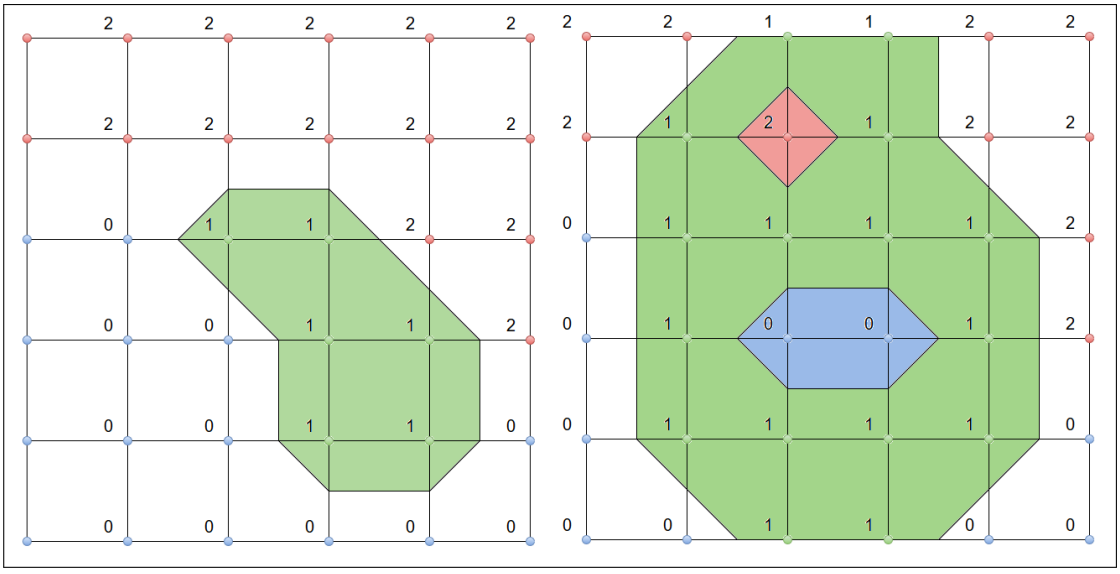

Figure 3.1: Marching square algorithm applied on arbitrary arrays. **Left** a simply-connected polygon; **Right** polygon with a polynya (considered as open water) and a pack ice inner sections, these are still considered part of the polygon. This issue is still unsolved; however, these inner areas are usually smaller than 5% of the polygon's area and have been witnessed only a few times in the whole melting season.

The marching squares algorithm aims at drawing lines between interpolated

values along the edges of a square, considering given weights of the corners and a reference value. Each point of this grid has a weight and for MIZ polygons recognition, the reference values used were 0.5 and 1.5 (since MIZ polygons are defined by grid weight of 1). To draw the curve whose value is constant and equals the reference one, a linear interpolation was used. In order to display these curves, each square of the grid was considered individually. For this method, 16 configurations have been enumerated which allows the representation of all kinds of lines in 2D space.

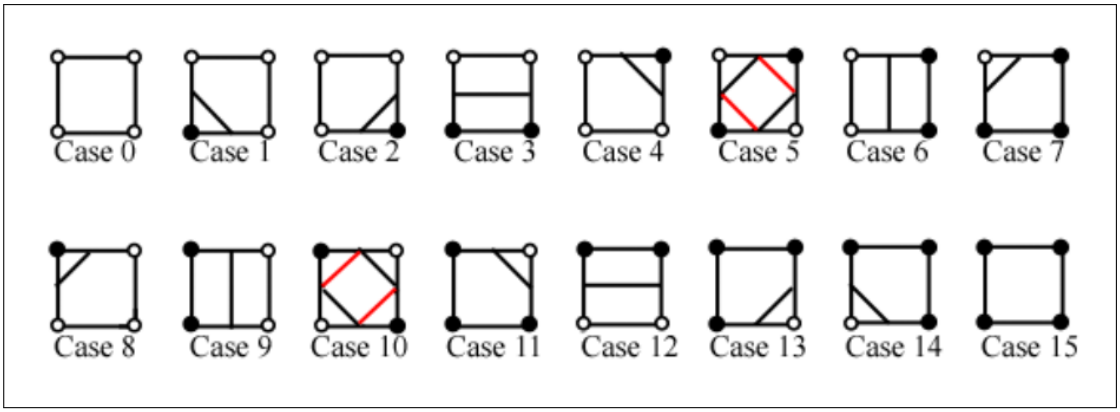

Figure 3.2: White points are weight based selected points, black points are cut off.

Mathematically speaking, MIZ polygons can be defined, for the first example, as portions of plane of value 1 enclosed by one polygonal-chain closed and simple (does not intersect nor self-intersect), for the second example as an homeomorphic holed disk enclosing points of value 1.

As introduced before, this study will focus on two regions: the Barents and Kara Seas (*bar*) and Greenland Sea (Fram Strait) (*gre*). After a polygon has been geographically localized, a process will define the nature of its perimeter. This can either be classified as **open water**, **pack ice** or **unknown** which is land or the boundary of the data set.

This operation can be performed both on OSISAF and OSIM+WIM, using either ice concentration or floe size distribution data. In fig. 3.3 ice concentration model data in the Barents and Kara Seas region is transformed. For this specific dataset 19 MIZ polygons were detected:

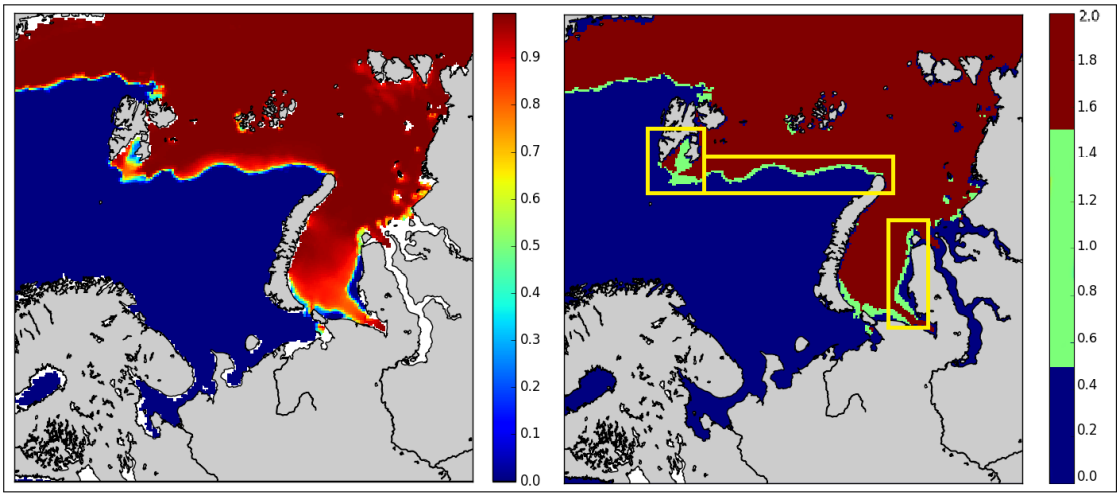

Figure 3.3: **Left**, OSIM+WIM ice concentration data from 11-05-2015. **Right** processed data into 3 value array. In **light green**, the collection of irregular polygons forming the MIZ. Highlighted in **yellow** the polygons of fig. 3.4.

In fig. 3.4 a closer look at polygons 14, 16 and 17 from ice concentration model data of 15-05-2015. Area and perimeter come from the calculation of number of grid points multiplied by the resolution ($10 \times 10\ km$ for OSISAF, $12.5 \times 12.5\ km$ for OSIM+WIM).

Polygon 14 is a class B polygon (area of 24453 km^2 and perimeter of 1045.0 km), it is a clear example of the deficit of the polygon definition algorithm where some of pack ice and some land is mistakenly confused as MIZ. This issue has not yet been tackled; however, MIZ polygons are treated and analysed as an averaged collection suggesting that small errors like this one could not significantly modify the results.

Polygon 16 is a class B polygon (area of 14922 km^2 and a perimeter of 1255.3 km), another issue is presented with this polygon where a landfast MIZ polygon (upper part) is connected to the bottom drift MIZ polygon.

Finally polygon 17 is a class H polygon (area of 21797 km^2 and a perimeter of 2319.2 km), it represents the most classical definition of MIZ, located between the pack ice and the open ocean is the first ice encountered by incoming waves from the Barents sea, has a narrow shape and does not show any error related to the marching squares algorithm.

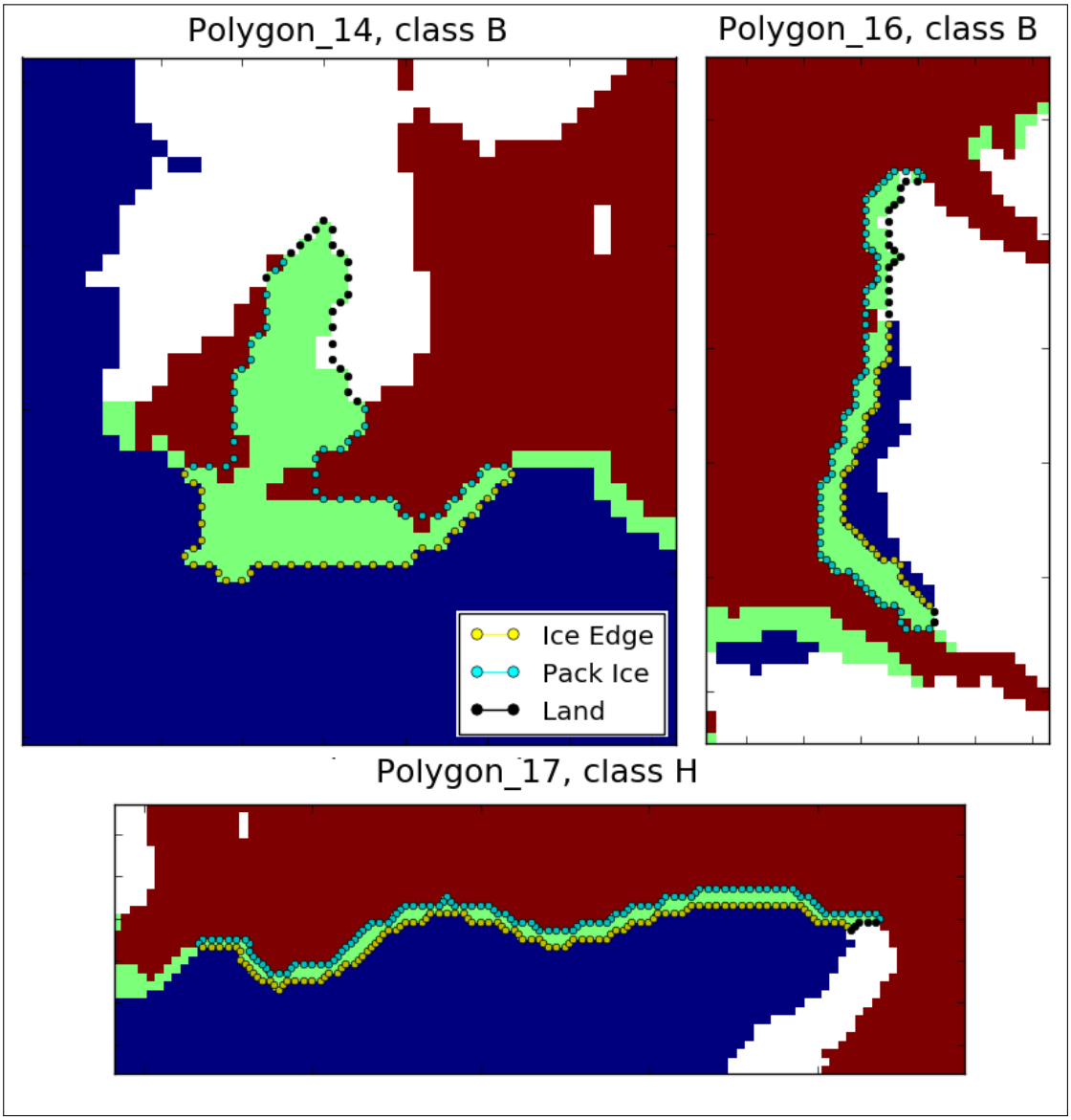

Figure 3.4: Close up of polygons 8,16 and 17 from OSIM+WIM processed data.

In fig. 3.5 the same operation on OSISAF ice concentration observational data in the Fram Strait (Greenland) region. For this dataset and region, 5 polygons were detected:

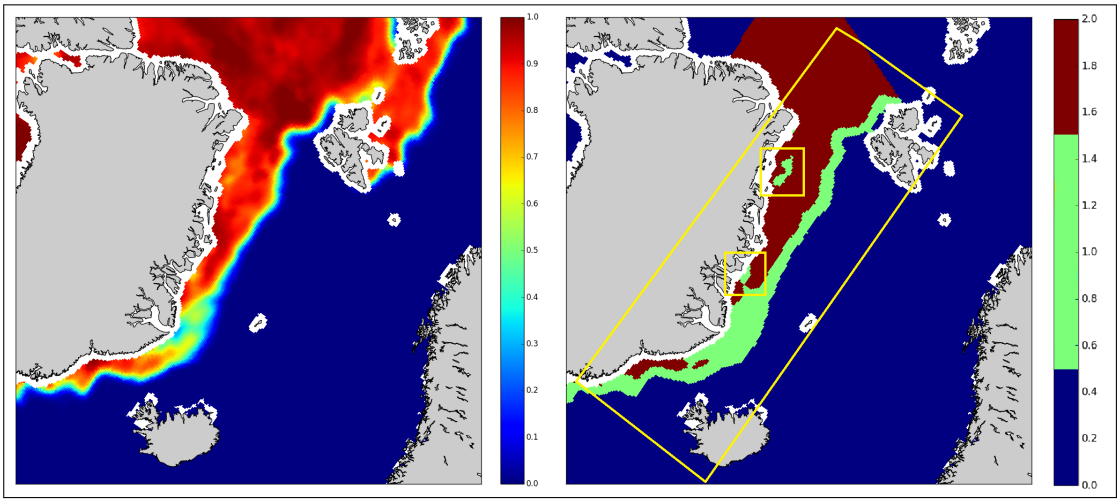

Figure 3.5: **Left**, OSISAF ice concentration data from 20-04-2015. **Right** processed data into 3 value array. MIZ polygons are in **light green** and highlighted in **yellow** the polygons of fig. 3.6.

In fig. 3.6 are showed polygons 2,3 and 4 from OSISAF ice concentration data of 20-04-2015. Polygon 2 is a class M polygon (area 4921.9 km^2 and perimeter 341.4 km). The polygon is correctly identified.

Polygon 3 is too a class M polygon (area 1273.4 km^2 and perimeter 625.5 km) it is completely surrounded by pack ice but is still considered as MIZ because of the low ice concentration. Hence, the possibility to break-up from wave induced stresses.

Polygon 4 is a class H polygon (area 431020 km^2 and perimeter of 9578.0 km), this is a massive polygon running from the Svalbard to the Fram Strait (in between Greenland and Iceland). This channel, as explained in appendix A.2, is the main and deepest connection between the Arctic ice cover and the open oceans. It is often characterised by broken floes drifting south and eventually disappear, a process extremely pronounced in the melting season [Kwok, 2005]. Another particular feature of this polygon is that it includes a pack ice area. This is an issue already introduced in the first part of this chapter and still unresolved.

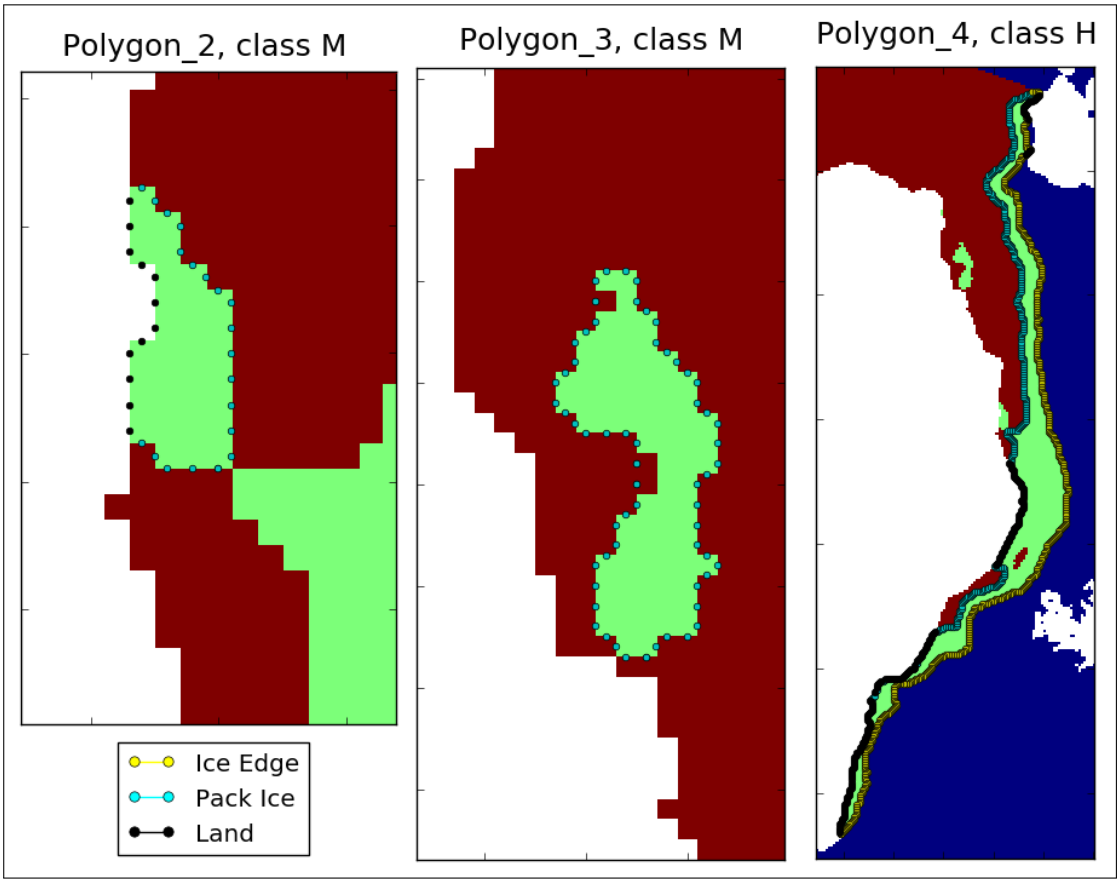

Figure 3.6: Close up of polygons 2,3 and 4 from OSISAF processed data.

3.1.1 Polygons statistics

As seen in the previous examples (fig. 3.4 and 3.6) however, their appearance is related to their original dataset. Qualitatively, it can be seen that the OSISAF concentrations are much more spatially heterogeneous, especially in the melting season while OSIM is close to being a binary function. Such behaviour leads the definition algorithm to divide the MIZ in many small polygons rather that considering a smooth wide area as with OSISAF.

For OSISAF the number of polygons is generally lower. The Barents and Kara seas region manifests an average of 14 polygons per day are detected with a maximum of 27 (19-03-2015). With more than 20 polygons per day during early season (March,April and May), a decreasing trend brings the number of daily polygons below 10 for late melting season (August and September). For the Fram Strait (Greenland) region however an average of 11 polygons per day is found with a maximum of 18 in middle melting season (June and July). The number of poly-

gons is always around 10 independently of the period.

For OSIM in the Barents and Kara seas region, an average of 15 polygons have been detected with a maximum of 47 (11-03-2015). In early melting season more than 30 polygons per day are often found. This number slowly decrease until late melting season were less than 10 polygons per day are detected. In the Fram Strait (Greenland) region the average is of 12 polygons with a maximum of 27 (15-04-2015). The trend is similar to the other region with around 20 polygons per day for early melting season that slowly decrease till less then 10 per day during late melting season.

3.2 The Principal Components Analysis

The **Principal Component Analysis** (**PCA**) (renowned as Empirical Orthogonal Functions (EOF) in meteorological science) is a statistical procedure which converts, using an orthogonal linear transformation, a set of possibly correlated observations into a set of linear uncorrelated variables, the **Principal Components** (**PC**). With such operation, the first principal component has the largest possible variance (accounting for as much of the variability as possible) and each succeeding one in turn has the highest variance possible under the constraint of orthogonality to the preceding components. The resulting vectors are an uncorrelated orthogonal basis set given they are eigenvectors of the covariance matrix, which is symmetric. Considered the MIZ as a collection of sets of points, for each collection a set of 2 principal components can be calculated.

The set of points locating the Open Ocean border in longitude (x) and latitude (y) are first projected onto the plane (x, y) using a suitable stereographic projection. If the earth is taken to be spherical then the projection will be a conformal mapping — i.e. angles (particularly orthogonality) will be preserved. The collection of m points (in the $m \times 2$ matrix $\mathbf{X}$) are reprocessed to have a null mean:

$$\tilde{\mathbf{X}} = \begin{bmatrix} x_1 - \bar{x} & y_1 - \bar{y} \\ x_2 - \bar{x} & y_2 - \bar{y} \\ \vdots & \vdots \\ x_m - \bar{x} & y_m - \bar{y} \end{bmatrix} \tag{3.1}$$

The PCA is defined by a set of two 2-dimensional unit basis vectors $\mathbf{w}_k$ ($k = 1, 2$) that map the row vectors $\mathbf{x}_i = (x_i - \bar{x}, y_i - \bar{y})$ of $\tilde{X}$ to a new matrix of principal components $\mathbf{T} = [t_{i,k}]$ given by:

$$t_{i,k} = \mathbf{x}_i \cdot \mathbf{w}_k, \quad \text{or} \quad \mathbf{x}_i = \sum_{k=1}^{2} t_{i,k}\mathbf{w}_k = \sum_{k=1}^{2} \mathbf{t}_k^{(i)}. \tag{3.2}$$

For the first principal component to inherit the maximum possible variance from $\mathbf{x}$, the following needs to be maximised:

$$\begin{aligned} \sigma_1^2 &= \frac{1}{m}\sum_{i=1}^{m} \left|\mathbf{t}_1^{(i)}\right|^2 = \frac{1}{m}\mathbf{w}_1^T\tilde{\mathbf{X}}^T\tilde{\mathbf{X}}\mathbf{w}_1 \\ &= \frac{\mathbf{w}_1^T\tilde{\mathbf{X}}^T\tilde{\mathbf{X}}\mathbf{w}_1}{m\mathbf{w}_1^T\mathbf{w}_1} \end{aligned} \tag{3.3}$$

(since $|\mathbf{w}_1| = 1$). Now, it is a standard result for a symmetric matrix such as the covariance matrix $\mathbf{C} = \tilde{\mathbf{X}}^T\tilde{\mathbf{X}}/m$ that the maximum value of (3.3) is the largest eigenvalue of $\mathbf{C}$, which occurs when $\mathbf{w}_1$ is the corresponding eigenvector — i.e. $\mathbf{C}\mathbf{w}_1 = \lambda_1\mathbf{w}_1$.

Similarly, the second component is determined from the remaining eigenvector of $\mathbf{C}$ ($\mathbf{C}\mathbf{w}_2 = \lambda_2\mathbf{w}_2$, where $\lambda_2 < \lambda_1$). This component is the one used to orient the calculations of the polygon widths.

In general (including for vector spaces with higher dimension than 2), the full principal components decomposition of $\tilde{\mathbf{X}}$ can be given as:

$$\mathbf{T} = \tilde{\mathbf{X}}\mathbf{W} \tag{3.4}$$

where $\mathbf{W}$ is the matrix whose columns are the eigenvectors of $\mathbf{C}$.

3.3 Characterization of the MIZ

The MIZ was studied for the 2015 melting period using ice concentration (IC) observations and model data. The behaviour of MIZ extent ($15 < IC < 80$), MIZ width using the PCA method and MIZ localization are shown and inter-compared. Sea ice and MIZ extent are calculated multiplying the value of ice concentration times the resolution of the grid cell (12.5×12.5 for the WIM and 10×10 for OSISAF). MIZ localization comes from an area weighted average of each MIZ polygon's centroid.

Results for the 2015 melting season show different behaviours during 3 distinct periods. The first one, referred to as *early* season goes from March to mid May (15-05-2015), the *mid* season from 15-05-2015 till the first days of September (1-10-2015) and the *late* season in September.

3.3.1 Barents and Kara Seas Region (BKR)

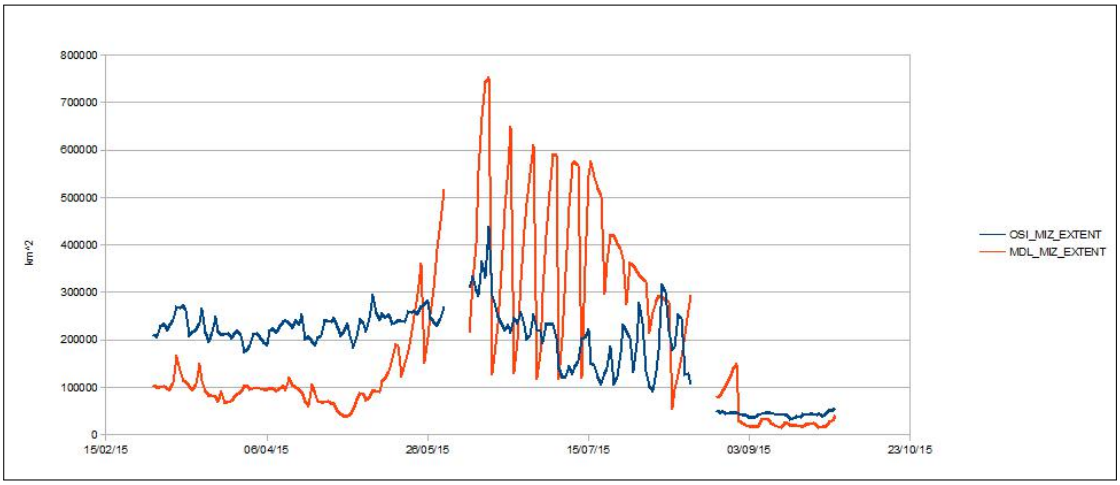

Figure 3.7

The MIZ shows 3 clear and distinct behaviours for the 3 melting periods. An average underestimation of $-134.5 \cdot 10^3\ km^2$ for the early season is, in fact, followed by an erratic behaviour for the mid season. OSIM tends to heavily overestimate MIZ extent until a new restart is given (at the beginning of every week). This is clearly a reinitialization problem but surely the model suffers from reduced ice melting where the MIZ grows (ice less and less compact) without melting away

until a new restart corrects the difference (average difference $118.2 \cdot 10^3\ km^2$ but extreme variability). This problem is related to the MIZ itself since sea ice extent does not seem to be affected by such periodic behaviour. The late season manifest an overall underestimation of the MIZ with an average difference of $-20.4 \cdot 10^3\ km^2$.

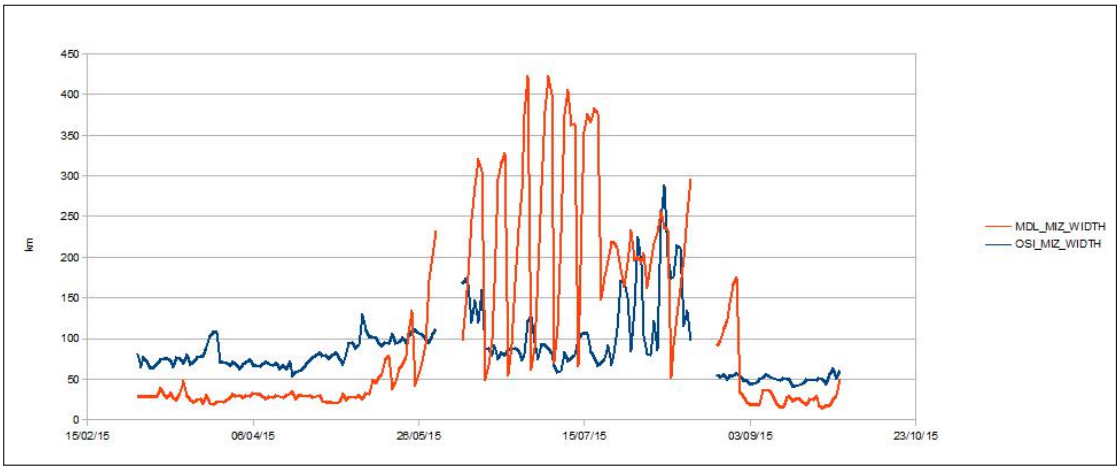

Figure 3.8

As with the extent, also MIZ width, calculated using the method explained in section 3.2, manifest the same periodic behaviour in mid season. The average difference with observational widths is $-48\ km$ for the early season, $82\ km$ in the mid season (with very high variability) and $-25\ km$ in late season.

Figure 3.9

The average longitude and latitude show, however, a great correlation. The average difference for longitude goes from $-3.2°$ (early) to $-1.8°$ (mid) till $0.1°$ is reached in late season. Latitude showed average differences of $-1.7°$ (early), $1.3°$

(mid) and $-0.2°$ (late), it also shows the north-wise drift of the MIZ typical of sea ice retreat for the melting season while at the same time is being affected by the mid-season periodical reinitialization issue.

3.3.2 Fram Strait Region (FSR)

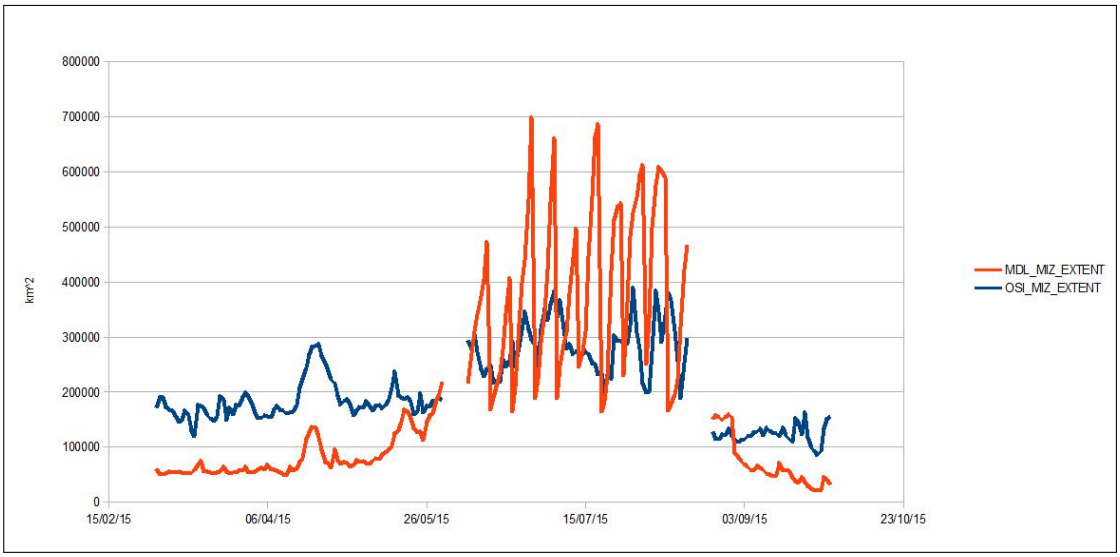

Figure 3.10

As with its analogy in the BKR, the MIZ in the Fram Strait behaves very differently for its 3 periods. The early melting season is still characterized by an average underestimation of $-113.6 \cdot 10^3\ km^2$. This is followed by the already seen periodic behaviour that even in this case is related to the reinitialization problem (average difference $68.1 \cdot 10^3\ km^2$ again with extreme variability). The high temperatures of the mid melting period slowly decrease till September where late melting season starts accompanied by an overall underestimation of the MIZ with an average difference of $-76.3 \cdot 10^3\ km^2$.

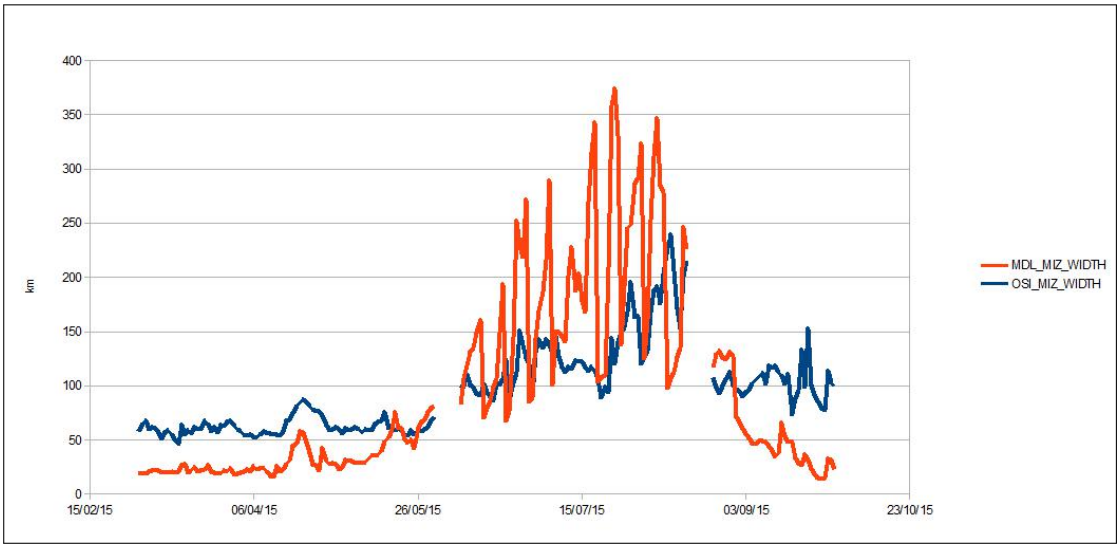

Figure 3.11

Same results are found for the MIZ width. The average difference with observational widths is $-35\ km$ for the early season, $40\ km$ in the mid season (very high variability) and $-65\ km$ in late season. Another notable fact is that MIZ average width is affected by a significant decrease at the beginning of late melting period while its behaviour seems less correlated to observations than in the early season.

From the 18th to the 20nd of April, MIZ extent and width of both models and observations show a significant increase, this is due the formation of a weak zone in the more exposed ice cover of the Greenland region. OSIM follows this behaviour; however, ice extent is still underestimated while ice concentration tends to be too homogeneous when compared to observations'.

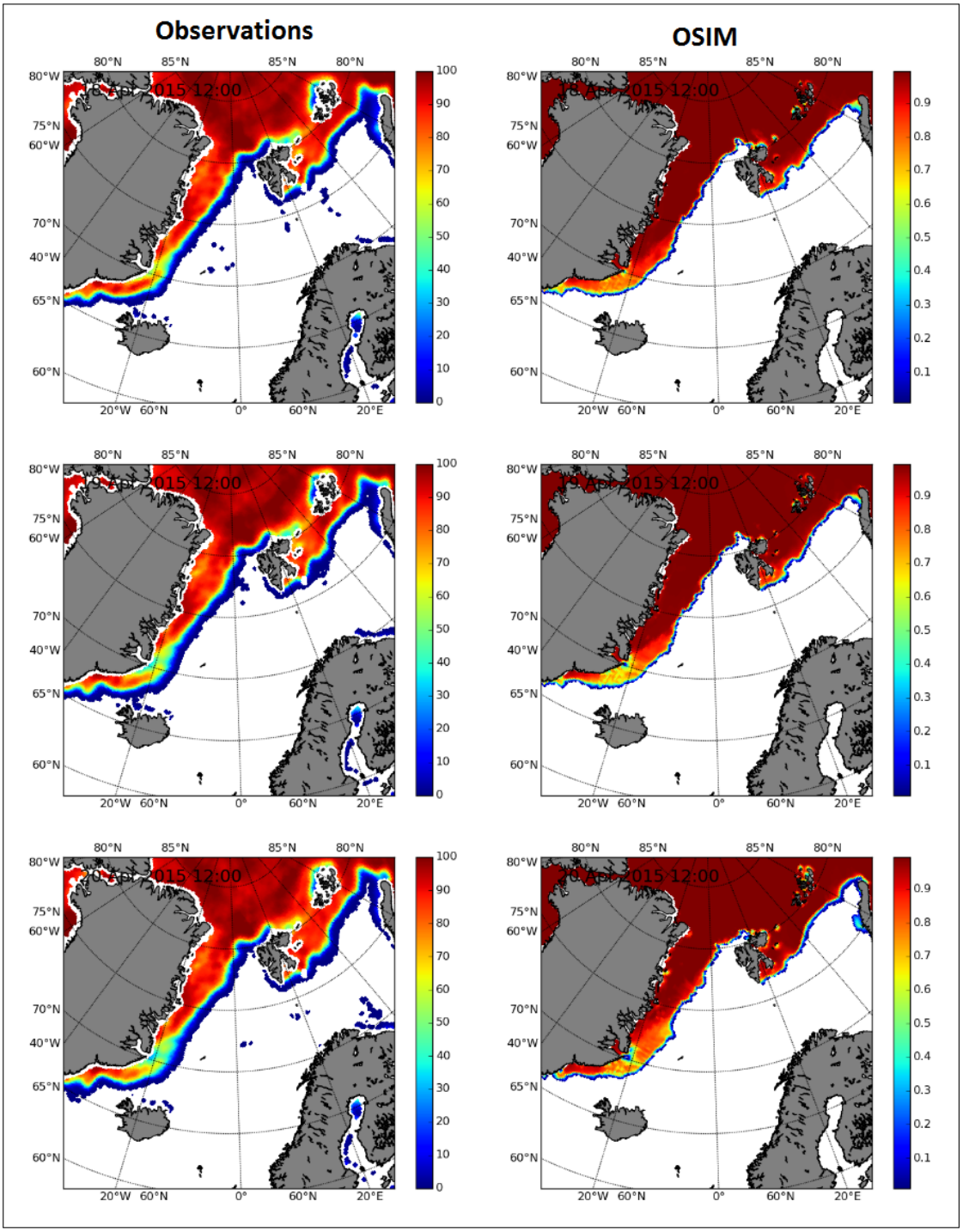

Figure 3.12: In 7 days (18th to 25th of April) the most exposed MIZ of the Greenland region (Denmark Strait) is subject of heavy melting. These figures are a clear example of the different (more sharp) behaviour of OSIM.

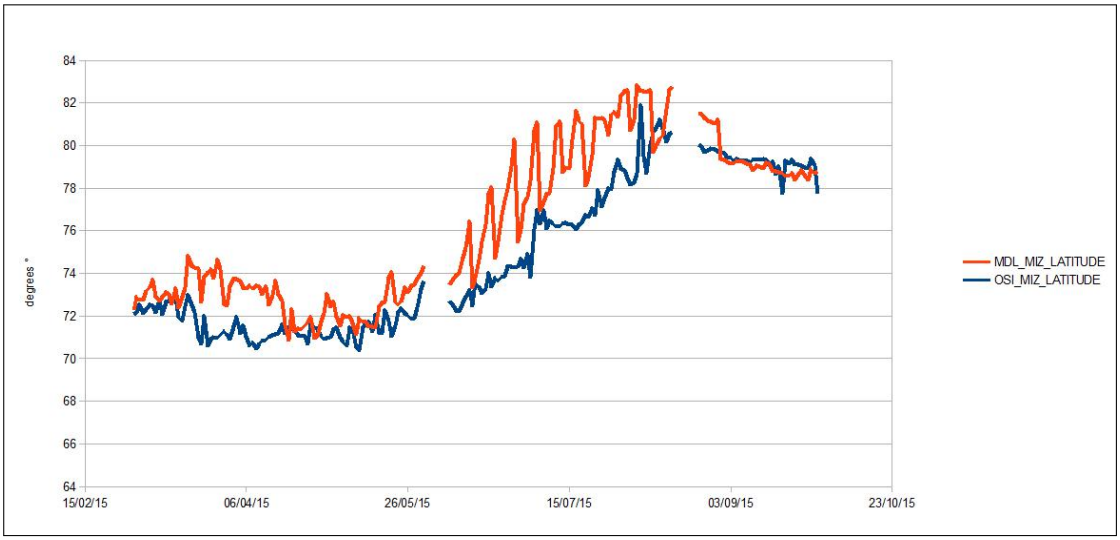

Figure 3.13

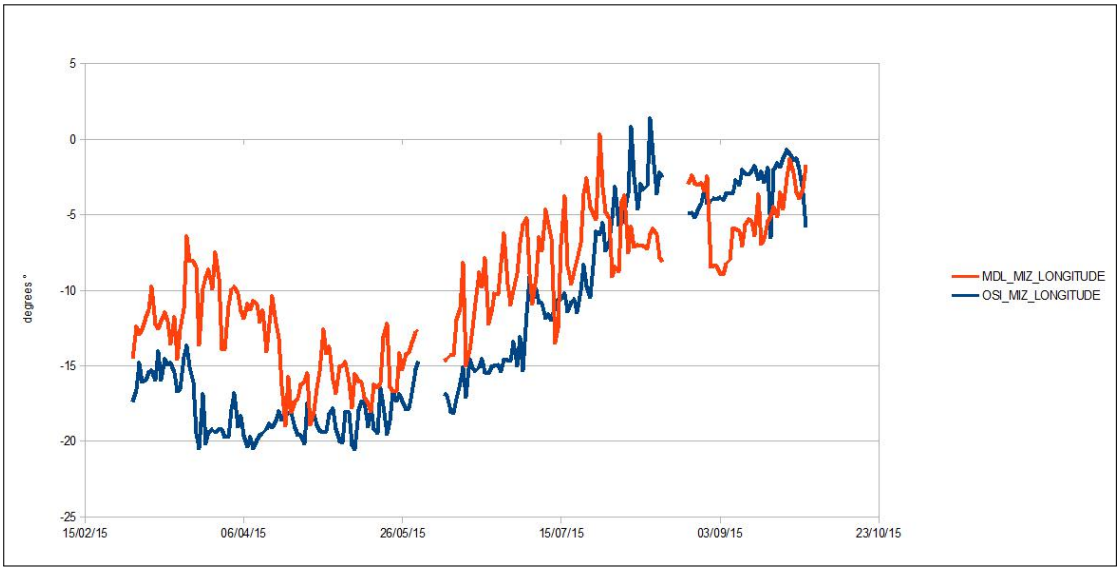

Figure 3.14

Again the average longitude and latitude look similar, at least both showing a north-east retreat, typical of sea ice in the Fram Strait. Average difference for longitude are 4.9° (early), 2.0° (mid) and −2.6° (late). For latitude 1.3° (early), 2.2° (mid) and −0.2° (late). While both are generally overestimating MIZ location, it is notable how both show a sudden decrease for the beginning of the late melting season.

3.4 Model Observations Inter-comparison

Another possible application of the PCA method explained in section 3.2 is for ice edge inter-comparison. In this case the collection of polygons do not represent the MIZ. Instead, they are the differences between the model and observations ice extent. This is achieved in a 2-step process. The array representing the ice concentration (IC) data ranging from 0 to 1 is transformed into a binary array with values 1 for $IC > .15$ and 0 for $IC < .15$.

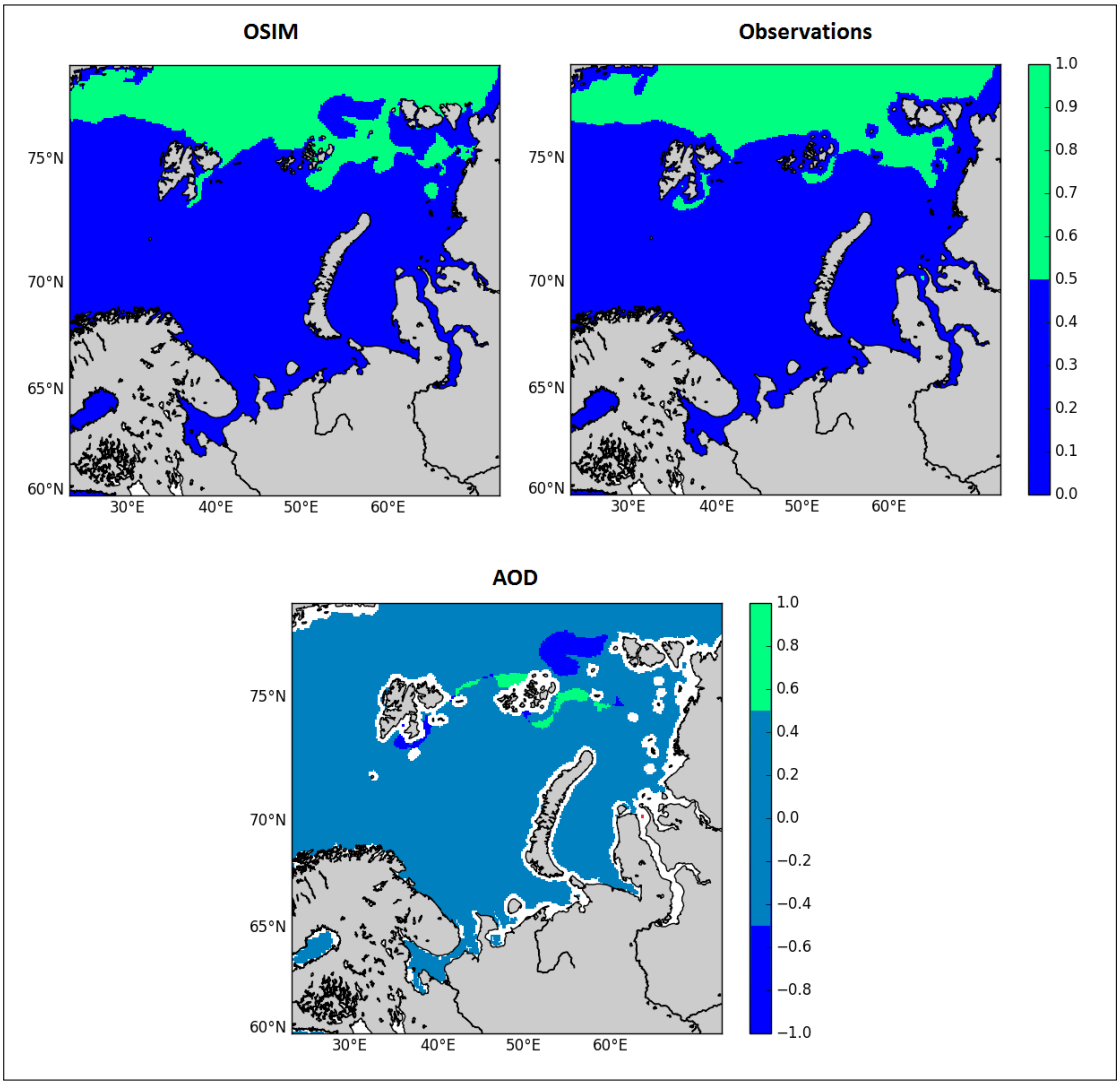

Figure 3.15: An example of AOD derivation. **Top left** is OSIM's modified dataset, **top right** observations'. **Below** the difference between OSIM and observations. Data from 18-07-2015 in the Barents and Kara seas region

This operation is done on both datasets, model and observation. The model is

then reprojected onto the observation grid using a linear interpolation method and the difference of the two is taken. The result is referred to as Area Of Difference (AOD), its values are 1 for overestimation of OSIM compared to the observed ice extent (*overestimation polygon*), -1 for underestimation (*underestimation polygon*) and 0 for agreement. The average of the widths of the polygons forming the AOD is thus a mean difference between the dataset's ice edges.

Results are presented using extension and width of the Overestimation and Underestimation polygons. For the extent, every point was multiplied by OSISAF's grid resolution (10×10 km). These results give general information about the difference between model's and observations' ice extent. The widths come from the PCA analysis but with a significant difference, since these polygons do not represent the MIZ, there is no unique ice edge to use for PC derivation. In this case it was used the ice edge of the observations for underestimation polygons, of the model for overestimation ones.

3.4.1 Barents and Kara Seas Region (BKR)

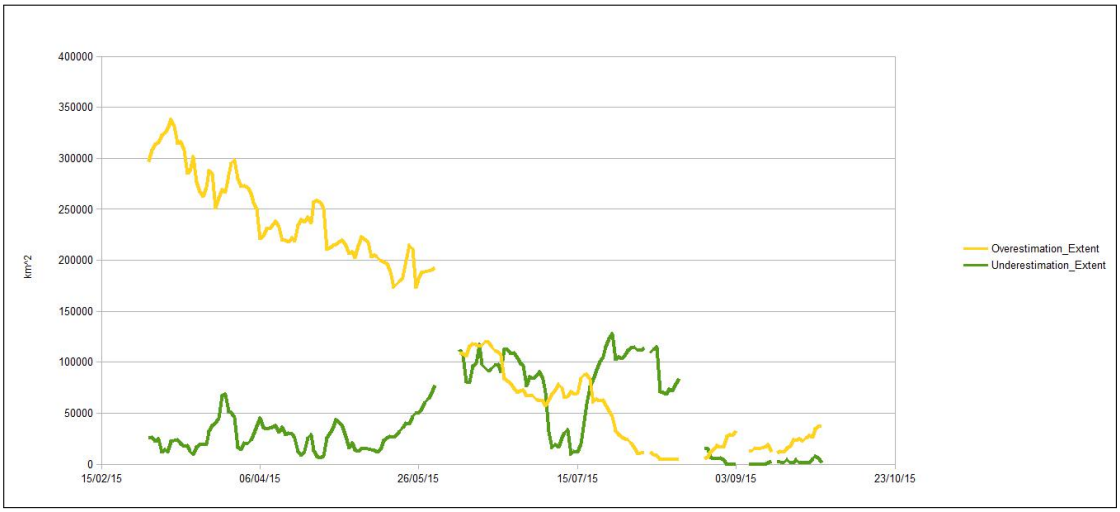

Figure 3.16

OSIM starts with a general overestimation of sea ice extent characterized by a negative trend decreasing as melting season advances. Underestimation becomes significant (when compared to overestimation) only during mid-late melting season (June,July and August). However, OSIM's summer months are affected by a still

unsolved issue on reinitialization possibly jeopardizing such results (see section 3.3).

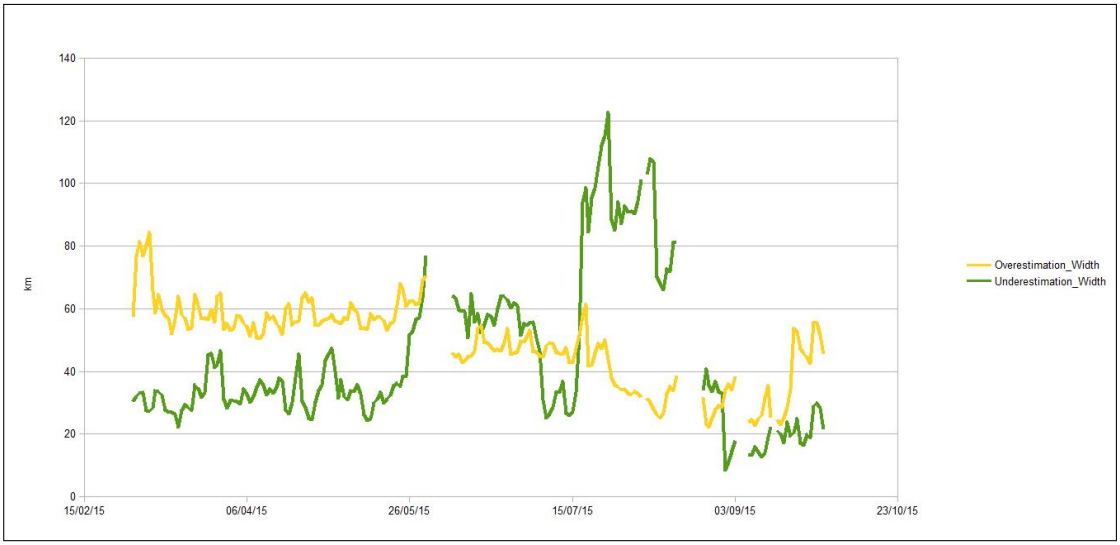

Figure 3.17

As for the widths, underestimation widths have generally lower values than overestimation ones. This may suggest that underestimation polygons are stretched throughout the ice-edge following its shape . Overestimations on the other end are characterized by higher widths for early season slowly decreasing till the beginning of September. As melting season advances, air and sea get warmer, sea ice retreats and overestimation polygons get smaller and smaller while underestimation ones grow into more irregular shapes.

3.4 Model Observations Inter-comparison

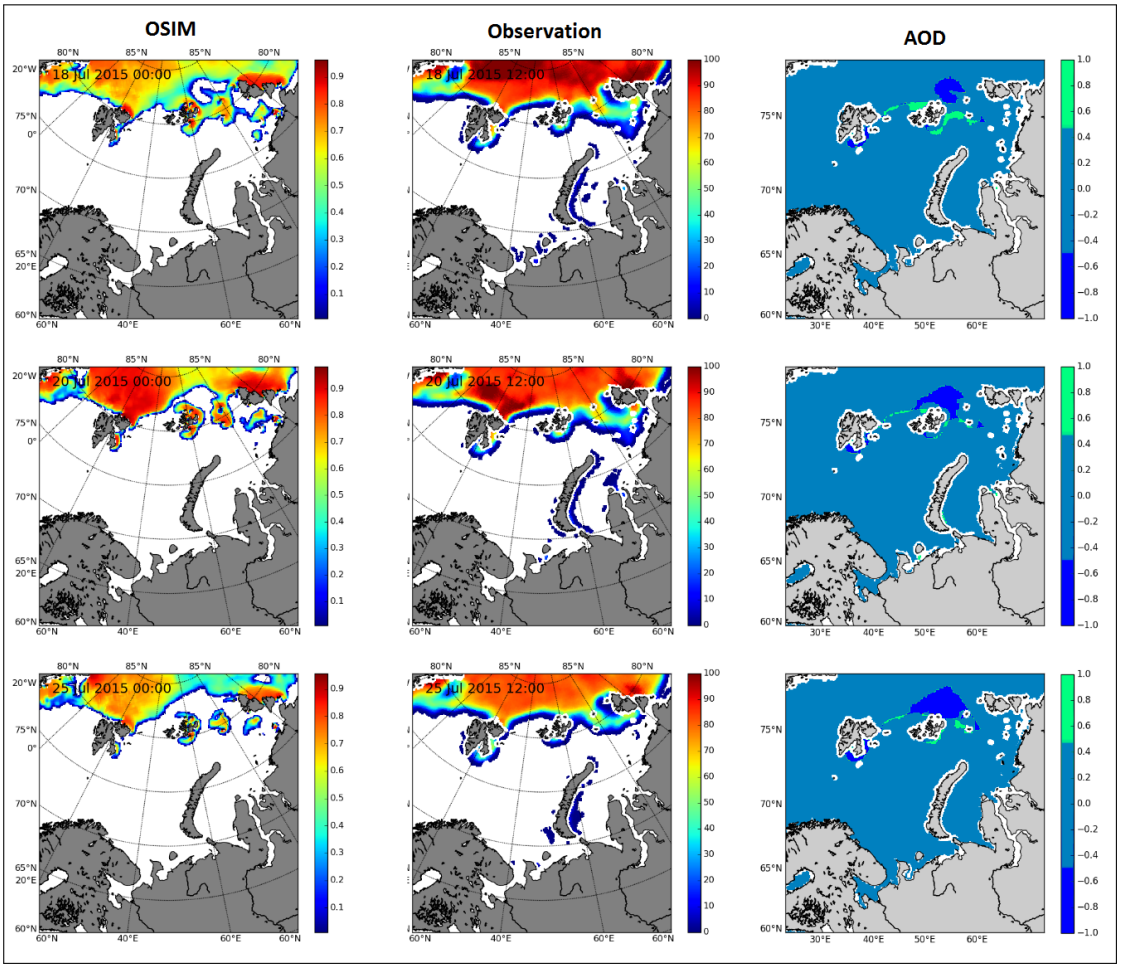

Figure 3.18: 3 days showing the excessive melting of model's sea ice and

As shown in fig. 3.18, the regime changes from general overestimation to underestimation extent (18th to 25th of July). Particularly interesting is the formation of a c-shaped polynya in the north-east side of the Barents sea with the consequent loss of sea ice by the model and peaked underestimation when compared to the observations.

3.4.2 Fram Strait Region (FSR)

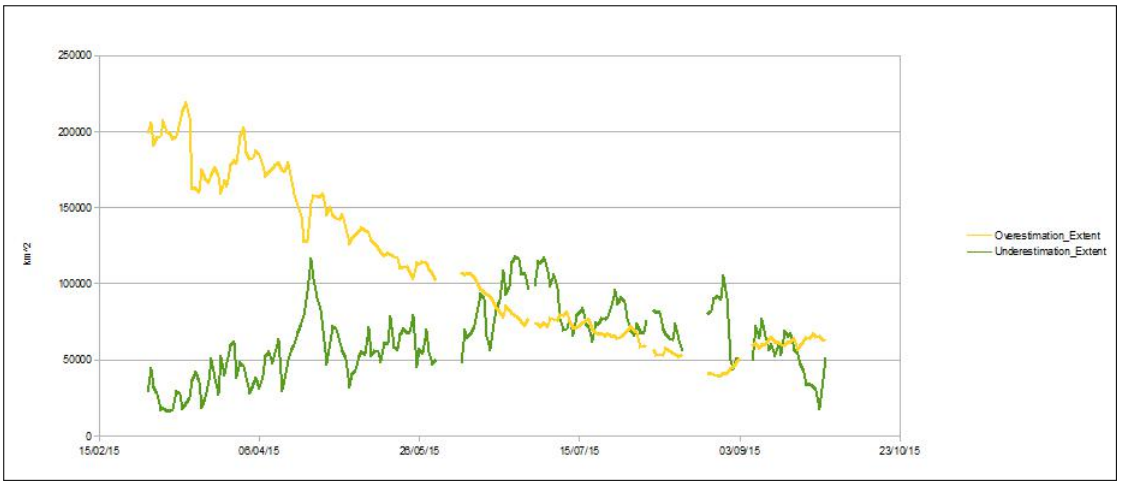

Figure 3.19

Similar results are found for the Fram Strait region where a general overestimation is followed by an overall underestimation in early July.

Figure 3.20

Widths in this case are almost constant all season for the overestimations while underestimation polygons show increased widths after mid season. This is probably related to the high currents and fast flow of drift ice through the Fram Strait in Summer. Given the fast-changing dynamics of such region (see appendix A.2) it is expected a general underestimation once ice gets weaker and more subject to break-up, drift and melt.

It is clear from the charts presented in this section that more data is missing for this analysis. This is due to some corrupted observation data. Such corruption will not influence the analysis 3.3 which is limited to the MIZ (i.e. excluding missing values) but produces false overestimation polygons and was thus excluded.

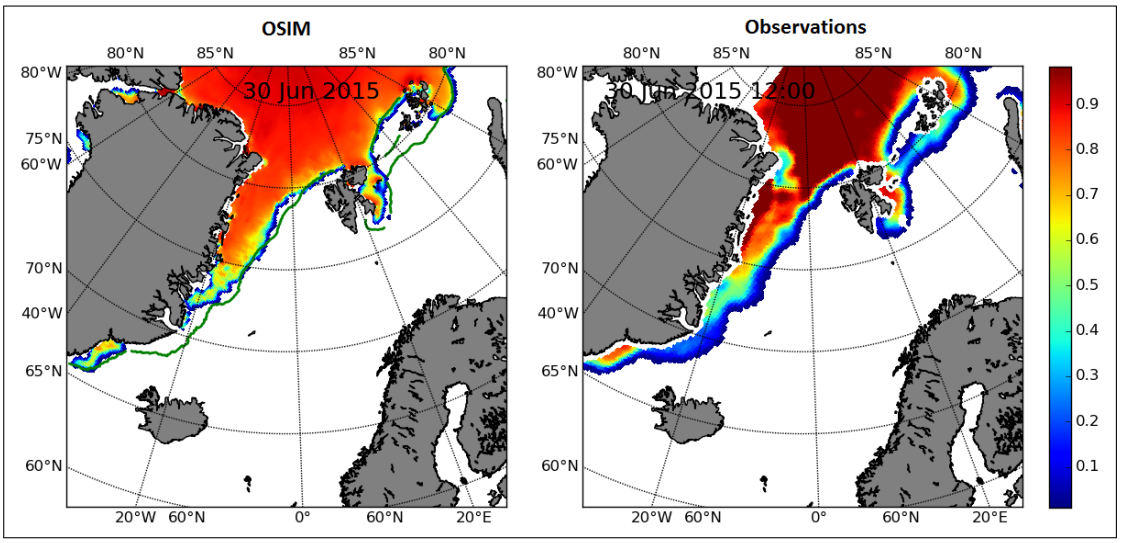

Figure 3.21: Ice concentration data from OSIM and observations for 30/06/2015. In **green** the ice edge for observations is projected over OSIM. In the **top left** of the observations the missing data can be clearly seen (probably for a corrupted satellite swath).

3.5 FSD MIZ qualitative comparison

In the following MIZ polygons derived from FSD are studied and compared with OSISAF ice concentration MIZ polygons. Since these MIZ polygons come from different parameters, such comparison has no real value quantitatively, however, qualitatively it is an opportunity to assess the relation between modeled FSD and ice concentration.

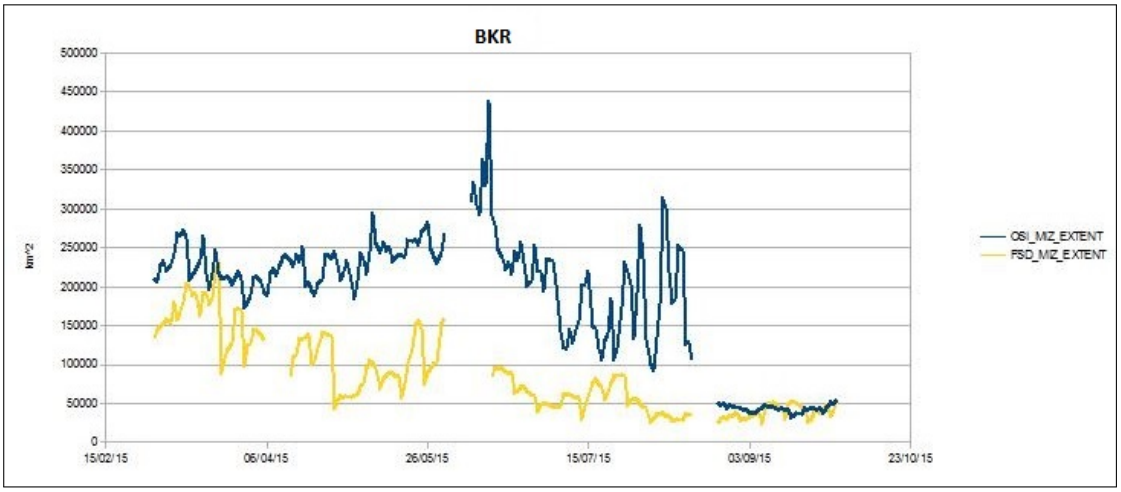

Figure 3.22

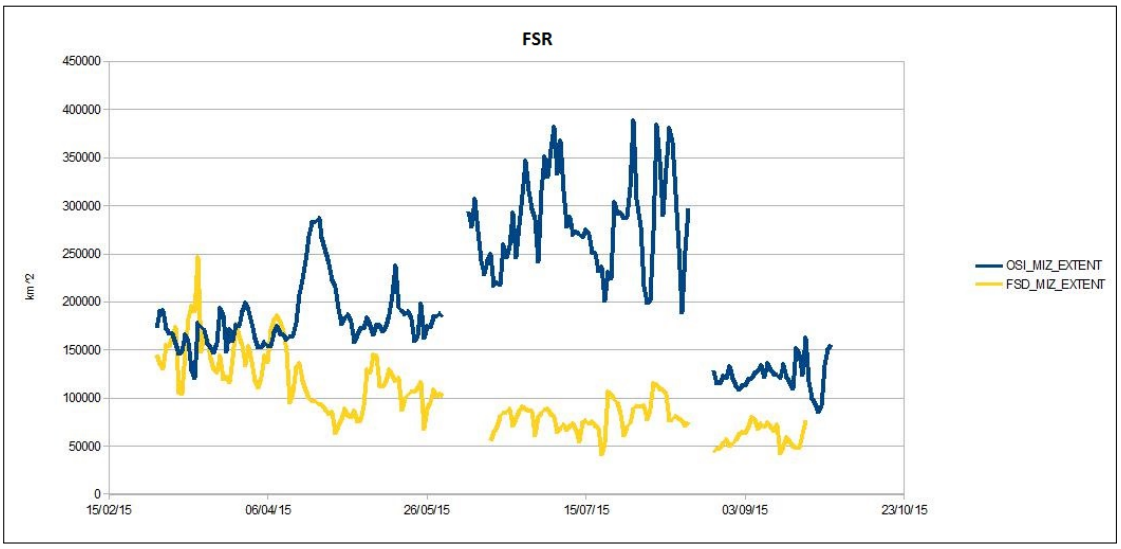

Figure 3.23

For both regions the FSD MIZ and IC MIZ behave very differently assuming very different values in their extension, however, in both cases September is characterized by less difference, almost none for the Barents and Kara sea region. This may suggest that during melting season ice concentration tends to decrease but without the presence of strong wave motion the overall FSD will be characterised by big floes; as September reaches among the highest water and air temperature (hence minimum sea ice extent) said floes will eventually melt. This is not an uncommon process and may give a good explanation to the late melting period similarity between measured MIZ extents.

Chapter 4

Conclusions

Even though all the experiments carried out for this study were done with an OSIM+WIM model configuration (see section 2.3), most of the results are related to OSIM, specifically about its MIZ. A complete validation of this model is far from being completed, however, results give some clear indications on where to look and what to optimize.

As referred to OSIM from section 3.3 it is clear that the model is affected by re-initialization shocks as every assimilation of sea ice data from the validated TOPAZ (TP4) shows an abrupt change in ice concentration not only for the MIZ but for the whole sea ice (i.e. Pack ice, fast ice). Such behaviour, discovered in this analysis leads to some drastic changes for ice prediction skill of the model. Even though massive models such as OSIM are composed by hundreds of sub-components, after this study it is safe to assume that the thermodynamic processes of the model are at fault for the erratic behaviour which characterize ice concentration in mid melting season 3.3 .

As for the WIM, in chapter 2 the uncertainties in the model are highlighted. These are the viscosity parameter (Γ) that determines the attenuation of large period waves, the breaking strain of the ice cover as well as the critical probability above which the ice will break. An additional uncertainty in the model is the amount of wave energy lost during ice breakage. To overcome such limitations sensitivity studies are required together with high resolution modelling possibly to be compared with ice charts drawn from high resolution SAR images or even better form SVN ice charts. Focusing on the WIM outputs, examples in section 2.3 show that the break-up process has indeed a sensible effect on the produced FSD

especially in the presence of strong waves. The examples taken, especially for the strong wave of the described 18th December event, represent a good starting point for WIM's validation while at the same time show how dynamic and seemingly unpredictable the MIZ is.

The main thesis development is however the PCA method for widths calculation. Even though the study was limited to the melting season and only few specific examples were given, the PCA proved to be a very good candidate not only for MIZ analysis (i.e. the width of the MIZ is directly related to the propagation of waves into the ice cover) but even for ice-edge validation. The process is still being developed but such definition of width would represent a unique and repetitive method to assess the accuracy of the model on ice edge localization independently of the user or the data. Future studies may consider the distribution of the widths and their frequency of appearance in a specific region with specific wave conditions. This may be of great interest for the study of sea ice and specifically the MIZ.

Finally, in appendix B two methods for WIM analysis are given. In B.1 the mean momentum causing wave-induced drift of floes (i.e. wave stress applied to the sea ice) is derived while on B.2 lateral and bottom melting based on floe size distribution are described. From the application of such theories into WIM-hc, the wave stresses derived were not sufficiently strong to be compared with other forcing (i.e. wind induced stress) hence they could not have a significant effect on ice drift. Wave-induced drift on ice floes is still an issue in sea-ice modeling; however, high-resolution models could be the best platforms to test this effect which is highly localized at the ice edge. As for the modified ice growth, these presented abnormally big ice formation processes (sometimes with over 15 meters of new ice per day on certain locations). In order to achieve more realistic results a deeper study of these processes is needed, specifically focusing only on the increased lateral melting already observed and described in literature.

As the study of sea ice and waves in ice infested waters continues, unique and repetitive methods of measurements for sea ice, as those proposed in this work, are undeniable tools for the assessment of modern ocean and sea ice models.

Appendices

Appendix A

Regions geographical and oceanographic characteristics

A.1 Barents/Kara region and the Fram Strait

Located in the north of Norway and in the western part of Russia, the Barents and Kara Seas are Arctic shelf seas that play and important role in the Arctic climate system even though are geographically partly restricted. A major part of the heat exchange between the Arctic Ocean and lower latitudes is, in fact, taking place in the *Fram Strait* and the Barents and Kara Sea regions, both in the ocean and in the atmosphere [Proshutinsky et al., 2005]. The local conditions in the Barents and Kara Seas strongly influence the north-south heat exchange and influence the water mass formation in the Arctic Ocean as well as large-scale atmospheric dynamics while the production, melting, and transport of sea ice set the condition for the vertical heat exchange between the atmosphere and the ocean.

There are some clear differences between the Barents Sea and the Kara Sea. While Barents Sea is directly connected to the Nordic Seas and receives warm and saline Atlantic water, Kara Sea is shield off from direct influence by Atlantic water and is subject to large inflow of fresh water from two of the Arctic's major rivers, *Ob* and *Yenisey*. Together these factors have strong influence on the local ice condition. The sealed off and less salty Kara Sea has a relatively constant ice cover during the winter season, while there are strong inter annual as well as seasonal sea ice variability in the Barents Sea [Sorteberg and Kvingedal, 2006] [Keghouche et al., 2010]. The most influential atmospheric conditions during winter seasons are low-pressure system formed in the North Atlantic, travelling north-east into

Barents Sea. These cyclones bring warm and humid air masses into high latitudes and have a strong impact on the water masses and the ice condition.

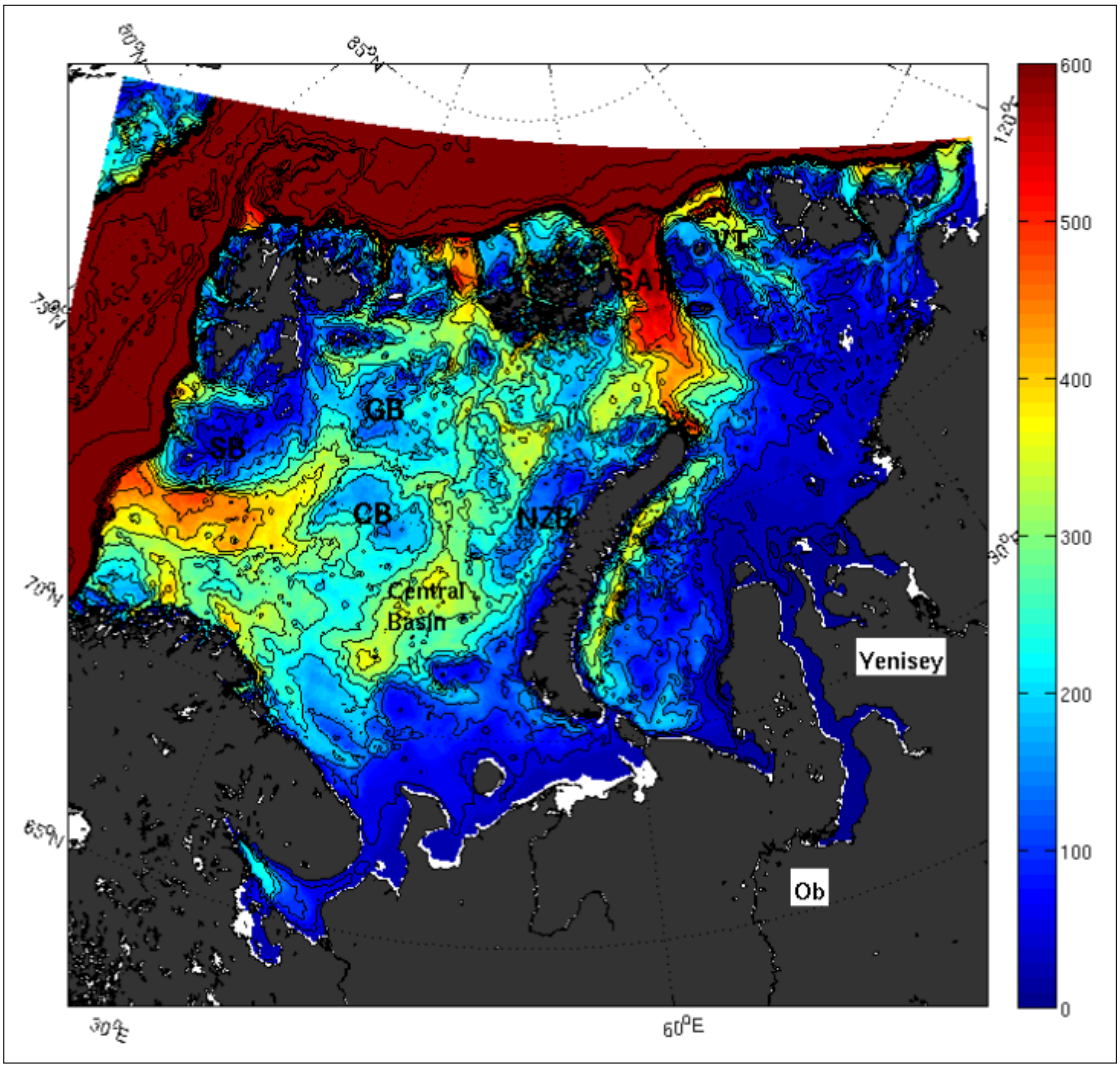

Figure A.1: Bathymetry used in the Barents and Kara Sea model, with the larges rivers, Ob and Yenisey, indicated as well as the Central Basin, Central Bank (CB), Great Bank (GB), Svalbard Bank (SB), Novaya Zemlya Bank (NZB), St. Anna Trough (ST), and Veronin Trough (VT). The colour scale is limited down to 600 m depth to highlight the bathymetry on the shelf. Non-coloured areas are outside the model domain and indicate the open boundaries in the north and the west.

Barents Sea has an opening to the North Atlantic in the west, from mainland Norway up to the Svalbard Islands, and a restricted connection to the Arctic Ocean in the north, between Svalbard and the shallow areas around Franz Josefs Land, see Figure A.1. Barents Sea has an average depth of less than 230 m, with the deepest parts in the south (Central Basin deeper than 300 m) and the most

shallow areas south-east of Svalbard (Central Bank and the Great Bank less than 200 m). The north to south stretched out island Novaya Zemlya separate Barents Sea from Kara Sea in the east. The connection between the two seas, is restricted to a narrow and shallow passage south of the island and a wider and partly deeper area north of the island, see Figure A.1.

The Kara Sea is relatively shallow with a large part less than 100 m deep. Though, a deep narrow channel along the east coast of Novaya Zemlya 200-400 m and two deep troughs in the north (St. Anna Trough around 500 m and Veronin Trough around 400 m) resulting in an average depth of 111 m [Volkov et al., 2002]. The central and eastern parts are the shallowest areas with the river mouths of the Ob and the Yenisey rivers, less than 30 m, and several islands. The two deeper troughs in the north connect Kara Sea to the much deeper Nansen Basin in the Arctic Ocean, see Figure A.1.

A.2 The Fram Strait region

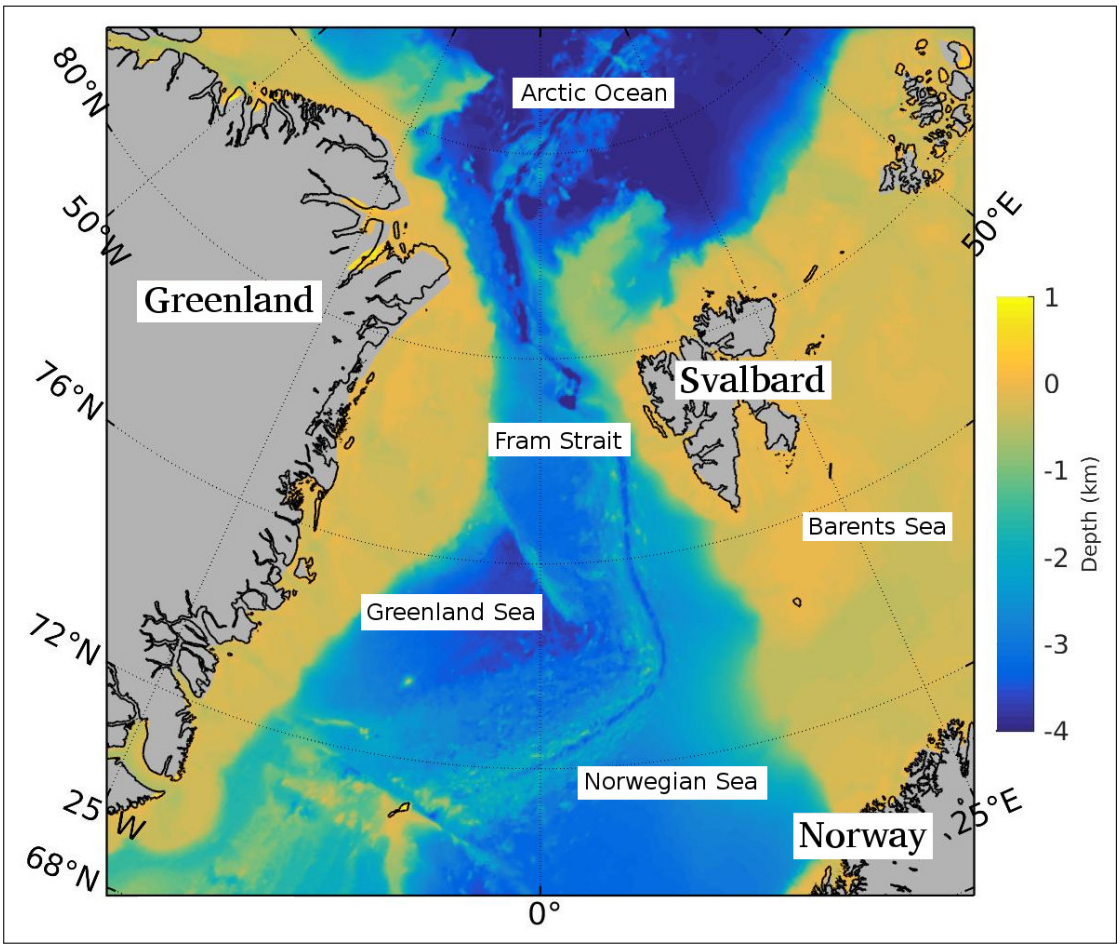

Figure A.2: Bathymetry used in the Fram Strait basemap.

The Fram Strait is the passage between Greenland and Svalbard, located roughly between $77°N$ and $81°N$ latitudes and centered on the prime meridian. The Greenland and Norwegian Seas lie south of Fram Strait leaving the Nansen Basin and the rest of the Arctic Ocean to the north. The width of the strait is about 450 km but because of the wide continental shelves of Greenland and Spitsbergen, the deep portion of Fram Strait is only about 300 km wide.

Within Fram Strait, the sill connecting the Arctic and Fram Strait is 2545 m deep. The Knipovich Ridge is the northernmost section of the mid-Atlantic ridge and extends northward through the strait to connect to the Nansen-Gakkel ridge of the Arctic Ocean. A rift valley, caused by sea-floor spreading, runs adjacent and parallel to the Knipovich ridge. The deepest location is the Molloy Deep which is the deepest point of the whole Arctic basin (5607 m). The shallowest is the Yermak

Plateau, with a mean depth of about 650 m, lying to the northwest of Spitsbergen.

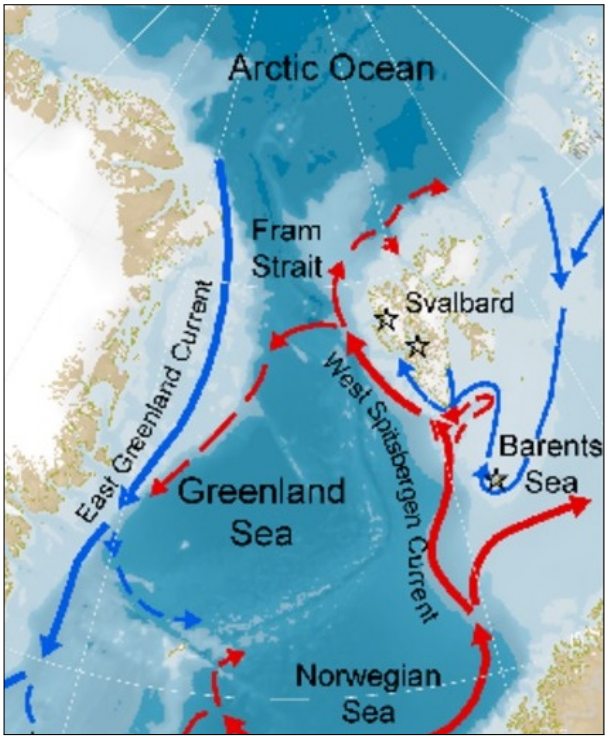

Figure A.3: Main currents in the Fram Strait region.

The Fram Strait is noted for being the only deep connection between the Arctic Ocean and the world oceans and as dominant oceanographic features displays the West Spitsbergen Current on the east side of the strait and the East Greenland Current on the west. This exchange occurs in both directions, with specific water masses identified with specific regions flowing between the Oceans. For instance water with characteristics of the deep Canadian and Eurasian Basins of the Arctic are observed leaving the Arctic in the deep western side of Fram Strait while on the eastern side, cold water from the Norwegian Sea is observed entering the Arctic below the West Spitsbergen Current [Langehaug and Falck, 2012].

The Arctic Basin exports $\approx$ 10% of the sea ice area southwards annually through Fram Strait. The Fram Strait area is in fact located downwind of the transpolar drift the major ocean current of the Arctic Ocean transporting sea ice from the northern regions. However in recent years, a larger than normal export decreases the remaining mean thickness and ice area. A new updated timeseries from 1979-2013 of Fram Strait sea ice area export shows an overall increase until today, and that more than 1 million km^2 has been exported annually in recent

years showing an increasing trend of 7% per decade. Spring and summer area export increases more ($\approx 14\%$ per decade) than in autumn and winter, and these export anomalies have a large influence on the following September mean ice extent. This alarming behaviour is a compelling argument in the choice of such region for the study of wave-ice interaction.

Appendix B

WIM diagnostics

The WIM model described in chapter 2 is still encountering difficulties in its validation since the scarce observations available on FSD, however, two methods are proposed in order to analyse and compare it to the OSIM results. To asses the impact that modeled waves in ice have on a sea-ice model the first parameter to be studied is the stress arising from wave-ice interaction. The second parameter is the alternative growth rate related to the FSD after wave induced break-up events. Eventually a functional feedback between wave-induced events and sea ice will lead to the comparison between modeled IC and observations. This result can be achieved only after a deeper study of waves-ice interactions.

B.1 Wave momentum on sea ice

B.1.1 Mean momentum calculation

To evaluate the stresses imposed to the sea-ice by waves, the propagation of gravity waves in deep water is considered. The ocean is supposed to be inviscid and the motion irrotational, from the incompressibility condition $\nabla \cdot \mathbf{u} = 0$. The motion is thus specified by:

$$\mathbf{u} = \nabla\phi \ , \ \nabla^2\phi = 0 \tag{B.1}$$

with $\partial\phi/\partial n = 0$ at fixed surfaces, $\dot{\zeta} = \partial\phi/\partial z$ at $z = 0$ and as dynamical boundary condition:

$$\frac{d}{dt}\left(\frac{p_a}{\rho}\right) + \frac{\partial^2\phi}{\partial t^2} + g\frac{\partial\phi}{\partial z} - \gamma\nabla_h^2\left(\frac{\partial\phi}{\partial z}\right) = 0 \text{ at } z = 0 \tag{B.2}$$

where $\mathbf{u}$ is the velocity vector and ϕ the velocity potential. As for the dynamical boundary condition, at fixed surfaces (i.e. the sea-bed) the normal velocity component vanishes ($\partial\phi/\partial n = 0$) however for the free-surface conditions, if the position of the surface is specified by $z = \zeta(x, y, t)$ at all times, then its total derivative will be:

$$w|_{z=\zeta} = d\zeta/dt = \dot{\zeta} + \mathbf{q}|_{z=\zeta} \cdot \nabla_h\zeta \tag{B.3}$$

where $\nabla_h \equiv (\partial/\partial x, \partial/\partial y)$ is the horizontal gradient operator while $\mathbf{q} = (u, v)$ the horizontal vectorial component of the velocity field. In an irrotational motion, this kinematic free-surface condition becomes:

$$(\partial\phi/\partial z) = \dot{\zeta} + (\nabla_h\zeta) \cdot (\nabla_h\phi)|_{z=\zeta} \tag{B.4}$$

Is then required that difference in pressure between the two sides of the surface can differ only as a result of surface tension. Given the Bernoulli's equation for an irrotational flow, the pressure in the water at a free surface is given by:

$$p/\rho + g\zeta + (\dot{\phi})|_{z=\zeta} + \frac{1}{2}(\nabla\phi)^2|_{z=\zeta} = 0 \tag{B.5}$$

With a prescribed atmospheric pressure and given the initial conditions, these equations suffice to determine the subsequent motion. Since the wave is considered to be in a deep-water configuration, the free surface conditions can be expressed as a Taylor series expansion about $z = 0$.

First-order solutions are sufficient since certain mean properties of the motion such as the energy and momentum density (both of second order) can be found very simply from the first-order solutions. An arbitrary sinusoidal disturbance is considered which, by Fourier's theorem, can be considered as a superposition of elementary waves each of which is independent from the first-order propagation.

If the surface displacement is

$$\zeta = a\cos(\mathbf{k}\cdot\mathbf{x} - \omega t) \tag{B.6}$$

the associated velocity potential is

$$\phi = \frac{\omega a \cosh k(z+d)}{k \sinh kd} \sin(\mathbf{k}\cdot\mathbf{x} - \omega t) \tag{B.7}$$

where $k = |\mathbf{k}|$.
The radial frequency ω comes from B.2 and with constant atmospheric pressure p_a:

$$\omega^2 = gk(1 + \gamma k^2/g)\tanh kd = \sigma^2(k) \tag{B.8}$$

where γ is the ratio of surface tension to water density.

Most of the energy of ocean waves is found in deep water gravity waves for which surface tension is negligible and $kd \gg 1$ so B.8 reduces to $\sigma^2 = gk$ and the velocity potential B.7:

$$\phi = k^{-1}\sigma a e^{kz} \sin(\mathbf{k}\cdot\mathbf{x} - \sigma t), \tag{B.9}$$

The mean energy per unit area of the wave motion can be readily found from:

$$\begin{aligned} T &= \frac{\rho}{2}\overline{\int_{-d}^{\zeta} \mathbf{u}^2 dz} \\ &\approx \frac{\rho}{2}\int_{-d}^{0} \overline{\mathbf{u}^2} dz \\ &= \frac{\rho\sigma^2 a^2}{4k}\coth kd \end{aligned} \tag{B.10a}$$

Since in any conservative dynamical system undergoing small oscillations the

mean potential and kinetic energies are equal, the total energy density is:

$$\begin{aligned} E &= (2k)^{-1}\rho\sigma^2 a^2 \coth kd; \quad \text{for gravity waves} \quad \gamma k^2/g \ll 1 \\ &= \frac{1}{2}\rho g a^2 = \rho g\overline{\zeta^2} \end{aligned} \tag{B.11a}$$

Finally, the mean momentum per unit area $\mathbf{M}$ is a second-order quantity that can be found from the first-order solutions:

$$\mathbf{M} = \rho\overline{\int_{-d}^{\zeta} \mathbf{q} dz} = \rho\overline{\int_{-d}^{\zeta} \nabla_h \phi dz} \tag{B.12}$$

Now considering the identity:

$$\nabla_h \int_{-d}^{\zeta} \phi dz \equiv (\nabla_h \zeta)\phi_\zeta + \int_{-d}^{\zeta} \nabla_h \phi dz,$$

The term on the left is the gradient of an oscillating quantity, whose mean vanishes while the mean of the last is $\mathbf{M}/\rho$. Thus:

$$\begin{aligned} \mathbf{M} &= -\rho\overline{\phi|_{z=\zeta}\nabla_h\zeta} \\ &\approx -\rho\overline{\phi|_{z=0}\nabla_h\zeta} \\ &= \frac{\mathbf{k}}{2k}\rho\sigma a^2 \coth kd \\ &= \frac{E\mathbf{k}}{ck}, \end{aligned} \tag{B.13}$$

where $c = \sigma/k$ is the phase speed.

B.1.2 Momentum flux

Considering now a spectrum of wave frequencies and directions, the momentum flux is

$$\begin{aligned} D_t\mathbf{M} &= \int_0^{\infty}\int_0^{2\pi} D_t\left(\frac{S(\mathbf{x},t,\omega,\theta)}{c}\right)\frac{\mathbf{k}}{k}\mathrm{d}\theta\mathrm{d}\omega \\ &= -\int_0^{\infty}\int_0^{2\pi}\left(\frac{c_g R_{ice}}{c}\right)\frac{\mathbf{k}}{k}\mathrm{d}\theta\mathrm{d}\omega. \end{aligned} \tag{B.14}$$

This is the momentum flux to the waves from other sources (ice, ocean and atmosphere), its negative is the momentum flux out of the waves into these sources. If we know which source in particular then it can be included in the momentum equations for that source. In the case of scattering, it is most likely that the momentum will be transferred to the ice, causing it to drift in the dominant direction of the waves.

B.2 Wave effects on sea ice

B.2.1 Heat fluxes

As explained in section 1.1.4 sea ice growths are heavily affected by the FSD. This is due to the relation between the lateral and bottom surface of a floe, exposition of ice surface to the environment (i.e. ocean water, atmosphere) increases melting rates. In this section lateral and bottom surfaces for model products are calculated, this allow to estimate an alternative growth of sea ice. These growth is referred to as WIM growth (W-growth) while the unmodified growth as OSIM growth (O-growth).

O-growths are calculated from the OSIM's existing thermodynamics, given the following parameters old ice concentration (f_i), old ice thickness (h_i), new ice concentration (Δf_i) and new ice thickness (Δh_i); O-growths can be written as:

$$G_{vrt} = f_i\frac{\Delta h_i}{\Delta t}, \tag{B.15a}$$

$$G_{lat} = h_i\frac{\Delta f_i}{\Delta t}. \tag{B.15b}$$

OSIM output three heat fluxes that go into the ice:

- Q_{cool} $[J/s]$ - Flux to cool the mixed (top) layer of the ocean to freezing
- Q_{atm} $[J/s]$ - Flux into ocean from atmosphere
- Q_{other} $[J/s]$ - Flux into ice from above (i.e. fluxes from the snow,melt ponds and conduction from top)

Now it is possible to calculate the absolute lateral and vertical heat fluxes:

$$\begin{aligned} q_{atm} &= Q_{atm}(1 - f_i)A_{sq}\Delta t, \\ q_{cool} &= Q_{cool}A_{sq}\Delta t, \\ q_{other} &= Q_{other}f_i A_{sq}\Delta t, \\ q_{dist} &= q_{cool} + q_{atm}, \\ q_{lat} &= \alpha_{lat}q_{dist}, \qquad \text{(B.16a)} \\ q_{vrt} &= q_{other} + (1 - \alpha_{lat})q_{dist}. \qquad \text{(B.16b)} \end{aligned}$$

Since sea ice volume change will be studied, the latent heat of fusion of ice per volume has to be considered.

$$L_{water} = 333550 \left[\frac{J}{kg}\right] \longrightarrow L' = L_{water} \cdot \rho \left[\frac{J}{m^3}\right] \qquad \text{(B.17a)}$$

$$L'_i = 3.02 \times 10^8 \left[\frac{J}{m^3}\right] \qquad \text{(B.17b)}$$

$$L'_s = 1.10 \times 10^8 \left[\frac{J}{m^3}\right] \qquad \text{(B.17c)}$$

Sea ice density is on average $\rho_{s.ice} = 900 \left[\frac{kg}{m^3}\right]$ [Timco and Frederking, 1996]. Since snow is subject to compaction an average value is considered, specifically is chosen the density of *higly settled snow* (or *Depth Hoar*), with $\rho_{snow} = 330 \left[\frac{kg}{m^3}\right]$ [Paterson, 1994].

B.2.2 Lateral changes: Freezing ($Q_{lat} < 0$)

If conditions are proper and sea ice freezes growing in volume, snow is excluded.

$$\begin{aligned} q_{lat} &= -L_i' \Delta V_{lat} = -L_i' h_i \Delta f_i A_{sq} && \text{(B.18a)} \\ &= Q_{lat} \Delta t S_{lat} \\ &= \beta_{lat} Q_{lat} \Delta t S_{bot} \\ &= \beta_{lat} Q_{lat} \Delta t f_i A_{sq} && \text{(B.18b)} \end{aligned}$$

Thus the change in concentration based on the FSD is:

$$\Delta f_i = -\frac{\beta_{lat} f_i Q_{lat} \Delta t}{L_i' h_i} \tag{B.19}$$

Considered that ice concentration cannot be bigger than 1 ($0 < f_i < f_{max} = 1$), if $f_i' = f_i + \Delta f_i > f_{max}$ an effective growth will be defined (i.e. moving growth from lateral to vertical)

$$\Delta f_{i,eff} = f_{i,max} - f_i \tag{B.20a}$$

$$\Delta h_{i,eff} = \frac{h_i}{f_{i,max}} (f' - f_{i,max}) \tag{B.20b}$$

$$\Delta V_{vrt,eff} = h_i A_{sq} (f_i' - f_{i,max}) = f_{i,max} A_{sq} \Delta h_{i,eff} \tag{B.20c}$$

$$\Delta V_{lat,eff} = h_i (f_{i,max} - f_i) A_{sq} \tag{B.20d}$$

Using the effective changes, the two model can be compared (only the initial and final values of concentration (f_i) and thickness (h_i) are given).

$$Q_{lat,eff} = -\frac{L'_i}{\beta_{lat} f_i} \times \frac{\Delta V_{lat,eff}}{A_{sq} \Delta t} \tag{B.21a}$$

$$= -\frac{L'_i}{\beta_{lat} f_i} \times \frac{h_i}{\Delta t}(f_{i,max} - f_i) \tag{B.21b}$$

$$Q_{vrt,eff} = -\frac{L'_i}{f_i} \times \frac{\Delta V_{vrt,eff}}{A_{sq} \Delta t} \tag{B.21c}$$

$$= -\frac{L'_i}{f_{i,max}} \times \frac{\Delta h_i}{\Delta t} \tag{B.21d}$$

B.2.3 Lateral changes: melting ($Q_{lat} > 0$)

When melting, even snow has to be considered (imaging it as underwater in unrealistic)

$$q_{lat} = -(L'_i \Delta V_{lat,s.ice} + L'_s \Delta V_{lat,snow}) \tag{B.22a}$$

$$= -(L'_i h_i + L'_s h_s) \Delta f_i A_{sq} \tag{B.22b}$$

$$= -\beta_{lat} Q_{lat} \Delta t f_i A_{sq} \tag{B.22c}$$

From these:

$$\Delta f_i = -\frac{\beta_{lat} f_i Q_{lat} \Delta t}{(L'_i h_i + L'_s h_s)} \tag{B.23a}$$

$$Q_{lat} = -\frac{(L'_i h_i + L'_s h_s)}{\beta_{lat} f_i} \times \frac{\Delta f_i}{\Delta t} \tag{B.23b}$$

B.2.4 Vertical changes

As for vertical changes, both freezing ($Q_{vrt} < 0$) and melting ($Q_{vrt} > 0$) can be derived from the same procedure.

$$q_{vrt} = -L'_i \Delta V_{vrt} = -L'_i S_{bot} \Delta h_i = -L'_i f_i \Delta h_i A_{sq} \tag{B.24a}$$

$$= Q_{vrt} \Delta t f_i A_{sq} \tag{B.24b}$$

From which:

$$\Delta h_i = -\frac{Q_{vrt}\Delta t}{L'_i} + \Delta h_{i,eff} \tag{B.25a}$$

$$Q_{vrt} = -L'_i \frac{\Delta h_i}{\Delta t} \tag{B.25b}$$

$$= -\frac{L'_i}{f_i} \times \frac{\Delta V_{vrt}}{A_{sq}\Delta t} \tag{B.25c}$$

In conclusion, lateral and vertical growths derived from FSD can be written as:

$$G_{lat}^{WIM} = h_i \frac{\Delta f_{i,eff}}{\Delta t} \tag{B.26a}$$

$$G_{vrt}^{WIM} = f_{i,eff} \frac{\Delta h_{i,eff}}{\Delta t} \tag{B.26b}$$

where $f_{i,eff} = f_i$ in case of melting $Q_{lat} > 0$.

Symbol	Description	Units
V	ice vol	m^3
q	heat	J
Q	heat flux	W/m^2
f_i	ice fraction	-
h_i	ice thickness	m
L_{water}	water latent heat of fusion	J/kg
L'_i	sea ice latent heat of fusion per volume	J/m^3
L'_s	snow latent heat of fusion volume	J/m^3
h_s	snow depth	m
S_{lat}	Lateral surface area	m^2
S_{bot}	Bottom surface area	m^2
A_{sq}	Area of grid cell	m^2
C_p	specific heat of seawater	$J\,K^{-1}kg^{-1}$
ρ_{sw}	density of sea water	$kg\,m^{-3}$
h_{ml}	ocean layer thickness	m
T_{ml}	ocean layer temperature	K
T_f	ocean freezing temperature	K

Table B.1: Symbols

Bibliography

[Ardhuin et al., 2008] Ardhuin, F., Rascle, N., and Belibassakis, K. a. (2008). Explicit wave-averaged primitive equations using a generalized Lagrangian mean. *Ocean Modelling*, 20(1):35–60.

[Asplin et al., 2012] Asplin, M. G., Galley, R., Barber, D. G., and Prinsenberg, S. (2012). Fracture of summer perennial sea ice by ocean swell as a result of Arctic storms. *Journal of Geophysical Research: Oceans*, 117(6):1–12.

[Bennetts et al., 2010] Bennetts, L. G., Peter, M. a., Squire, V. a., and Meylan, M. H. (2010). A three-dimensional model of wave attenuation in the marginal ice zone. *Journal of Geophysical Research*, 115(C12):1–50.

[Bennetts and Squire, 2012a] Bennetts, L. G. and Squire, V. a. (2012a). Model sensitivity analysis of scattering-induced attenuation of ice-coupled waves. *Ocean Modelling*, 45-46:1–13.

[Bennetts and Squire, 2012b] Bennetts, L. G. and Squire, V. a. (2012b). Model sensitivity analysis of scattering-induced attenuation of ice-coupled waves. *Ocean Modelling*, 45-46:1–13.

[Canuto et al., 2002] Canuto, V. M., Howard, A., Cheng, Y., and Dubovikov, M. S. (2002). Ocean Turbulence. Part II: Vertical Diffusivities of Momentum, Heat, Salt, Mass, and Passive Scalars. *Journal of Physical Oceanography*, 32(1):240–264.

[Doble and Bidlot, 2012] Doble, M. J. and Bidlot, J.-R. (2012). Wavebuoy measurements at the Antarctic sea ice edge compared with an enhanced ECMWF WAM: progress towards global waves-in-ice modelling. *Ocean Modelling*, 70(Ocean Surface Waves):166–173.

[Drange and Simonsen, 1996] Drange, H. and Simonsen, K. (1996). Formulation of air-sea fluxes in the ESOP2 version of MICOM. *NERSC Report*, 125(9).

[Dumont et al., 2011] Dumont, D., Kohout, a., and Bertino, L. (2011). A wave-based model for the marginal ice zone including a floe breaking parameterization. *Journal of Geophysical Research: Oceans*, 116(4):1–12.

[Evensen, 1994] Evensen, G. (1994). Sequential data assimilation with a nonlinear quasi-geostrophic model using Monte Carlo methods to forecast error statistics. *Journal of Geophysical Research*, 99(C5):10143.

[Feltham, 2005] Feltham, D. L. (2005). Granular flow in the marginal ice zone. *Philosophical transactions. Series A, Mathematical, physical, and engineering sciences*, 363(1832):1677–1700.

[Fox and Squire, 1991] Fox, C. and Squire, V. a. (1991). Strain in shore fast ice due to incoming ocean waves and swell. *Journal of Geophysical Research*, 96(C3):4531.

[Girard et al., 2010] Girard, L., Amitrano, D., and Weiss, J. (2010). Failure as a critical phenomenon in a progressive damage model. *Journal of Statistical Mechanics: Theory and Experiment*, 2010(01):P01013.

[Girard et al., 2009] Girard, L., Weiss, J., Molines, J. M., Barnier, B., and Bouillon, S. (2009). Evaluation of high-resolution sea ice models on the basis of statistical and scaling properties of Arctic sea ice drift and deformation. *Journal of Geophysical Research: Oceans*, 114(8):1–15.

[Hasselmann and Hasselmann, 1985] Hasselmann, S. and Hasselmann, K. (1985). Computations and Parameterizations of the Nonlinear Energy Transfer in a Gravity-Wave Spectrum. Part I: A New Method for Efficient Computations of the Exact Nonlinear Transfer Integral.

[Herman, 2010] Herman, A. (2010). Sea-ice floe-size distribution in the context of spontaneous scaling emergence in stochastic systems. *Physical Review E*, 81(6):066123.

[Herman, 2011] Herman, A. (2011). Molecular-dynamics simulation of clustering processes in sea-ice floes. *Physical Review E*, 84(5):056104.

[Herman, 2012] Herman, A. (2012). Influence of ice concentration and floe-size distribution on cluster formation in sea-ice floes. *Central European Journal of Physics*, 10(3):715–722.

[Herman, 2013] Herman, A. (2013). Shear-jamming in two-dimensional granular materials with power-law grain-size distribution. *Entropy*, 15(11):4802–4821.

[Hibler III, 1979] Hibler III, W. D. (1979). A Dynamic Thermodynamic Sea Ice Model. *Journal of Physical Oceanography*, 9:815–846.

[Hunke and Dukowicz, 1997] Hunke, E. C. and Dukowicz, J. (1997). An Elastic-Viscous-Plastic Model for Sea Ice Dynamics. (Hibler 1979):1849–1867.

[Keghouche et al., 2010] Keghouche, I., Counillon, F., and Bertino, L. (2010). Modeling dynamics and thermodynamics of icebergs in the Barents Sea from 1987 to 2005. *Journal of Geophysical Research*, 115(C12):C12062.

[Kohout and Meylan, 2008] Kohout, a. L. and Meylan, M. H. (2008). An elastic plate model for wave attenuation and ice floe breaking in the marginal ice zone. *Journal of Geophysical Research: Oceans*, 113(9):1–17.

[Kwok, 2005] Kwok, R. (2005). Variability of Nares Strait ice flux. *Geophysical Research Letters*, 32(24):1–4.

[Langehaug and Falck, 2012] Langehaug, H. R. and Falck, E. (2012). Changes in the properties and distribution of the intermediate and deep waters in the Fram Strait. *Progress in Oceanography*, 96(1):57–76.

[Liu and Mollo-Christensen, 1988] Liu, A. K. and Mollo-Christensen, E. (1988). Wave Propagation in a Solid Ice Pack.

[Mandelbrot, 1983] Mandelbrot, B. B. (1983). The Fractal Geometry of Nature.

[Marko, 2003] Marko, J. R. (2003). Observations and analyses of an intense waves-in-ice event in the Sea of Okhotsk. *Journal of Geophysical Research*, 108(C9):1–14.

[Masson and Leblond, 1989] Masson, D. and Leblond, P. H. (1989). Spectral evolution of wind-generated surface gravity waves in a dispersed ice field. *Journal of Fluid Mechanics*, 202:43–81.

[Mellor, 1986] Mellor, M. (1986). *Mechanical behavior of sea ice.*

[Meylan and Masson, 2006] Meylan, M. H. and Masson, D. (2006). A linear Boltzmann equation to model wave scattering in the marginal ice zone. *Ocean Modelling*, 11(3-4):417–427.

[Meylan et al., 1997] Meylan, M. H., Squire, V. A., and Fox, C. (1997). Toward realism in modelling ocean wave behavior in marginal ice zones. *J Geophys Res*, 102(C10):22981–22991.

[NERSC, 2016] NERSC (2016). Ships and Waves Reaching Polar Regions D5 . 1 Validation Reports. Technical report.

[Paterson, 1994] Paterson, W. S. B. (1994). *The Physics of Glaciers*. Butterworth-Heinemann.

[Perrie and Hu, 1996] Perrie, W. and Hu, Y. (1996). Air-Ice-Ocean Momentum Exchange. Part 1: Energy Transfer between Waves and Ice Floes.

[Polnikov and Lavrenov, 2007] Polnikov, V. G. and Lavrenov, I. V. (2007). Calculation of the nonlinear energy transfer through the wave spectrum at the sea surface covered with broken ice. *Oceanology*, 47(3):334–343.

[Prinsenberg and Peterson, 2011] Prinsenberg, S. J. and Peterson, I. K. (2011). Observing regional-scale pack-ice decay processes with helicopter-borne sensors and moored upward-looking sonars. *Annals of Glaciology*, 52(57 PART 1):35–42.

[Proshutinsky et al., 2005] Proshutinsky, A., Yang, J., Krishfield, R., Gerdes, R., Karcher, M., Kauker, F., Koeberle, C., Hakkinen, S., Hibler, W., Holland, D., Maqueda, M., Holloway, G., Hunke, E., Maslowski, W., Steele, M., and Zhang, J. (2005). Arctic ocean study: Synthesis of model results and observations. *Eos, Transactions American Geophysical Union*, 86(40):368–371.

[Rampal et al., 2015] Rampal, P., Bouillon, S., Olason, E., and Morlighem, M. (2015). neXtSIM : a new Lagrangian sea-ice model. In *The Cryosphere Discussions*, number 1, page 56.

[Rampal et al., 2008] Rampal, P., Weiss, J., Marsan, D., Lindsay, R., and Stern, H. (2008). Scaling properties of sea ice deformation from buoy dispersion analysis. *Journal of Geophysical Research*, 113(C3):1–12.

[Robinson and Palmer, 1990] Robinson, N. J. and Palmer, S. C. (1990). A modal analysis of a rectangular plate floatng on an incompressible fluid. *J. Sound Vibration*, 142(3):453–460.

[Rothrock and Thorndike, 1984] Rothrock, D. a. and Thorndike, a. S. (1984). Measuring the sea ice floe size distribution. 89:6477–6486.

[Sakov et al., 2012] Sakov, P., Counillon, F., Bertino, L., Lisæter, K. A., Oke, P., and Korablev, a. (2012). TOPAZ4: an ocean sea ice data assimilation system for the North Atlantic and Arctic. *Ocean Sci.*, 8:633–662.

[Shen et al., 2004] Shen, H. H., Ackley, S. F., and Yuan, Y. (2004). Limiting diameter of pancake ice. *Journal of Geophysical Research C: Oceans*, 109(12):1–13.

[Shen et al., 1987] Shen, H. H., Hibler, W. D., and Leppäranta, M. (1987). The role of floe collisions in sea ice rheology. *Journal of Geophysical Research*, 92(C7):7085.

[Sorteberg and Kvingedal, 2006] Sorteberg, A. and Kvingedal, B. (2006). Atmospheric Forcing on the Barents Sea Winter Ice Extent. *Journal of Climate*, 19(19):4772–4784.

[Squire, 2007] Squire, V. a. (2007). Of ocean waves and sea-ice revisited. *Cold Regions Science and Technology*, 49(2):110–133.

[Squire et al., 1995] Squire, V. A., Dugan, J. P., Wadhams, P., Rottier, P. J., and Liu, A. K. (1995). Of Ocean Waves and Sea Ice. *Annual Review of Fluid Mechanics*, 27(1):115–168.

[Squire and Moore, 1980] Squire, V. a. and Moore, S. C. (1980). Direct measurement of the attenuation of ocean waves by pack ice. *Nature*, 283(5745):365–368.

[Steele, 1992] Steele, M. (1992). Sea ice melting and floe geometry in a simple ice-ocean model. *Journal of Geophysical Research*, 97(C11):17729.

[Steele et al., 1989] Steele, M., Morison, J. H., and Unterstener, N. (1989). The Partition of Air-Ice-Ocean Momentum Exchange as a Function of Ice Concentration , Floe Size , and Draft. *Journal of Geophysical Research*, 94(C9):12739–12750.

[Steer et al., 2008] Steer, A., Worby, A., and Heil, P. (2008). Observed changes in sea-ice floe size distribution during early summer in the western Weddell Sea. *Deep Sea Research Part II: Topical Studies in Oceanography*, 55(8-9):933–942.

[Stephenson et al., 2011] Stephenson, S. R., Smith, L. C., and Agnew, J. a. (2011). Divergent long-term trajectories of human access to the Arctic. *Nature Climate Change*, 1(3):156–160.

[Strong, 2012] Strong, C. (2012). Atmospheric influence on Arctic marginal ice zone position and width in the Atlantic sector, February-April 1979-2010. *Climate Dynamics*, 39(12):3091–3102.

[Timco and Frederking, 1996] Timco, G. and Frederking, R. (1996). A review of sea ice density. *Cold Regions Science and Technology*, 24(1):1–6.

[Timco and O.'Brien, 1994] Timco, G. and O.'Brien, S. (1994). Flexural strength equation for sea ice. *Cold Regions Science and Technology*, 22(3):285–298.

[Timco and Weeks, 2010] Timco, G. W. and Weeks, W. F. (2010). A review of the engineering properties of sea ice. *Cold Regions Science and Technology*, 60(2):107–129.

[Toyota et al., 2011] Toyota, T., Haas, C., and Tamura, T. (2011). Size distribution and shape properties of relatively small sea-ice floes in the Antarctic marginal ice zone in late winter. *Deep-Sea Research Part II: Topical Studies in Oceanography*, 58(9-10):1182–1193.

[Toyota et al., 2006] Toyota, T., Takatsuji, S., and Nakayama, M. (2006). Characteristics of sea ice floe size distribution in the seasonal ice zone. *Geophysical Research Letters*, 33(2):2–5.

[Turcotte, 1986] Turcotte, D. L. (1986). Fractals and fragmentation. *Journal of Geophysical Research*, 91(5):1921–1926.

[Ulaby et al., 1981] Ulaby, F., Moore, R., Fung, A., and House, A. (1981). Microwave remote sensing: active and passive.

[Volkov et al., 2002] Volkov, V. A., Johannessen, O. M., Borodachev, V. E., Voinov, G. N., Pettersson, L. H., Bobylev, L. P., and Kouraev, A. V. (2002). *Polar Seas Oceanography: An integrated case study of the Kara Sea*. Springer Science & Business Media.

[Wadhams et al., 1988] Wadhams, P., Squire, V. A., Goodman, D. J., Cowan, A. M., and Moore, S. C. (1988). The Attenuation Rates of Ocean Waves in the Marginal Ice Zone. *Journal of Geophysical Research*, 93(C6):6799–6818.

[Wang and Shen, 2011] Wang, R. and Shen, H. H. (2011). A continuum model for the linear wave propagation in ice-covered oceans: An approximate solution. *Ocean Modelling*, 38(3-4):244–250.

[Weber, 1987] Weber, J. E. (1987). Wave Attenuation and Wave Drift in the Marginal Ice Zone.

[Weiss, 2001] Weiss, J. (2001). Fracture and fragmentation of ice: a fractal analysis of scale invariance. *Engineering Fracture Mechanics*, 68(17-18):1975–2012.

[Wentz, 1997] Wentz, F. (1997). A well calibrated ocean algorithm for special sensor microwave/imager. *Journal of Geophysical Research: Oceans*.

[Williams et al., 2013a] Williams, T. D., Bennetts, L., Squire, V. a., Dumont, D., and Bertino, L. (2013a). Wave-ice interactions in the marginal ice zone. Part 1: Theoretical foundations. *Ocean Modelling*, (Part 1).

[Williams et al., 2013b] Williams, T. D., Bennetts, L. G., Squire, V. A., Dumont, D., and Bertino, L. (2013b). Wave-ice interactions in the marginal ice zone. Part 2: Model sensitivity studies along a 1-D section of the Fram Strait. *Ocean Modelling*, (Part 2).

Acknowledgements

First of all I would like to thank the Nansen Environmental and Remote Sensing Center and all his staff for making this work possible, for hosting me and, above all, for making me feel at home in a country so far from mine.
The biggest thank goes to Dr. Timothy Williams. After 5 months of working side-by-side with him I feel confident to say that he is not only a great scientist and mentor but also a true and dear friend. You will be a great $p\bar{a}p\bar{a}$.
I would like to thank Dr. Laurent Bertino, Dr. Jon Bergh, Dr. Phillip Griewank, Dr. Alberto Carassi and Dr. Jiping Xie for their guide, help, support and inspiration.
I would like to thank all the PHD students who worked with me during my staying in Norway; Patrick, Tobias and Lea. You guys are awesome. A special thank goes to Gaute, a true Norwegian with a golden heart and a top notch brain.
To my super crazy multi-ethnic friends Abhishek "Abibi", Anna "Lasagna" and Alexandra "Sasha".
As for my support in Italy, first of all my greatest thank goes to my Professor Nadia Pinardi whom, in her unique way, made me feel a real scientist and showed me the way during the (many) difficult moments in this thesis development.
To my all my FieSTa colleagues for their endless support.
To Sam and Bombix for being my family in Bologna.
A special thought for my friends "Gli Amici Miei" and specifically "APD". You are my dearest friends, I love you guys.
Last but not least to my whole family, especially my mom, my dad and brother Tommy. They are the only one in the world always able to make me feel special and loved. Their endless support and guide is the greatest gift a son (brother) could ever ask for. :)
Finally to the stunning city that stole my heart. Thank you Bologna, for loving me back.
To Moro.